UCLA
UCLA Electronic Theses and Dissertations

Title
Probing the Surface and the Interior of an Enzyme: What is the origin of Dissipation at the Angstrom scale?

Permalink
https://escholarship.org/uc/item/8gn7f5kp

Author
Alavi, Zahrasadat

Publication Date
2017

Supplemental Material
https://escholarship.org/uc/item/8gn7f5kp#supplemental

Peer reviewed|Thesis/dissertation

eScholarship.org Powered by the California Digital Library
University of California

UNIVERSITY OF CALIFORNIA
Los Angeles

Probing the Surface and the Interior of an Enzyme: What is the origin of Dissipation at the Angstrom scale?

A dissertation submitted in partial satisfaction
of the requirements for the degree
Doctor of Philosophy in Physics

by

Zahrasadat Alavi

2017

© Copyright by
Zahrasadat Alavi
2017

ABSTRACT OF THE DISSERTATION

Probing the Surface and the Interior of an Enzyme:
What is the origin of Dissipation at the Angstrom scale?

by

Zahrasadat Alavi
Doctor of Philosophy in Physics
University of California, Los Angeles, 2017
Professor Giovanni Zocchi, Chair

Biological macromolecules such as proteins are remarkable machines at the nano scale. The mechanical motion of proteins that is present in every living system allows those molecules to perform theie specific tasks. Most proteins are enzymes. Enzymes bind to their substrates, speed up the chemical reaction and release the products. Upon this binding and unbinding they undergo a large conformational motion. In case of Guanylate Kinase, the protein under study in my thesis, this deformation is about 1 nm, relatively large compared to the enzymes size ($\sim$ 4nm). This conformational motion is essential to the proteins activity. Proteins are not rigid solids, but rather deformable, wiggling and jiggling inside a medium. This deformability is a general materials property of a folded protein. Enzymes can be deformed and their activity can be modulated by perturbations other than ligand binding.

Fluctuations of enzymes have been studied for a long time and although some progress has been made, still much is unknown about proteins dynamics. In my thesis I try to reveal a little more about proteins dynamics by studying the effect of different kinds of perturbations. For this purpose, a nano-rheology technique is used which allows us to detect deformations as small as half an Angstrom. In this technique we look at the molecule as a whole: the interior polymer chain wrapped by the surface hydration layer. An oscillatory force is applied

to the protein, and the amplitude of the resulting oscillation is measured. It has been shown previously, that enzymes are viscoelastic: dissipative at low frequencies and elastic at higher frequencies. I have looked, more closely, for the origin of this atomic scale dissipation.

First, I study the contribution of the hydration layer, which is an integral part of the molecule, by modifying it using an order-inducing compound: Dimethyl Sulfoxide (DMSO), which, at small concentrations is harmless to a protein's native forms. This compound was added to the molecule's surface, i.e. the hydration shell, and formed strong hydrogen bonds with water molecules. Even at small DMSO concentrations a significant change in the dynamics was observed: the enzyme became more viscous. The effect is bigger at lower frequencies where enzyme shows dissipative behavior. In that sense, DMSO makes the enzyme more dissipative.

For the first time with this experimental setup, I measured the phase of the response (i.e. the phase difference between the applied force and the resulting deformation, which is basically the imaginary part of the amplitude). Having the ability to measure the phase, we have direct access to dissipation measurements. Phase measurements also revealed that DMSO makes the enzyme more dissipative, which suggest that the hydration layer partially controls the viscoelastic behavior.

Then I investigated at the contribution of the interior, i.e. the polymer chain bulk. To do so I induced point mutations in specific residues of the amino-acid sequence. The mutation points are in a region that goes under a huge strain as the enzyme goes from an open to a closed configuration. Surprisingly, one of the mutated proteins is 10 times more active than the wild type, meaning that the rate of the enzymatic reaction is 10 times faster with the mutated enzyme. Mechanics of the mutated proteins were studied using the same nano-rheology technique, and some changes were observed, suggesting that both the interior and the surface contribute to dissipation.

I then looked at the deformation caused by ligand binding, in order to see if there is any difference in how different mutants deform upon binding the substrates or unbinding the products. Since the effect of ligand binding is small, our detection method was improved to increase the sensitivity and therefore be able to detect these small deformations. It was seen that some ligands make the enzyme softer while others make the enzyme more resistive to driven deformations. In some cases ligand bindings signature was only detectable in phase measurements. Overall the conformational change caused by ligand binding was very similar among different mutants, with one exception. For one of the ligands (Guanylate monophosphate-GMP, which makes the enzyme stiffer) the fast mutant seems to have two binding events: one at low concentrations of the ligand and one at higher concentrations, whereas in the wild type only the low-concentration binding event is observed. It seems like the hyperactive mutant might have two binding sites for GMP: at higher concentrations, GMP might bind to ATP binding site. This is a case where specificity is traded off with speed: the mutant is faster but less specific.

Overall, some of my main results are:

- Hydration layer is an integral part of the molecule which is partially responsible for dissipation.

- Both interior and the surface contribute to the viscoelastic behavior. A dissipative contribution in the elastic regime is observed which can be associated with a second dissipation term, namely the one of the bulk.

- Phase measurements provide direct access to dissipation measurements at the atomic scale.

The dissertation of Zahrasadat Alavi is approved.

Chris Regan

William Gelbart

Joe Rudnik

Giovanni Zocchi, Committee Chair

University of California, Los Angeles

2017

To Monireh and Mahmoud, my wonderful parents
who have supported me from day 1.
To my dearest sister, Salma
who has always been ther for me.
And to my beloved husband, Amir,
without whom I would not know the joy of life.

Table of Contents

List of Figures

List of Tables

Acknowledgments

I could not go through my five years at UCLA without the help of amazing people who supported me every day. First of all, I would like to thank Giovanni Zocchi, my advisor, who has been there for me every day. To me, he is more than an advisor; he is my mentor, my friend and a role model I look up to. His compassion for science has always inspired me. He is an outstanding scientist who challenges his students and keeps them going forward with enthusiasm. Not only in science, but also in life, he has always been a great teacher to me. As an international student away from my family, his companion kept my heart warm and helped me feel like home.

I also send my gratitude to my wonderful colleagues and friends: Hao Qu, Chiao Tseng, Amila Ariyaratne, Hector G. Vasquez , Yilin Wang and Jared Lodico. I learnt a lot from every one of them. Their friendship meant a lot to me and made my daily life in the lab memorable.

I am grateful for having great teachers and mentors at UCLA. I learnt a lot from Joe Rudnik and would like to thank him for all the time and energy he spent to help me. I was honored to have Chris Regan and Bill Gelbart by my side, who helped me with their deep insights.

I would like to thank the wonderful staff in Physics Department. I send my deepest appreciations to Jenny Lee, without whom I could not start my graduate studies. She is a superhero with a big heart who has helped me greatly. I also thank Ernie Najar, Elaine Dolalas, Cecile Chang, Craig Reaves and Craig Murayama, who have helped my research, our lab and me every day. I thank Stephanie Krillov, who was always there for me to answer all my administrative questions, despite of her busy schedule.

I thank Benjamin and Carol Holmes, who supported me financially during my last year through a scholarship.

Finally, my deepest gratitude goes to my family. My mother was always there for me and stood by my side through my hardest time. My father always believed in me and made me stronger with his supports. I thank my dearest sister who never stopped helping me. She was my best friend and biggest supporter through these 5 years. I thank my amazing husband Amir, who makes my life happier every day. His help and support made my time in graduate school stress free.

Vita

2007–2011	B. Sc. (Physics), Sharif University of Technology, Tehran, Iran
2011–2012	Graduate Student, Teaching Assistant, Department of Physics and Astronomy, University of California, Riverside
2012–2017	PhD Candidate, Teaching Assistant and Graduate Research Assistant, Department of Physics and Astronomy, University of California, Los Angeles

Publications

Increasing the antioxidant activity of green tea polyphenols in the presence of iron for the reduction of graphene oxide O. Akhavan, Z. Alavi, et al., Carbon Journal, Volume 50, Issue 8, July 2012

Nano-rheology measurements reveal that the hydration layer of enzymes partially controls conformational dynamics Z. Alavi, A. Ariyaratne, G. Zocchi, Applied Physics Letters, Volume 106, Issue 20, May 2015

CHAPTER 1

Introduction

Enzymes are soft heterogeneous biological macromolecules with specific catalytic activity in aqueous environments. They are needed in almost all metabolic processes in the cell in order to make the process fast enough to sustain life. Most enzymes are proteins. Proteins consist of polypeptide chains of amino acids and a hydration shell which wraps around the bulk of the protein like a blanket. They are not rigid solids, but rather deformable, wiggling and jiggling inside a medium. These essential parts of organisms, participate in virtually every process within the cells. Enzymatic proteins act upon the reactants, namely substrates, by binding to them and release the products. Upon binding the substrates and unbinding the products, the enzyme undergoes a relatively large conformational change (Kos94; MK05), a property which may have co-evolved with the catalytic ability (TLE17). This conformational motion is essential to the proteins activity. Assuming a specific conformation allows the enzyme to catalyze a specific chemical reaction, while deformability confers the ability to operate as molecular machines. Deformability is, however, a more general materials property of the folded protein, and enzymes can be deformed - and their activity modulated - by perturbations other than ligand binding (Zoc09; TZ13).

Fluctuations of enzymes have been studied for a long time. These dynamics has been investigated in a long series of experiments by Frauenfelder and collaborators (Fen02; Fen04; Fra06) and others (YZ16a; YZ16b; BH11). According to Frauenfelder and colleagues, different types of protein motions have been proposed, i.e. solvent-slaved, hydration-shell-coupled, and vibrational (non-slaved) motions (Fen02; Fen04; al05). Solvent-slaved fluctuations are

due to dielectric fluctuations in the bulk solvent and thus are absent in a solid configuration or dehydrated proteins. These slaved motions have a rate proportional to the fluctuation rate in the solvent(Fen02; Fen04; Fra06). An example of this type of motion is the entrance and exit of dioxygen in Mb(Fen02; Fen04; al05).

Fluctuations in the hydration layer were measured, for example, by dielectric spectroscopy. This spectroscopy method measures the dielectric properties of a medium as a function of frequency and is based on the interaction of an external field with the electric dipole moment of the sample(KS03). This type of motion is present even if the enzyme is embedded in a solid, but absent in dehydrated proteins. Furthermore , fast water dynamics in the hydration layer is also measured by NMR (PH08). and Overhauser dynamic nuclear polarization (BH11; JH13).

Fluctuations in the polypeptide chain were measured by neutron and x-ray scattering, and, in the case of hemoglobin, by Mossbauer spectroscopy, which is based on resonant absorption and emission of gamma rays, of the Fe atom in the heme group (FMA01) Other groups have also looked at the conformational dynamics. In 2003, H. Yang et al. studied a naturally fluorescent flavin enzyme using single molecule electron transfer (ET). By correlation analysis they studies conformational fluctuation at multiple time scales and showed that multiple interconverting conformers exist that are related to the fluctuating catalytic activity (YLK03). Using NMR relaxation, it has been shown that collective domain motion on the μs-ms timescale is the rate limiting step in catalysis in different homologs of Aden Kinase. In this study Magnus Wolf-Watz et al. measured the rate of opening of the nucleotide binding lids in a thermophilic-mesophilic enzyme pair and showed that the slower lid opening rate is the only cause for the reduced activity of the thermophilic homolog (WTH04). Combining NMR and molecular dynamics computational analysis, it was shown that atomic fluctuations in hinge region of Adenylate Kinase in pico to nano second timescale, facilitates the large-scale slow rate lid motions(KLT07). These NMR studies are very valuable, however they cannot provide enough information about the connection between the chemical and

conformational dynamics. To study how interaction with ligands can lead to specific structural changes in the proteins we need to look at the entire course of the binding interaction. Furthermore simulations of the dynamical coupling on a ms timescale has suggested that the conformational dynamics does not have a significant contribution in dynamics(AW09).

In summary, although some progress has been made, still many secrets have remained unknown about protein dynamics.

To shed some light on some of these secrets, a nano-rheology technique has been used to investigate protein dynamics. Nano-rheology is essentially a traditional rheology experiment, where one imposes an oscillatory stress and measures the resulting strain. The technique is explained in details in Chapter 2. Using this specific experimental setup, an oscillatory force can be directly applied to the protein under study and measure the resulting strain. The timescale in these experiments are $100 micro$s to 100 ms, which is close to the timescale of the natural enzymatic cycle, therefore we can look at the dynamics involved in the enzymatic cycle. In this setup, there are about 10^8 molecules in the field of view and all the measurements are ensemble averaged. Thus, since the thermal fluctuations of individual molecules are independent, the thermal noise is cancelled out. In addition, this setup benefits from other noise rejection and signal enhancing techniques. Therefore a remarkable resolution is achieved. With this setup we can detect sub-Angstrom changes in the conformation of the protein.

Before proceeding, it is noteworthy to stress that "the enzyme" means the folded polypeptide chain plus the hydration layer at its surface. The hydration layer is an integral part of the protein and cannot be dissociated from it (al05) . Without it the enzyme is a totally different molecule with no functionality. Unlike individual spectroscopic techniques, which deal with either the polypeptide chain or the hydration water, nano-rheology deals with both. With this instrument, the internal rheology of one particular enzyme - Guanylate Kinase- has been investigated in some detail.

Now I summarize the results obtained previously. It was discovered that the dynamics of Angstrom size deformations of the enzyme is visco-elastic: elastic at "high" frequency, vis-

cous flow like at "low" frequency (WZ11a). High and low refers to a characteristic corner frequency $\omega_c \sim 100\, rad/s$ well defined in the experiments. The system is nonlinear in that, for example, the characteristic frequency ω_c depends on the amplitude F_0 of the applied force (QLZ12). Indeed, at fixed forcing frequency ω and for increasing F_0, the system undergoes an abrupt dynamic softening transition at a critical deformation amplitude $x_c \sim 1\, \mathring{A}$ (rms) (WZ11b). This value depends on ω (QZ13). A viscoelastic transition implies dissipative dynamics (AWT14; FRJ15) ; interpreting the corner frequency ω_c as a ratio of an elastic and a dissipative parameter: $\omega_c = \kappa/\gamma$ one finds indeed that the enzyme is effectively very viscous (WZ11a) .

In this thesis my aim is to examine more closely this molecular scale dissipation. Does the dissipation in the system originate mainly from the surface of the molecule, which includes the hydration layer, or from the interior, or both.

The role of the hydration layer in protein dynamics has, of course, been investigated before. It is clear that the hydration layer is an integral part of the protein (al05): without hydration layer, the molecule is a totally different object as far as dynamics and functionality. This is not surprising: unlike bulk materials, the physical properties of nanoparticles derive both from the surface and the interior. For a globular protein the size of GK, more than half the residues are at the surface of the molecule, and the "surface" comprises a dynamic network of hydrogen bonds between and amongst water molecules in the hydration layer and residues at the surface. Summarizing a wealth of experimental data, and following (al05; YZ16a) , we may say that the hydration shell fluctuations are strongly coupled to polypeptide chain fluctuations. We now proceed with the question, does the dissipation measured by nano-rheology originate from the surface or the interior of the enzyme ?

In Chapter 3 I show that chemically perturbing the hydration layer has a big effect on the measured dissipation (AAZ15) . The hydration shell is chemically modified by addition of DMSO - a kosmotropic (order inducing) agent - in concentrations so small that the bulk properties of the solvent (water) are unaffected. Yet a dramatic effect on the mechanical

susceptibility of the enzyme, measured through a the introduced nano-rheology method, is observed. Interpreted through the viscoelastic model of enzyme conformational dynamics (WZ11a; QLZ12; QZ13), which is explained in details in section 2.6.1 our measurements show that the enzyme's surface (the enzyme - water interface) partially controls the dissipative part of the dynamics.

In Chapter 4 we study the effect of point mutations in the interior of the molecule. The location of the mutations was chosen in a region which undergoes high strain during the enzymatic cycle, based on the structures of the open (apo) and closed (GMP bound) conformations of the enzyme (ML16). There is a readily observable effect on the enzymatic activity. However, summarizing the results of many experiments detailed in Chapter 4, we find that the effect of the point mutations on the mechanics measured by nano-rheology is relatively small. Finally Chapter 5 includes the protocols of different experimental techniques used in this study.

1.1 Other Techniques

1.1.1 FRET

Forster Resonance Energy Transfer is a distance measuring mechanism, which uses the energy transfer description between two light-sensitive molecules. This interaction can be taught of as a dipole-dipole coupling where the donor molecule is in excited state and transfer energy to the acceptor molecule. Since this energy transfer depends dramatically on the distance between the two molecules, FRET can be used for sensitive measurements of small changes in distance. This technique is widely used to measure distances between domains in a single protein and therefore can obtain information about the proteins conformation. To do so the protein is labeled at two appropriate sites with the donor and the acceptor. As the protein goes under a conformational change upon ligand binding the distance between the donor and the acceptor changes which results in a change in the fluorescence efficiency. The spatial resolution is in nanometer scale and thus it is not suitable to study sub-Angstrom changes.

1.1.2 AFM

Atomic Force Microscopy is a scanning probe microscopy technique invented in 1986 in which a mechanical probe gathers information by touching the surface. The surface under study can be modified in different ways, for example for biological applications it is grafted by proteins. This technique can be used as an imaging method. To do so, in the contact mode, the tip is in contact with the surface and an electronic feedback loop is used to keep the probe-sample contact force constant while the tip scans the surface. The feedback loop has a cantilever deflection as the input. As the probe scans the surface in 2-D, the changes in the third dimension (i.e. height) is adjusted by the feedback loop so that the probe remains in contact with the sample. The signals are (e.g. the cantilever deflection) then recorded and an image is produced. AFM can also be used in the tapping mode for imaging where the cantilever is driven up and down near its resonance frequency, at constant amplitude. This technique is however mostly used for force spectroscopy. The interaction forces of tip-sample are directly measured as a function of the distance between them. Forces as small as a few pNs can be measured with a sub-nanometer spatial resolution. But this resolution is not enough for the studies done in this thesis.

1.1.3 Optical Tweezers

Initially developed by Arthur Ashkin and coworkers in 1970, optical tweezers utilizes the laser lights momentum to trap objects ranging fom 0.3 to 30 microns in size. This method can detect the response of a single biomolecule to an applied force by detecting the distance changes in real time. Optical tweezers can apply forces from 0.02-250 pN and have spatial resolution of 0.2 nm 100μm, with a timescale ranging from 0.1 ms to more than 1000 seconds. This method is mostly used to study of the processive enzymes: molecular motors involved in key biological processes. A few examples are: kinesin, myosin, RNA and polymerases. Another major application is studying the folding dynamics of proteins. To do so, optical tweezers exert a mechanical force that tilts the energy landscape of the protein

towards the unfolded state. This method can be used in measuring the folding energy and kinetic of macromolecules (ZMZ13).

The setup is shown in Fig. 1.1. In this method a laser beam (usually in infrared region) is finely focused using a high-numerical-aperture objective and an optical trap is formed. There is a very strong electric field gradient at the beam waist (the narrowest part of the focused beam) and dielectric spherical beads in micron size (usually suspended in water) are attracted to the optical trap along this field gradient and become stably trapped in the focus point, the region of the strongest electric field. The beads are tethering the biomolecule under study. The biomolecule is connected to the bead from one end, and tethered to a fixed surface from the other end. The laser light applies a force on the beads in the direction of beam propagation, since the dielectric beads receive momentum from the photons that are absorbed or scattered by them. The setup is designed in a way that the displacement of beads from the trap center is small. For small displacement, the force applied to the bead is linearly proportional to the displacement and thus Hookes law can be applied.
For the purpose of this thesis, the limit with this method is the spatial resolution.

1.1.4 X-ray and Neutron Scattering

To measure the distance between atoms in a molecule, X-ray are the perfect rulers, since these distances range from 0.5 to 1.5 angstroms. In X-ray crystallography, the three dimensional structure of s particular protein is obtained by x-ray diffraction of the crystallized form of the protein. Since X-ray and covalent bonds have similar wavelength, X-ray crystallography can precisely reveal the three dimensional position of atoms in a molecule, specify the active sites and binding sites.
This method was first used to obtain the structure of myoglobin by Max Perutz and John Kendrew, who won the Nobel Prize in Chemistry in 1962. This method provides static images of the molecule, and cannot be used to study the dynamics.

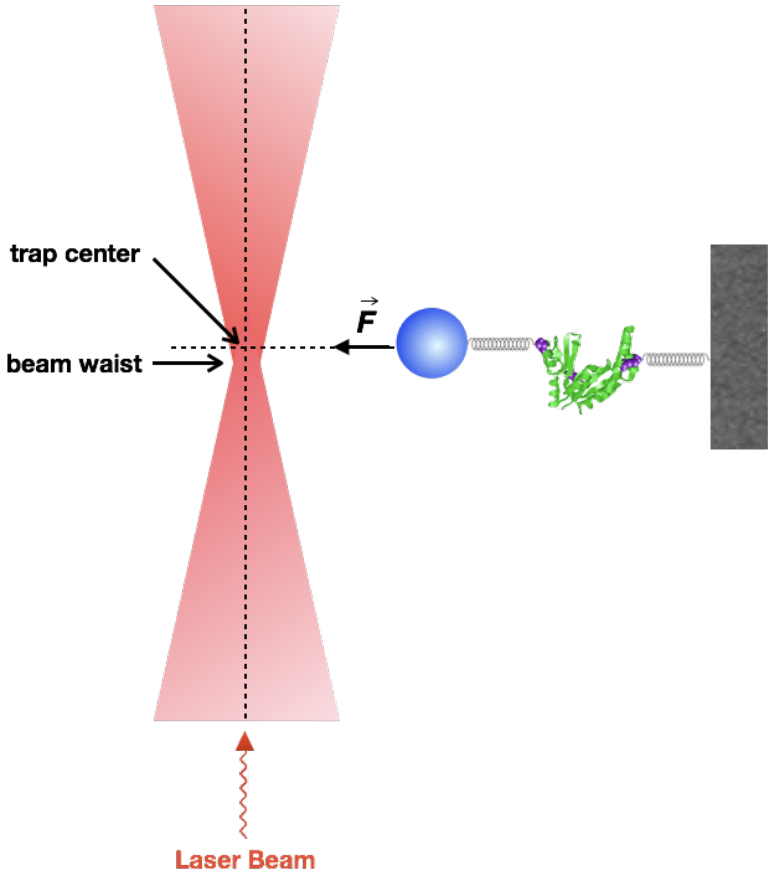

Figure 1.1: Schematic representation of Optical Tweezers. A laser beam (usually in infrared region) is finely focused and an optical trap is formed. There is a very strong electric field gradient at the beam waist and dielectric spherical beads are attracted to the optical trap along this field gradient and become stably trapped in the focus point, the region of the strongest electric field. The beads are tethering the biomolecule under study. The biomolecule is connected to the bead from one end, and tethered to a fixed surface from the other end. The laser light applies a force on the beads. The setup is designed in a way that the displacement of beads from the trap center is small. For small displacement, the force applied to the bead is linearly proportional to the displacement and thus Hookes law can be applied.

Neutron Scattering (also known as neutron diffraction or neutron crystallography) is similar to X-ray crystallography to some extent. This method relies on the wave-like diffraction of free neutrons. Neutrons are scattered by the nucleus in an atom (rather than electrons as in X-ray scattering) since neutrons have a natural strong affinity to react with the internal nuclei. In addition to obtaining the structure, this technique can also be used to provide information about the thermal motions of atoms. Vibrations can be induced using low energy neutrons.

1.1.5 NMR

Nuclear Magnetic Resonance is a spectroscopy technique based on the fact that atomic nuclei are intrinsically magnetic. The nuclei in a magnetic field absorb and re-emit electromagnetic radiation, whose energy is at a specific resonance frequency which is the characteristic of the isotope. The resonance frequency depends on the magnetic properties of the atoms which itself depends on the intermolecular magnetic field around the atom in the molecule. This dependency gives access to details of the electronic structure of a molecule. This technique can be used to reveal the structure, dynamics and chemical environment of biomolecules. Although NMR is limited to small molecules, it is advantageous compared to X-ray crystallography, mainly because it can be done in solution. The spatial resolution achieved with this method is a few nanometers. This technique can resolve the events that happen in pico-seconds to nano-seconds, but it cannot reveal the dynamics of slower processes.

CHAPTER 2

Nano-Rheology Experimental Setup

2.1 Introduction

In a typical macroscopic rheology experiment, the sample is under stress and the resulting strain is measured with a rheometer. Rheology is studying the flow of matter in response to an applied force. The idea is to do the same thing in nano-scale with proteins. In this chapter a nano-rheology technique is explained in details, which we use to investigate driven deformations of enzyme under an applied AC force. The enzyme under study is Guanylate Kinase which is introduced is section 2.2.1. In our nano-rheology setup, we aim to measure the ensemble averaged mechanical deformations with an extraordinary sub-Angstrom resolution.

In this setup the enzyme tethers surface modified gold nano-particles (GNP) to a gold-coated slide, which acts as the bottom plate of a fluid chamber. A second gold-coated slide is put on the top to form a parallel plates capacitor configuration. Instruction to make the chamber is explained in details in section 2.2.2. An AC voltage is applied across the electrodes which derive the negatively charged GNPs, as shown in Fig. 2.1. Oscillation of GNPs, which causes the enzyme deformation, is measured through evanescent wave microscopy explained in details in section 2.4.1. The setup is shown in Fig. 2.2

As shown in Fig. 2.2 a lock-in is used to apply AC voltage across the chamber, and also to measure the response in a phase-locked-loop which results in a great resolution. More details about the operation of the Lock-in can be found in section 2.3. An evanescent wave is produced in the buffer solution by total internal reflection of the laser beam in the prism.

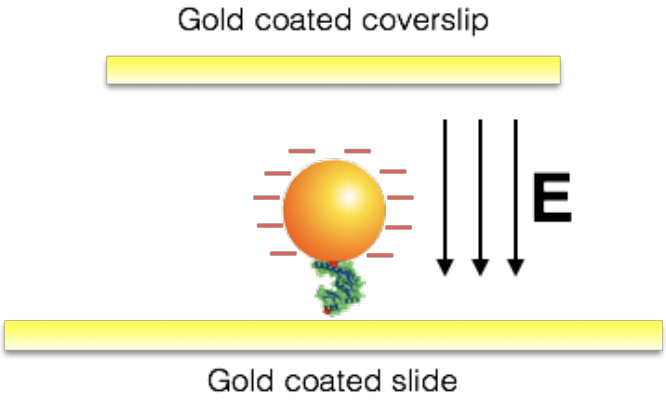

Figure 2.1: A force is applied on the sample by placing the negatively charged sample in between two conducting plates and apply a voltage across them.

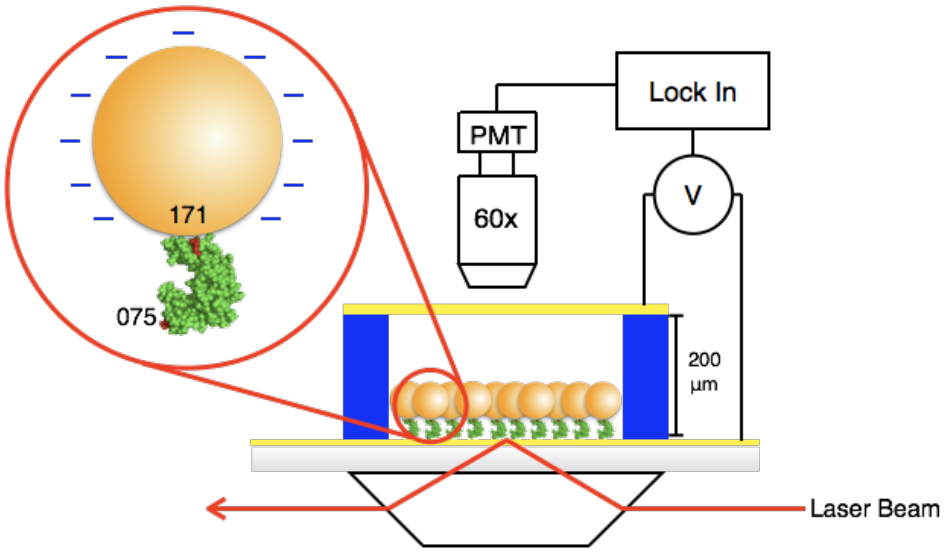

Figure 2.2: Nano-rheology setup, showing the flow chamber with enzyme-tethered GNPs, the parallel plates capacitor geometry used for mechanical excitation, and the evanescent wave scattering optics used for read out.

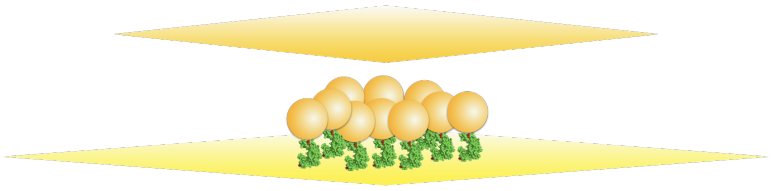

Figure 2.3: The enzyme is attached to the bottom plate of a parallel plate capacitor configuration, through S-Au bond. GNPs are tethered to the bottom plate through the enzyme, also through S-Au bond. There are ss DNAs on the surface of the GNPs to provide negative charge.

The evanescent wave in the buffer solution is then scattered by GNPs. The intensity of the scattered beam is detected by a photo-multiplier-tube and measured by lock-in-amplifier. Using this technique, a transition from linear elasticity to viscous dynamics as a function of driving force and frequency is observed. This transition is characterized in section 2.6.1.

In this chapter, I first go over sample preparation, then explain the measurement setup including the theory behind them, and finally represent the results with a model to interpret them.

2.2 Fluid Chamber Preparation

The experimental sample is a fluid chamber in a parallel capacitor configuration. The enzyme under study is anchored to the bottom plate of the chamber, through S-Au covalent bond, and tethers gold nano-particles, which are modified on the surface with ss DNAs in order to be negatively charged. Fig. 2.3 shows the configuration.

2.2.1 Brief Introduction to Guanylate Kinase

The enzyme used in this study is Guanylate Kinase from Mycobacterium tuberculosis, expressed and purified using the protocols in Chapter5. GK has ~ 200 amino acids, a molecular weight of ~ 24 kDa and a size of ~ 4 nm. This protein is the enzyme catalyzing the reac-

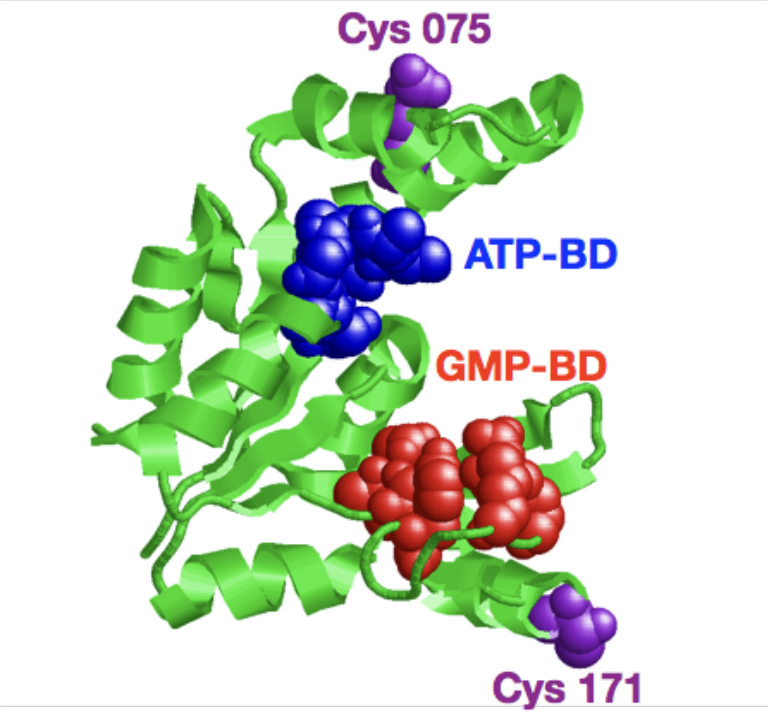

Figure 2.4: Structure of GK shown in cartoon representation, from PDB: 1S4Q. For this experiment two Cysteine residues were introduced diametrically at 075 and 171 sites (Thr-075-Cys; Arg-171-Cys) with mutagenesis. There is also a third Cysteine at 042, which was mutated unexpectedly and was discovered later. The Cysteines are shown in purple. The protein molecule attaches to the gold surface and GNP through the Cysteines. The GMP binding site is colored red, the ATP binding site blue.

tion of transferring a phosphate group from Adenosine Tri-Phosphate (ATP) to Guanosine Mono-Phosphate (GMP):

$$GMP + ATP \overset{\text{GK}}{\rightleftharpoons} GDP + ADP \tag{2.1}$$

Fig. 2.4 shows the crystal structure of GK.

Upon binding the substrates, the enzyme undergoes a conformational motion of ~ 1 nm, large compared to its size (SSS02). This substrate induced conformational change takes the enzyme from the open state to the close state as seen in Fig. 2.5. GMP induces most of

Figure 2.5: The open to closed conformational change GK upon binding substrate GMP. (PDB structures: 1ZNW for the open configuration and 1LVG for the close configuration) Colors are based on the secondary structure. Alpha helices are colored magenta and beta sheets are colored yellow. All other residues are colored white.

the conformational change (CZ07) (OB11). Fig. 2.4 shows the crystal structure of GK. For this experiment two Cysteine residues were introduced diametrically at 075 and 171 sites (Thr-075-Cys; Arg-171-Cys) with mutagenesis, a method explained in details in Chapter 5. The purpose of these mutations is to enable the enzyme to attach to gold. Cysteine has S-H group, which can bind to gold, by forming a strong covalent Au-S bond. Therefore these two cysteine residues will be the attachment points of the enzyme to the gold layer and GNPs. The DNA sequence obtained from Sanger Sequencing (done by GeneWiz company) and the corresponding aminoacid sequence of the molecule is shown in Fig. 2.6. The purple parts show the introduced Cysteines and the yellow part shows a third unexpected Cysteine.

Initially there were two Cysteines at 193 and 040, in the natural amino acid sequence of the protein, which were replaced by Arginine. Later we found out that there is a third Cysteine at 042 which had appeared unexpectedly in mutagenesis process. So there are three Cysteines in total that can bond to gold. Therefore we have a mixture of enzymes attached from different positions. If we call them C1 (at 075), C2 (at 171) and C3 (at 042), some enzymes are attached from C1 and C2, some from C1 and C3, and some from C2 and C3.

DNA sequence:

NNNNNNNNNNNNNNNNNNNNNNCNAGNNNNNNTTTGTTTNNNNNNAAGAAGGAGATATA
CAT
ATGGCTGTGAGCNNCNNNNNGGGNNNGGACACCAAGCCCACCGCGCGTGGCCAACCG
GCGGCAGTGGGACGTGTGGTGGTGCTGTCCGGTCCTTCCGCGGTCGGCAAATCCACGGTG
GTTCGGTCTCTGTGCGAGCGGATCCCGAATCTGCATTTCAGTGTCTCGGCCACGACGCGG
GCGCCACGCCCGGGCGAGGTCGACGGTGTCGACTACCACTTCATCGACCCCTGCCGCTTT
CAGCAGCTCATCGACCAGGGTGAGTTGCTGGAATGGGCAGAAATCCACGGCGGCCTGCAC
CGGTCGGGCACTTTGGCCCAGCCGGTGCGGGCGGCCGCGGCGACTGGTGTGCCGGTGCTT
ATCGAGGTTGACCTGGCCGGGGCCAGGGCGATCAAGAAGACGATGCCCGAGGCTGTCACC
GTGTTTCTGGCGCCACCTAGCTGGCAGGATCTTCAGGCCAGACTGATTGGCCGCGGCACC
GAAACAGCTGACGTTATCCAACGCCGCCTGGACACCGCGTGCATCGAATTGGCAGCGCAG
GGCGACTTTGACAAGGTCGTGGTGAACAGGCGATTAGAGTCTGCGTCTGCGGAATTGGTA
TCCTTGCTGGTGGGAACGGCACCGGGCTCCCCGGGTGTACCACGAGGTAAGCTTGCGGCC
GCACTCGAGCACCACCACCACCACCACTGAGATCCGGCTGCTAACAAAGCCCGAAAGGAA
GCTGAGNTGGCTGCTGCCACCGCTGANCAATAACTAGCATAACCCCTTGGGGCCTCTAAA
CGGGTCTTGAGGGGTTTTTTGCTGAAAGGAGGAACTATATCCGGATTGGCGAATGGGACG
CGCCCTGTAGCGGCGCNNTAAGCGCGGCGGGNGTGGTGGTTACGCGCAGCGNGACNNCTA
CACTTGCCAGCGCCCTAGCGCCCGCTCCTTTCGCTTTTCTTCCCNTTCCTTTNNNNNCNN
NNNNNNCNGNTTNCCCGTCAAGCTCTAAATCNNGGGNNNCCNTTAGGNNNCNNTTNNNNN
NTTNNNNNNCNNCNACCCNAAAAANNNGANNNNNNNNANGNNNNNNNNNNNNNNNNNNN
NNNANNNANNNTNNNNNNNNNNNNNNGNNNCNNNNNNNNNNNNNNNNNNNNNNCNANN
NNNNNNNNANNNNNNNNNNN

Protein sequence:

MAVSXXXXXD TKPTARGQPA AVGRVVVLSG PSAVGKSTVV RSLCERIPNL HFSVSATTRA
PRPGEVDGVD YHFIDPCRFQ QLIDQGELLE WAEIHGGLHR SGTLAQPVRA AAATGVPVLI
EVDLAGARAI KKTMPEAVTV FLAPPSWQDL QARLIGRGTE TADVIQRRLD TACIELAAQG
DFDKVVVNRR LESASAELVS LLVGTAPGSP GVPRGKLAAA LEHHHHHH

Figure 2.6: DNA sequence obtained from Sanger Sequencing (done by GeneWiz company) and the corresponding aminoacid sequence of the GK molecule under study. The purple parts show the introduced Cysteines and the yellow part shows a third unexpected Cysteine.

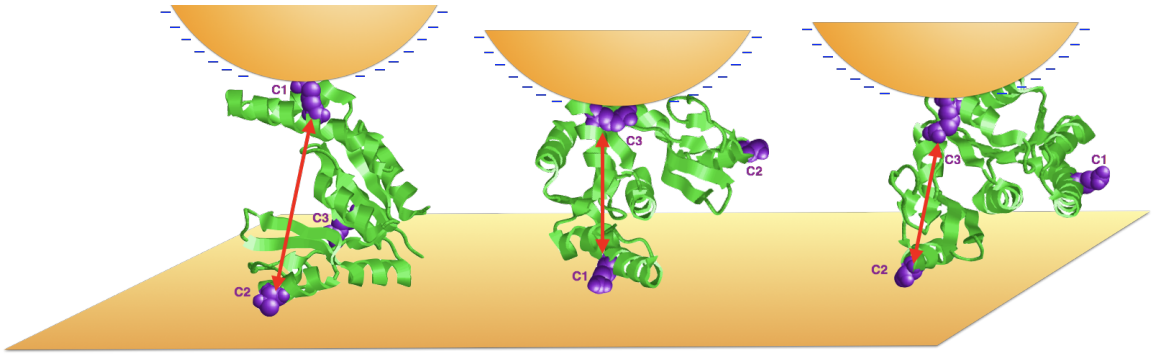

Figure 2.7: There are three Cysteines in total that can bond to gold. Therefore we have a mixture of enzymes attached from different positions. If we call them C1 (at 075), C2 (at 171) and C3 (at 042), some enzymes are attached from C1 and C2, some from C1 and C3, and some from C2 and C3. C3 at 042 had appeared unexpectedly in mutagenesis process. However since the third Cysteine is relatively buried, C1-C2 orientation is the most probable and therefore the average deformation is dominated by deformation along this orientation

Fig. 2.7 shows the configuration. The measured deformation is the average of deformations along these three possible orientations. However since the third Cysteine is relatively buried, C1-C2 orientation is the most probable and therefore the average deformation is dominated by deformation along this orientation. Using point mutation, I removed the third Cysteine, but the mutated enzyme did not attach to gold as well as the enzyme with 3 Cysteines. The importance of the measurements is still valid: although the measured deformation is not entirely along a specific orientation, but it still can help to understand the dynamics.

2.2.2 Construction of the Chamber

Gold coated slides and coverslips are prepared by evaporating 3 nm Cr followed by 30 nm Au on glass slides and coverslips usen an e-beam evaporator machine . Preparing the flow chamber takes 3 days. On the first day, protein is first diluted to a final concentration of 2 μM in KH_2PO_4 1M pH 7. This is the optimum pH which minimizes the nospecific binding of GK to gold (WZ10). Using a barrier pen (Aqua-Hold Pap Pen from Fisher Scientific) a rectangular barrier is drawn on the gold slide, measuring $\sim$ 1 cm $\times$ $\sim$ 4 cm. Then 500 μL of the protein

solution is inserted into the bordered area for overnight at room temperature. On the second day the slide is first rinsed with a large amount of DI water in order to remove the unbound proteins. After that the slide is immersed in a Native Wash buffer solution containing 0.5 mM TCEP (3,3',3"-Phosphanetriyltripropanoic acid from Thermo Fisher Scientific) for $\sim$ 30 minutes in order to break the dimer bonds and reduce the protein. The slide is then rinsed once again and immersed in 20 nm GNP (from Nanocs) for $\sim$ 80 minutes. When GNP is bound the slide turns slightly red. In order to put negative charge on the gold nano-particles the slide is then immersed in KH_2PO_4 1M pH 4 containing 2 μM thiol-modified ss DNA (from IDT-DNA), for overnight. The DNA sequence is /5ThioMC6-D/AAAAAAAAAAAAAAAAAAA ACGCATTCAGGAT. Thiol-modification enables the DNA to bind to gold because of the S-H group. Finally on the third day, first the unbound DNA is washed away with a large amount of DI water and then the slide is immersed in 500 μL SSC/3 (Sodium Saline Citrate buffer from Invitrogen).

Now we have to make the chamber. First a gold-coated coverslip is rinsed with ethanol and water and dried with nitrogen gas. Then two metal wires are soldered to the slide and the coverslip to be used as the electrodes. Two spacers (200 μm thick) are placed next to the barred area on the slide. Then the coverslip is perpendicularly placed and glued (using epoxy glue) on top of the slide, gold layers facing each other. The volume of the cell is between the plates is $\sim$ 20 μL. Fig. 2.8 shows the configuration. When the flow chamber is now ready to be used for measurements, it is placed on top of the prism and optically locked with the prism using immersion oil.

The electrode from the coverslip is grounded and the electrode from the slide is connected to the Sine-Out port of the Lock-In and an AC voltage is applied to the chamber through these electrodes.

2.2.3 Flow Chamber: A Double Layer Capacitor

Electrically, the chamber can be treated as a resistor R (contact resistance at the interface) in parallel to a capacitor C (due to the double layer formed at the interface) and then the

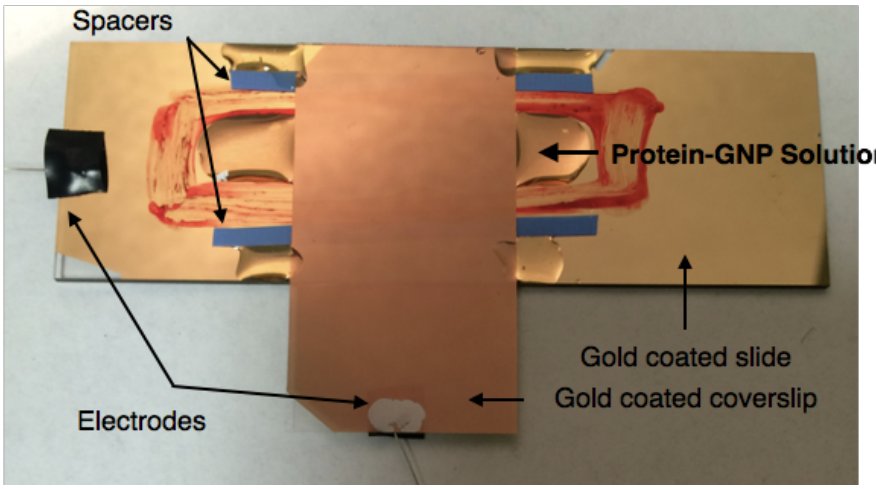

Figure 2.8: Flow Chamber constructed by two gold-coated surfaces. The spacers are 200 μm thick resulting in a $\sim$ 20 μL volume between the plates. Two metal wires are soldered to the plates to be used as electrodes.

parallel RC combination in series with a much smaller resistor r (resistance of the bulk), as shown in Fig. 2.9. For the RC part, the impedance is written as

$$\frac{1}{Z} = \frac{1}{R} + i\omega C \Rightarrow |Z| = R\sqrt{\frac{1}{1+(R\omega C)^2}} \tag{2.2}$$

Therefore the current is

$$I = \frac{|V|}{R}\sqrt{1+(R\omega C)^2} \simeq |V|\omega C \quad \text{for} \quad R\omega C \gg 1 \tag{2.3}$$

Measuring the current vs different frequencies of the applied voltage, at fixed $|V|$ gives us the value of C. The current was measured by putting a 200 Ω resistor in series with the chamber and measuring the voltage across the new resistor. C was found to be $\sim$ 100 μF. The DC resistance of the cell is measured to be $\sim$ 1 MΩ. Therefore $R\omega C$ is in fact much bigger than 1 for frequencies higher than 10 Hz, i.e. the assumption in Eq. 2.3 is valid.

The force deriving GNPs is $F = F_0\ e^{i\omega t}$ due to the electric field $E = E_0\ e^{i\omega t}$ which is generated by the applied AC voltage $V = V_0\ e^{i\omega t}$. The amplitude of the driving force F_0 is simply Q $\times$ E_0, Q being the effective charge of the particle. However the effective charge

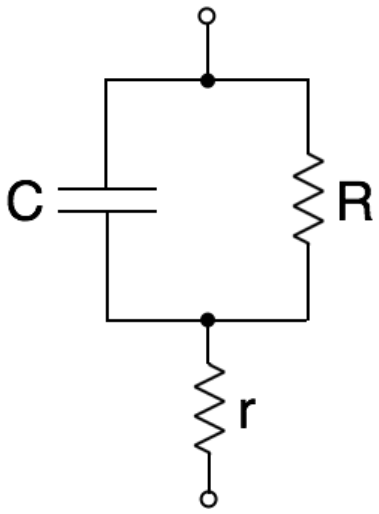

Figure 2.9: The equivalent circuit of the fluid chamber, which is a capacitor C in parallel with a resistor R and then in series with a much smaller resistor r. The capacitor C represents the capacitance from the double layer in the solution, measured to be $\sim 100\ \mu$F, the resistor R corresponds to the contact resistance at the interface, measured to be 1 MΩ, and the resistor r is for the resistance in the bulk solution, estimated to be around 1 Ω.

and the magnitude of the electric field are not easily calibrated due to the complexity of the system. Exposing a conducing plate (gold-coated slide in this experiment) to a fluid containing ions (SSC buffer in this experiment) results in the appearing of a double layer at the interface. In this situation two parallel layers surround the surface of the plate. The first layer is composed of the ions absorbed to the surface due to chemical interactions. The second layer is composed of opposite charged ions attracted to the first layer due to Coulomb force. This second layer screens the first layer electrically. This phenomenon is one of the reasons for the complexity of calculating the effective charge Q in our experiment (Gra47; OB83a; Con06).

The electric potential in a double layer decays exponentially according to Gouy-Chapman model, as shown in Fig. 2.10. In this model, diffusion of the second layer is considered, and Maxwell-Boltzmann statistics is applied to the charge distribution with respect to the distance from the interface, which results in the exponential decay of the electrical potential,

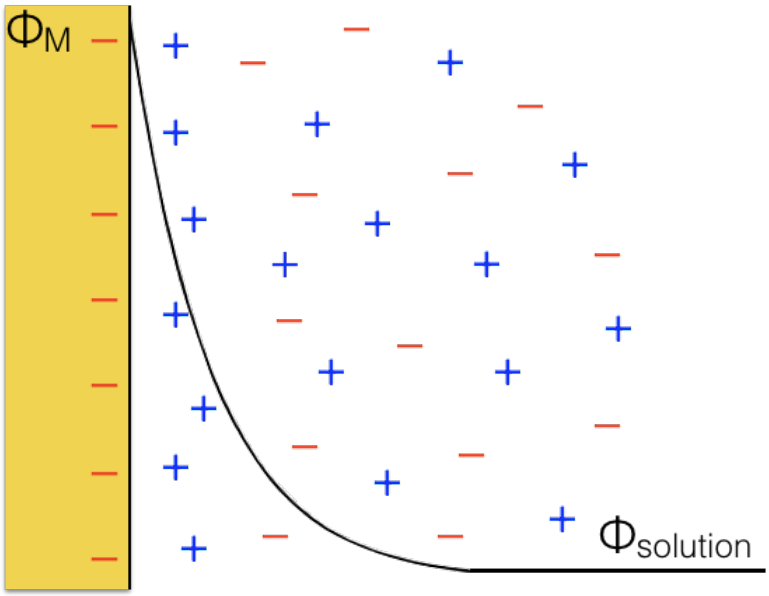

Figure 2.10: The Gouy Chapman diffuse layer model of an electrical double layer. The ions in the solution have Boltzmann distribution. The electric field is localized in the vicinity of the interface, within 1$\sim$ 2 nm and decays exponentially deeper in the solution.

as we get further away from the interface and go into the bulk of the fluid (Con06; Deb88).

$$\Phi(x) \simeq \Phi(0) \text{ exp } (\text{-x}/\lambda) \tag{2.4}$$

where λ ,obtained from the Debye-Huckel equation (Deb88), is a characteristic length scale.

$$\lambda = \sqrt{\frac{\epsilon k_B T}{2 N_A e^2 c}} \tag{2.5}$$

where ϵ is the permittivity of the electrolyte, k_B is the Boltzmann constant, T is the temperature, N_A is the Avogadro number, e is the elementary charge and c is the ionic strength of the electrolyte (55 mM for the SSC/3 buffer in this experiment). Plugging all the numbers in the Debye length of this setup is $\lambda \simeq 1 \sim 2$ nm.

From Eq. 2.4 the electric field can be written as

$$E(x) = -\frac{d}{dx}\Phi(x) \simeq \frac{\Phi(0)}{\lambda} \text{ exp } (\text{-x}/\lambda) \tag{2.6}$$

Eq. 2.6 shows that the electric field varies very much is the range we are interested in: 4 nm $\sim$ 10 nm. It is also concluded that the particles in the vicinity of the interface feel most

of the force, since the electric field is localized in that region. Also because the resistance in the bulk is much smaller, most of the voltage drop is across the double layer. The electric field is smaller by a factor of r/R $\sim 10^{-6}$, and therefore the beads in the feel a negligible force.

2.2.4 Hydrodynamic Properties

As the gold nano-particles move in the buffer solution, hydrodynamic friction of these particles becomes relevant. For a spherical particle close to a planar surface, the hydrodynamic friction coefficient γ_0 , from a numerical or analytical approach, can be approximated as (Bre61; Mau61; OB83b)

$$\gamma_0 = 6\pi\eta R \times (1 + \frac{9}{8}\frac{R}{h} + O\big[(\frac{R}{h})^2\big] \tag{2.7}$$

where R is the radius of the particle, h is the distance from the surface (calculated from the bottom of the particle) and η is the viscosity term. If the particle is far from any surfaces, the Stokes friction constant can simply be written as

$$\gamma_0 = 6\pi\eta R \tag{2.8}$$

In our experiment, because of the surface modifications (i.e. ss DNAs) , the effective radius of GNPs and the effective viscosity of the solution surrounding the particles, is modified. Furthermore the particles do not have a flat surface due to the presence of packed proteins and DNA coils. Therefore the hydrodynamic friction is not straightforward to be calculated.

The other hydrodynamic property worthy to be discussed, is the Reynolds number, Re. This dimensionless number provides the ratio between inertial and viscous effects in a fluid flow. Reynolds number is helpful in determining if the transfer of momentum in a fluid is due to the motion of fluid elements or due to the frictional stressed within the fluid. The inertial effect is considered as the change of momentum due to acceleration

$$\Delta P_i = F_i \Delta t \text{ where } F_i \sim \rho l^3 \times \frac{dv}{dt} \sim \rho l^3 \times \frac{v}{l} \sim \rho v l^2 \tag{2.9}$$

The viscous effect is the change in momentum due to the frictional forces

$$\Delta P_f = F_f \Delta t \text{ where } F_f \sim \eta l \tag{2.10}$$

Using Eq. 2.9 and Eq. 2.10 the Reynolds number can be written as

$$Re = \frac{\Delta P_i}{\Delta P_f} = \frac{F_i}{F_f} = \frac{\rho v l}{\eta} \tag{2.11}$$

If the Reynolds number is small it means that inertial effect is dominated by viscous effect. In this experiment, the length scale of the system is the size of the protein (or GNP) $l \sim 10nm$, $v \sim l/t \sim l\omega \sim 10^3 nm/sec$, $\rho \sim 20^3 kg/m3^3$ (using the density of GNP, since it has the maximum density in this system) and $\eta \sim 10^{-3} Pa.s$ (in the order of water viscosity). Putting these values in Eq. 2.11 we obtain the Reynolds number of this system.

$$Re = \frac{\rho v l}{\eta} \sim 10^{-4} \ll 1 \tag{2.12}$$

It is therefore concluded that the fluid in our system is dominated by the viscous effect and the inertial effect (e.g. $m\ddot{z}$ in equation of motion) is negligible. Furthermore in case of gold nano-particles the mass itself is very small.

2.3 Lock In Amplifier (LIA)

2.3.1 Phase Sensitive Detection using LIA

Lock in amplifiers are used to measure very small AC signals, as small as a few nano-volts, even if the signal is obscured by noise sources way larger than the signal. The technique Lock in Amplifier employs to do so is a phase and frequency sensitive detection, meaning that it singles out the component of the signal at a specific phase and frequency of reference. Noise signals that are not at the frequency of the reference will be rejected and thus will not affect the measurement. Therefore there is always a frequency reference required. Also it is noteworthy that lock-in displays the signals in Volts RMS, frequencies in Hz and phases in degrees.

In our case, the experiment is excited at a specific frequency of the reference (a.k.a. the frequency of the applied force) and the lock-in detects the response signal from the experiment at that frequency, i.e. $\omega_{reference} = \omega_{signal}$. To achieve this lock-in generates its own sine wave according to the reference signal, or in our case since the reference signal is a sine wave the lock-in wave will be equal to the reference wave. Let us consider the reference (which is also the lock-in wave) and the response signal as below:

$$\begin{aligned} \text{Reference} &= V_r sin(\omega_r t) \\ \text{Response Signal} &= V_s sin(\omega_s t + \theta_s) \end{aligned} \tag{2.13}$$

Notice that in writing Eq. 2.13 I have treated the reference signal as the reference for measuring the phase, i.e. $\theta_r = 0$ and θ_s is the phase difference between the reference and the signal.

The lock-in amplifies the signal and then multiplies it by the reference using a phase sensitive detector (PSD), as below:

$$\begin{aligned} V_{PSD} &= V_r V_s sin(\omega_r t) sin(\omega_s t + \theta_s) \\ &= \frac{1}{2} V_r V_s cos([(\omega_r - \omega_s]t + \theta_s) - \\ &\quad \frac{1}{2} V_r V_s cos([(\omega_r + \omega_s]t + \theta_s) \end{aligned} \tag{2.14}$$

Now if we pass the PSD output through a low pass filter, which passes signals with a frequency lower than a certain cutoff frequency and attenuates signals with frequencies higher than the cutoff frequency, the second term of the RHS of Eq. 2.14 is removed and the first term is remained only if $\omega_r = \omega_s$. Thus we are left with:

$$V_{PSD} = \frac{1}{2} V_r V_s cos(\theta_s) \tag{2.15}$$

The output is a nice DC signal proportional to the signal amplitude and depends on the phase difference between the applied force and the measured response. To eliminate this dependency lock-in uses a second PSD, which multiplies the signal by the reference shifted by 90°, i.e. $V_r sin(\omega_r t + 90)$, pass it through a low pass filter, like Eq. 2.15 the output will be:

$$V_{PSD_2} = \frac{1}{2} V_r V_s sin(\theta_s) \tag{2.16}$$

Now we have two outputs, one proportional to the sine of the phase difference and one proportional to the cosine of it. Defining X and Y as

$$X = Vcos(\theta_s) \quad \text{and} \quad Y = Vsin(\theta_s) \tag{2.17}$$

we have the detected signal as a vector relative to the lock-in reference. Lock-in measures X and Y and we can obtain a measure of the magnitude and the phase of the signal as below:

$$R = \sqrt{X^2 + Y^2} = V \quad \text{and} \quad \theta_s = tan^{-1}(\frac{Y}{X}) \tag{2.18}$$

Throughout this thesis I use φ as θ_s interchangeably.

Notice that if the input signal is the reference signal plus some noise, the low pass filter will remove the part of the noise that has a frequency far from the reference frequency. Noise at frequencies close to the reference frequency ($|\omega_r - \omega_{noise}|$ is small) might be attenuated depending on the band width of the low pass filter. There will be more discussion on this in section 2.3.2.

Also notice that in Eqs. 2.14 and 2.15 the phase difference θ_s cannot change in time, or else we will not have a DC signal. Therefore lock-in amplifier uses a phase-locked-loop (PLL) to be phase-locked to the signal reference, regardless of whether the reference is internal or external. The PLL actively tracks the reference signal and makes sure that the sine wave generated by lock-in is in phase with the signal reference.

2.3.2 Johnsons Noise

In every resistor there is thermal fluctuations in the electron density within the resistor. These fluctuations give rise to a noise voltage across the terminals of the resistor:

$$V_{noise}(rms) = \sqrt{4kTR\Delta f} \tag{2.19}$$

Where K=Boltzmanns constant, T is the temperature in Kelvin, R is the resistance in Ohms and Δf is the bandwidth of the measurement in Hz. The equivalent noise band width

(ENBW) obtained from the low pass filter and time constant sets the detection bandwidth in Lock In. Therefore Eq. 2.19 can be written as:

$$V_{noise}(rms) = 0.13\sqrt{R}\sqrt{ENBW}nV \tag{2.20}$$

Lock In has 4 first order RC type low pass filters with a 6dB/Oct roll off each. A 1second time constant referred to a filter whose -3 dB point occurred at 0.16 Hz and rolled off at 6 dB/Oct beyond 0.16 Hz.

Given a filter with transfer function $H(j\omega)$ the equivalent noise bandwidth of a first order low pass filter is defined as:

$$\omega_{enbw} = \int_0^\infty |\frac{H_{j\omega}}{H_{max}}|^2 d\omega \tag{2.21}$$

where H_{max} is the maximum value of the transfer function. For a first order low pass filter:

$$\begin{aligned} H(j\omega) &= \frac{H_{max}}{1 + j\frac{\omega}{\omega_c}} \\ \omega_{enbw} &= \int_0^\infty \frac{1}{1 + (\frac{\omega}{\omega_c})^2} d\omega \end{aligned} \tag{2.22}$$

Now if we use all the filters $H(j\omega) = \frac{H_{max}}{(1+j\frac{\omega}{\omega_c})^4}$ and Eq. 2.21 becomes:

$$\omega_{enbw} = \int_0^\infty \frac{1}{1 + (\frac{\omega}{\omega_c})^4} d\omega = \frac{5\pi}{32}\omega_c \tag{2.23}$$

For these filters $\omega_c = 1/2\pi T$ where T is the time constant. Therefore if we use 24 dB/Oct (cascading all the for filters) and 100ms as the time constant, then:

$$\Delta f_{ENBW} = \frac{5\pi}{32}\frac{1}{2\pi 100msec} = 781mHz \tag{2.24}$$

Putting the corresponding Δf in Eq. 2.20 gives $\simeq 100nV$ of voltage noise.

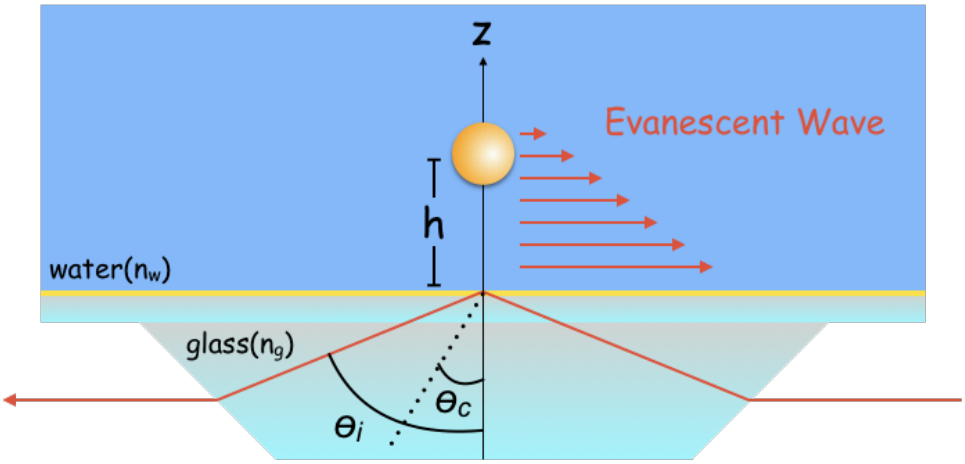

Figure 2.11: Evanescent wave produced in the buffer solution. Laser beam (in red) hits the prism at angle of θ_i greater than the critical angle θ_c. It gets totally internally reflected at the glass-water interface and produces evanescent wave in water, traveling parallel to the interface. The intensity of the evanescent wave decreases as we get further away from the origin (glass-water interface). The wave gets scattered by the gold nano particles (golden sphere in the picture) and the intensity of the scattered wave gives the value of h, i.e. the distance between the GNP and the interface. The figure is not in to scale.

2.4 Detection Techniques

2.4.1 Evanescent Wave Scattering

In our experimental setup the deformation of the protein is measured via evanescent wave scattering of gold nano-particles. A laser beam hits the prism, gets totally internally reflected at the interface of the prism and water and an evanescent wave is produced. The evanescent wave is then scattered by the gold nano-particles and the intensity of the scattered beam is detected by photo multiplier tube (PMT). In this section the detailed of this phenomenon is discussed.

The concept is shown in Fig. 2.11

Laser beam hits the prism at angle of θ_i greater than the critical angle θ_c. It gets

totally internally reflected at the glass-water interface and produces evanescent wave in water, traveling parallel to the interface.

Critical angle θ_c for total reflection is given by

$$\theta_c = sin^{-1}\ (\frac{n_w}{n_g}) \tag{2.25}$$

In Fig.2.11 as Snells law dictates we have

$$\begin{aligned} n_g \sin\ \theta_i &= n_w \sin\ \theta_r \\ \Rightarrow \sin\ \theta_r &= \frac{n_g}{n_w} \sin\ \theta_i \end{aligned} \tag{2.26}$$

Now since θ_i is greater than θ_c we have $\sin\ \theta_i > \sin\ \theta_c$ and from Eq. 2.25 we have $\theta_i > \frac{n_w}{n_g}$. Putting this result back in Eq. 2.26 we can write

$$\begin{aligned} \sin\ \theta_r &> \frac{n_g}{n_w} \times \frac{n_w}{n_g} \\ \Rightarrow\ \sin\ \theta_r &> 1 \Rightarrow \theta_r \text{ is complex.} \end{aligned} \tag{2.27}$$

which has a cosine of (from Eq. 2.26)

$$\cos\ \theta_r = i\sqrt{\Big(\frac{\sin\ \theta_r}{\sin\ \theta_c}\Big)^2 - 1} \tag{2.28}$$

For the electric field of a refracted beam, propagating in the buffer medium traveling in the transverse z direction, from (Jac98), we have

$$E_r(\vec{r},t) = \mathrm{E}'\ \exp(i\vec{k}'.\vec{r} + i\omega t) = \mathrm{E}e^{ik'(\mathrm{x}\ \sin\ \theta_r + \mathrm{z}\ \cos\ \theta_r) + i\omega t} \tag{2.29}$$

where $\vec{k}'$ is the wave vector of the refracted beam inside the buffer medium. Substituting Eq. 2.28 in Eq. 2.29 gives

$$E_r(\vec{r},t) = \mathrm{E}'\ \exp\Big[-k'z\sqrt{\Big(\frac{\sin\ \theta_r}{\sin\ \theta_c}\Big)^2 - 1}\Big]\exp\Big[ik'\Big(\frac{\sin\ \theta_i}{\sin\ \theta_c}\Big)x\Big] \tag{2.30}$$

Looking at Eq. 2.32, the magnitude of the field decreases with z, i.e. the evanescent wave decay exponentially in the buffer medium as we get further away from the interface. The characteristic length, δ is given by

$$\delta_e = 1/\Big[k'\sqrt{\Big(\frac{\sin\ \theta_r}{\sin\ \theta_c}\Big)^2 - 1}\Big] = \frac{1}{k\sqrt{sin^2\ \theta_i - sin^2\ \theta_c}} \tag{2.31}$$

where $\vec{k'}$ is the wave vector of the refracted beam inside the buffer medium. Substituting Eq. 2.28 in Eq. 2.29 gives

$$E_r(\vec{r},t) = \mathrm{E'}\ \exp\Big[-k'z\sqrt{\Big(\frac{\sin\,\theta_r}{\sin\,\theta_c}\Big)^2-1}\Big]\exp\Big[ik'\Big(\frac{\sin\,\theta_i}{\sin\,\theta_c}\Big)x\Big] \tag{2.32}$$

$$\delta_e = 1/\Big[k'\sqrt{\Big(\frac{\sin\,\theta_r}{\sin\,\theta_c}\Big)^2-1}\Big] = \frac{1}{k\sqrt{sin^2\,\theta_i\,\text{-}\,sin^2\,\theta_c}} \tag{2.33}$$

where $\vec{k}$ is the wave vector of the incident beam (k'/k = n_w/n_g = sin θ_c).

The evanescent wave is then scattered by the gold nano-particles in the buffer solution as shown in Fig. 2.11. For a single gold nano-particle, a sphere, with a distance h from the surface the differential scattering cross section is (Jac98)

$$\frac{d\sigma}{d\Omega} = \frac{k'^4}{|4\pi\epsilon_0 E|^2}|\vec{\epsilon^*}.\vec{p} + (\vec{n}\times\epsilon^*).\vec{m}/c|^2 \tag{2.34}$$

where $\vec{m}$ is the magnetic dipole moment of GNP, $\vec{p}$ is the electric dipole moment of GNP, $\vec{\epsilon}$ is the polarization of the electric field and $\vec{n}$ is the unit vector in the direction of scattered radiation. Treating gold nano-particles as perfect conducting spheres we have (Jac98) $\vec{p}$ = 4 $\pi\epsilon_0 R^3\ \vec{E}$ and $\vec{m}$ = -2$\pi R^3\ \vec{H}$, though we are going to neglect the magnetic dipole moment due to the 1/c term. R is the radius of a single gold nano-particle. In our experiment, the polarization of the laser beam is along the z-axis. Substituting $\vec{p}$ in Eq.2.34 gives

$$\frac{d\sigma}{d\Omega} \propto k'^4 R^6 \tag{2.35}$$

The total intensity of the scattered light from a single gold nano-particle is given by

$$\mathrm{I\ (z)} = \int \frac{d\sigma}{d\Omega} \times |\vec{E}(z)|^2 d\Omega\ \propto\ k'^4 R^6 |E'|^2 e^{-2z/\delta_e}\ \propto\ I_0\ e^{-z/\delta} \tag{2.36}$$

where $I_0 = k'^4\ R^6\ |E'|^2$ and $\delta = \delta_e/2$ is the penetration depth of the evanescent wave in the buffer solution.

Having $\theta_i \simeq 73^\circ$, $n_g \simeq 1.52$, $n_w \simeq 1.33$, and $\lambda_0 = 488$ nm and using Eq. 2.33 the penetration depth can be calculated.

$$\delta = \frac{1}{2k\sqrt{sin^2\ \theta_i \text{ - } sin^2\ \theta_c}} = \frac{\lambda_0}{4\pi\sqrt{{n_g}^2 sin^2\theta_i - {n_w}^2}} \simeq 64nm \tag{2.37}$$

Therefore the beam is localized in the vicinity of the interface. It is worthy to note that the average distance of a gold nano-particle from the interface (i.e. z in the equations above) is ~ 4 nm, the size of a GK protein. Therefore the penetration depth is much further away from the interface than an average gold nano-particle. Also the oscillation of a gold nano-particle is a few Angstrom (the amount of deformation of the protein), which is very small compared to the penetration depth and thus we can write

$$I(z+\Delta z) = I_0\ e^{-(z+\Delta z)/\delta} = I(z)\ e^{-\Delta z/\delta} \simeq\ I(z)\ (1-\Delta z/\delta) \tag{2.38}$$

which means as we get further from the interface by Δz the intensity of the scattered wave field decreases by I(z) Δz/δ. Therefore

$$\Delta z = \frac{\Delta I}{I}\ \delta \tag{2.39}$$

This simple equation enables us to measure the $\mathring{A}$ size deformation of protein, namely Δz, by measuring the change in the intensity of the scattered wave field.

In the actual measurement, I is first measured when no force is applied and GNPs are, on average, fixed at a specific height (e.g. h). To do so, the laser beam is chopped with a fan at 200 Hz and the lock-in is in external mode meaning it uses an external source (i.e. the fan) as the reference frequency, so that the intensity chopped at 200 Hz has the same frequency as the reference and can be measured accurately.

Then the fan is removed and the AC force is applied which oscillates the GNPs around h by Δz at a frequency of ω. We will see in section 2.6.1 that $\Delta z(\omega) = |\Delta z(\omega)|\ sin(\omega t + \phi)$ (in that section we use different notation, z is used instead of Δz and $|z_0|$ is used instead of $|\Delta z|$). Therefore when the force is applied and GNPs move, we can write

$$I(h+\Delta z) = I_0\ e^{-(h+\Delta z)/\delta} = I(h)\ e^{-\frac{|\Delta z|}{\delta} sin(\omega t+\phi)} \simeq\ I(h) - I(h)\frac{\Delta z}{\delta} sin(\omega t+\phi) \tag{2.40}$$

where we have used the estimation $\delta \gg \Delta z$. In this situation with GNPs oscillating, when LIA measures the intensity $I(h+\Delta z)$ using the frequency of the applied force as the reference frequency (i.e. ω), it measures $I(h)\frac{\Delta z}{\delta} sin(\omega t + \phi)$, the component that is oscillating at the same frequency as the reference frequency, which is ΔI. Now that we have the measured I and ΔI we can find Δz (or $|z_0|$ according to the notation of section 2.6.1) using Eq. 2.39.

2.5 Surface Plasmon Resonance

To improve the detection technique, and thus be able to detect smaller conformational changes (i.e. upon ligand binding) we take advantage from Surface Plasmon Resonance (SPR) phenomenon.

When a metal is in contact with a dielectric, the real part of the dielectric function changes sign as we cross the interface. There are coherent delocalized electron oscillations at the interface. These propagating mode of electron oscillations are called surface plasmons. Rufus Ritchie was the first one to predict the existence of these surface plasmons in 1957. One can excite these plasmons by transferring energy to them. One way to do so is using light. If the wavelength of the light used for excitation is larger than the size of a nanoparticle, the plasmons on the surface of the particle are confined and result in Localized Surface Plasmons (LSP). In this case the electric field near the particle surface is greatly enhanced and decays rapidly with distance from the interface. The concept is shown in Fig. 2.12

For a photon to excite a surface plasmon they both need to have the same frequency and momentum. For a specific frequency this condition cannot be achieved since the photon and the surface plasmon are in different mediums and have different dispersion relations. To adjust this mismatch, a coupling medium can be used, such as a prism(KR68; Ott71). Fig. 2.13 shows how this coupling is done. This is the method that we use for detection in SPR mode.

In our setup the gold layer is 30 nm and the light used for SPR mode is 632 nm in wave-

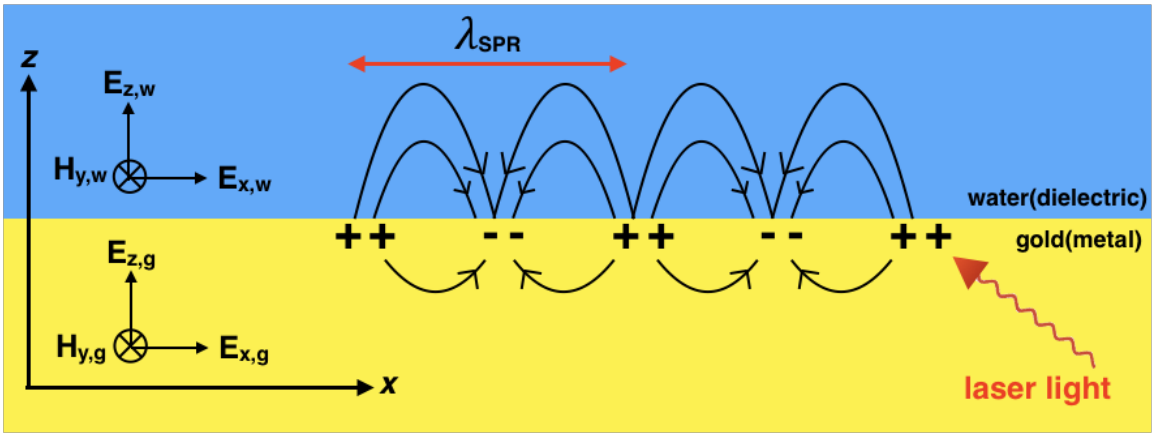

Figure 2.12: Electron density wave propagating along the gold-water (metal-dielectric) interface. These oscillations can be excited by shining light in visible range. At a particular wavelength of light, the oscillations resonate which results in an enhanced field near the surface. The field decays rapidly as it gets further away from the interface.

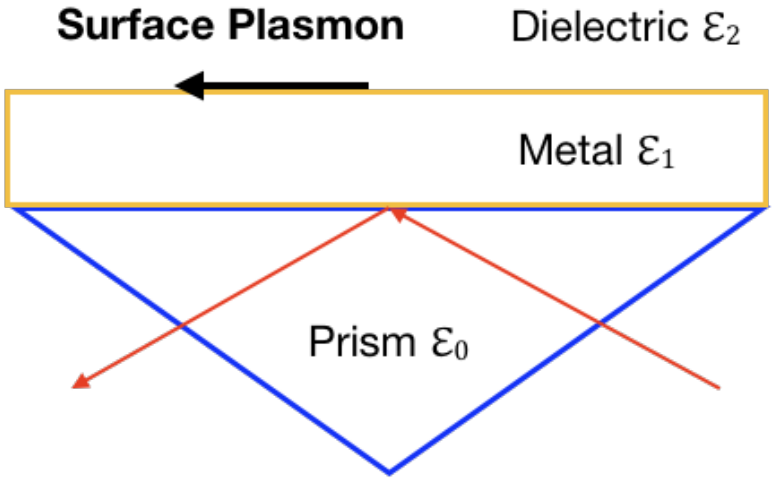

Figure 2.13: For a photon to excite a surface plasmon they both need to have the same frequency and momentum. But since they are in different mediums and have different dispersion relations, to achieve this condition a coupling medium (i.e. a prism in this case) is needed.

length. This wavelength is close to the SPR mode of the of the gold layer and illuminating with this light results in resonating the oscillations of surface plasmons. We can think of this phenomenon as a dipole field produced by the gold layer which, with near field interaction, induces a corresponding dipole in the GNPs. Since GNPs are 20nm in size, the SPR mode of GNPs and gold layer are very close. GNPs then radiate. The induced dipole interactions are distance related and thus the intensity of this radiation also depends on distance (between the gold layer and the GNP). Induced dipole interactions are proportional to $1/r^6$, and thus is the radiated intensity. Compared to EWS explained in section 2.4.1 where $I \propto exp(-r/\delta)$, here the intensity is way more sensitive to distance changes which makes it possible to measure the small changes in the conformation.

Fig. 2.14 (adapted from (AZ15)) shows the mechanical response of the enzyme to an oscillatory applied force measured in two ways: blue circles are measurements in EWS mode and red squares are measurements in SPR mode. In this figure the amplitude of oscillation is plotted as the change in the intensity δI normalized by the total intensity I versus the frequency of the applied force. The black triangles are the EWS measurements multiplied by 6, showing that SPR mode has $6times$ larger sensitivity.

2.6 Mechanical Response Measurements

The molecule under study is forced to oscillate at a certain frequency, by deriving GNPs attached to the molecules in an AC electric field. The amplitude and phase of this oscillation is measured. Changing the frequency of the applied voltage, we obtain the frequency response of the molecule, which helps us estimate the mechanical properties of the molecule. A microscope with a $\times 60$ magnification is used to focus on the desired area and collect the light. As discussed earlier in this chapter, the light scattered from the GNPs is then collected by a photomultiplier tube (Hamamatsu H10721-110) which, running in current mode, converts the light signal to electronic signal. The current is then converted to voltage and sent back to the LIA through the input port to be measured in phase locked loop. The

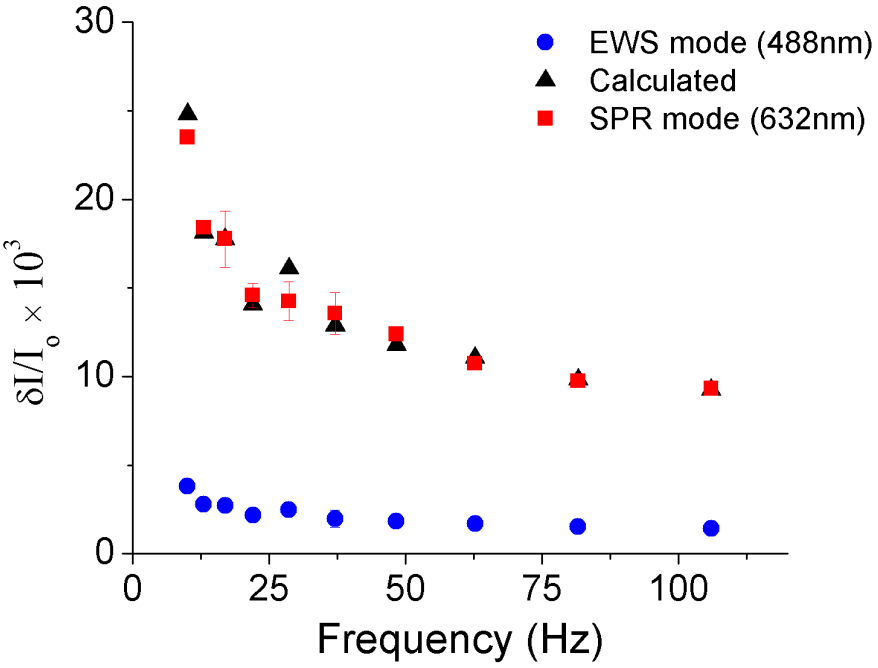

Figure 2.14: The amplitude of oscillations measured as the change in the intensity δI normalized by the total intensity I versus the frequency of the applied force. Blue circles are measurements in EWS mode and red squares are measurements in SPR mode. The black triangles are the EWS measurements multiplied by 6, showing that SPR mode has 6*times* larger sensitivity.

measurement, as discussed in section 2.3.1, provides us with the phase and amplitude of the signal. For each frequency (at fixed voltage) the signal was traced for 50 seconds at 256 Hz acquisition rates, resulting in $\sim$ 12800 data points, and the final values of amplitude and phase of the signal is the average of these 12800 data points at each frequency.
LIA is controlled by a computer through a PCI-GPIB board (from National Instrument). Because the impedance of the circuit varies by frequency, the actual voltage across the chamber is different from the voltage supplied by the lock-in, and the difference depends on the frequency of the applied voltage. Thus, the supplied voltage has to be adjusted as frequency changes. To do so the actual voltage across the cell is measured by a 68-pin I/O connector (CB-68LPR from National Instrument) and read by the computer using the DAQmx data acquisition software from National Instrument. Then using a C++ program, the supplied voltage is adjusted at each frequency, according to the measured actual voltage across the chamber. Fig. 2.15 is a schematic representation of the measurement setup, which can be mapped on to Fig. 2.16 which shows the real experimental setup.

Before explaining the results, it is noteworthy to mention that all the measurements are ensemble averaged over many GNPs ($\sim 10^8$ particle in the field of view). Therefore thermal fluctuations and random noise due to stochastic motion of GNPs are canceled out. These are independent motions that decrease by $1/\sqrt{N} \sim 10^{-4}$ when averaged over N particles (FPP07).
The nm size thermal motion of each GNP adds incoherently to the scattered intensity and so averages to zero, while the collective oscillation driven by the electric field adds coherently, and can be measured with sub-$\mathring{A}$ resolution. The nano-rheology setup is essentially an ensemble of $\sim 10^8$ synchronous nanoscale rheometers with ensemble averaged readout.

2.6.1 Viscoelastic Response: Maxwell Model

In this section, the AC mechanical deformations of the enzyme Guanylate Kinase, measured with the method discussed earlier in this chapter, is presented. Fig. 2.17 shows the measured

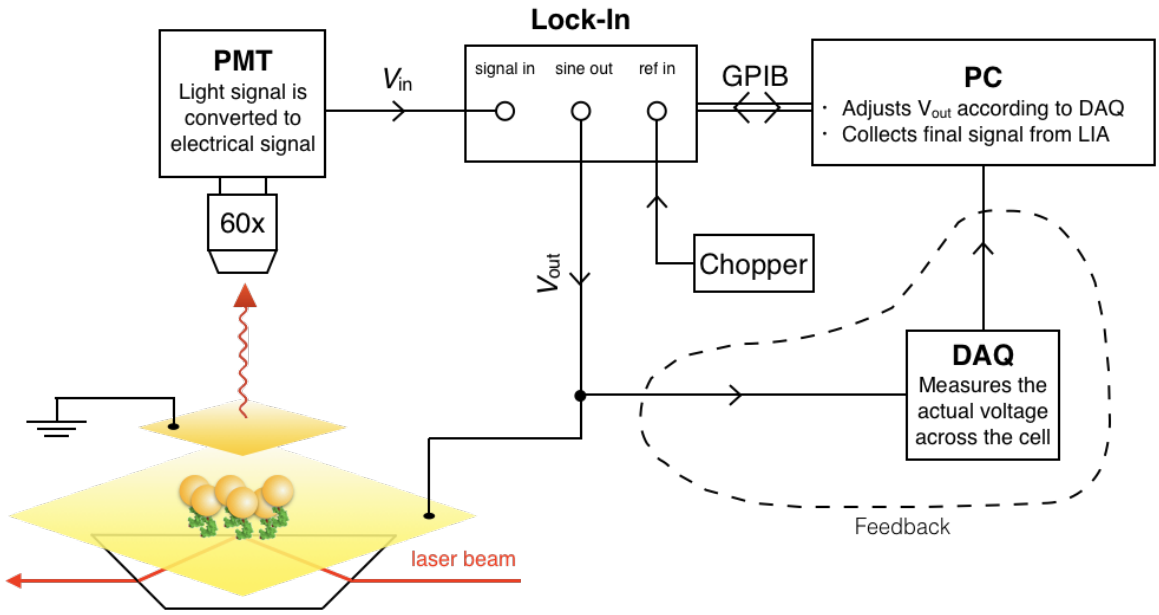

Figure 2.15: Schematic representation of the measurement setup. A computer communicates with LIA through a GPIB module. The computer orders LIA to generate an AC signal with a specific voltage and frequency. Using a feedback loop the voltage is adjusted according to the actual voltage across the cell measured with DAQ. The light scattered by GNPs is collected with a microscope and converted to electrical signal using a photo-multiplier tube. The produced signal is then sent to LIA to be measured and then sent to the computer to be represented and stored.

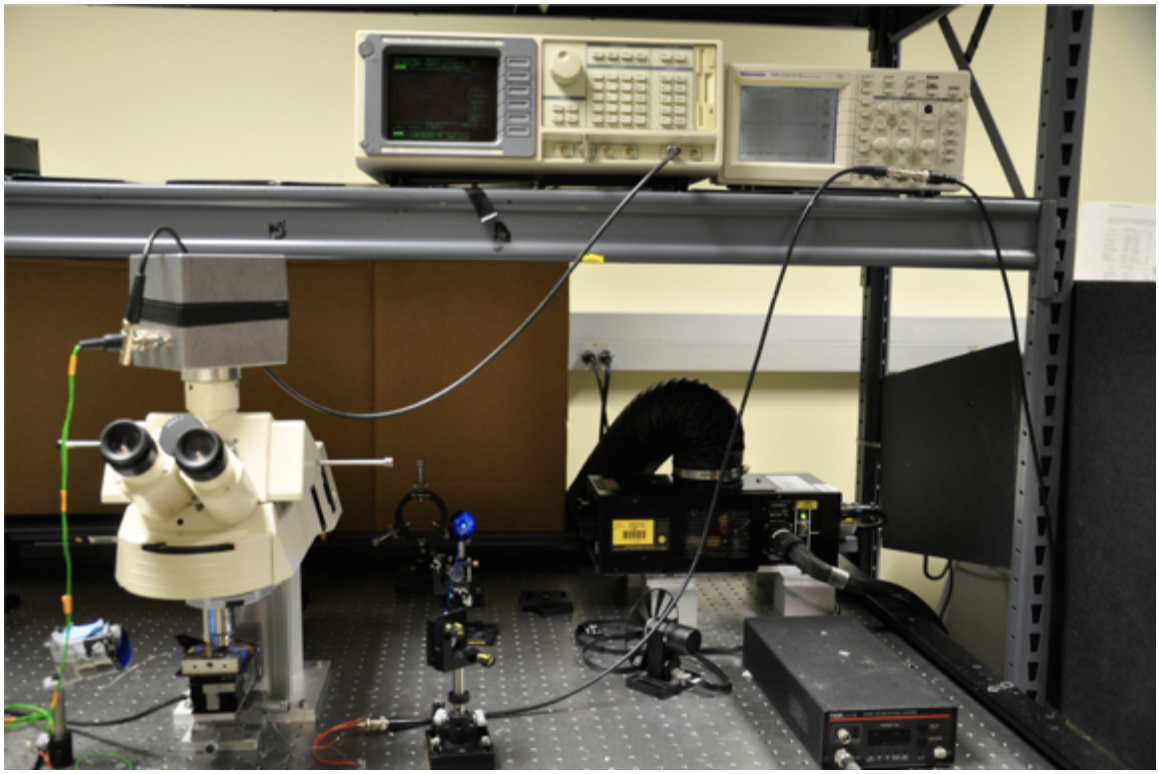

Figure 2.16: Picture of the real experimental setup.

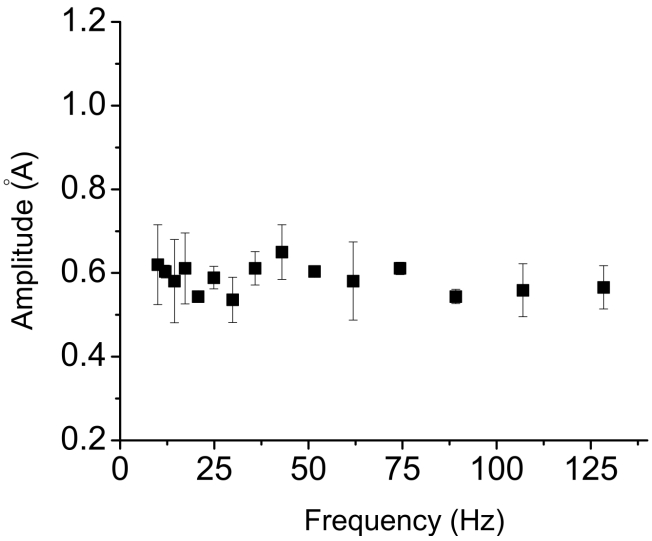

Figure 2.17: Mechanical response function measured for Guanylate Kinase using nano-rheology setup. The amplitude of response is plotted versus frequency of the applied force, at a constant voltage of $V_0 = 125$ mV. For this voltage, the amplitude of response remains constant as frequency changes.)

amplitude of response versus frequency of the applied force, at a fixed low voltage of 125 mV. As this figure suggests, the amplitude does not change with frequency. This graph is adapted from Dr. Amila Ariyaratne's PhD Dissertation titled "Rheology of biological macromolecules".

However at a higher voltage, the situation is different. Fig. 2.18 shows the same quantity measured at 250 mV. Here the frequency dependence is very clear: at lower frequencies the amplitude decays as $1/\omega$ whereas at higher frequencies a plateau is reached. If now we go back to 125 mV we can reproduce Fig. 2.17, which means that this behavior is reversible.

Assuming that the deriving force is $F = F_0\ e^{i\omega t}$, the amplitude of response is expected to be independent of frequency for elastic materials. At low voltages, according to Fig. 2.17, the enzyme behaves elastically, $|z| \propto F_0/k$ (k being the spring constant) for all frequencies. However Fig. 2.18 suggests that at higher applied voltages, the enzyme behaves elastically only at high frequencies. In this case, the enzyme shows a viscous behavior at low frequencies.

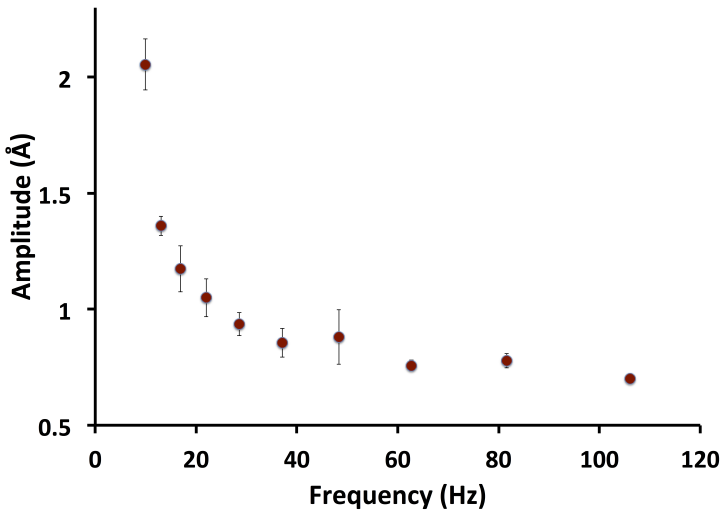

Figure 2.18: Mechanical response function measured for Guanylate Kinase using nano-rheology setup. The amplitude of response is plotted versus frequency of the applied force, at a constant voltage of $V_0 = 250$ mV. For this voltage, amplitude of response clearly depends on the frequency of the applied force. At lower frequencies the amplitude scales by $1/\omega$ whereas at higher frequencies it remains constant.

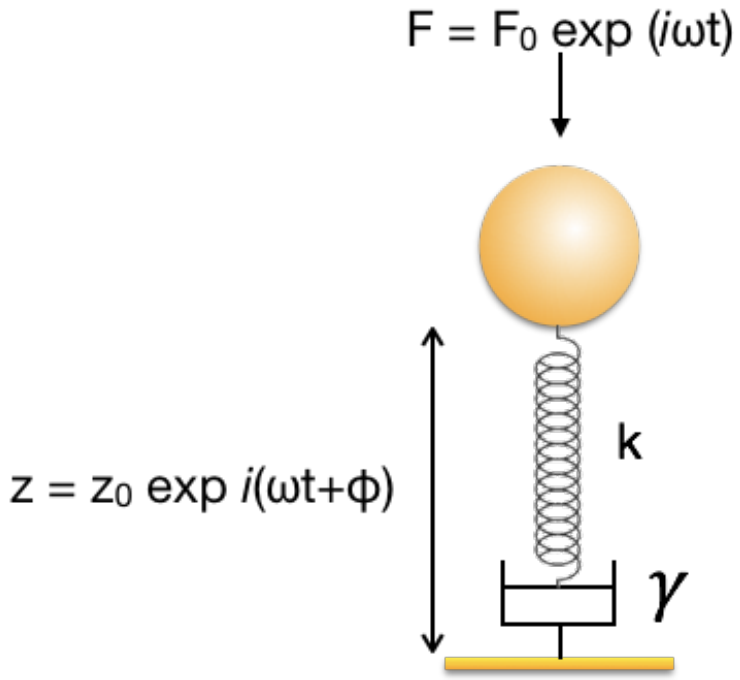

Figure 2.19: Schematic representation of Maxwell model configuration. A spring with spring constant k is in series with a dashpot with viscosity constant γ. The frequency response function of this configuration can be explained by Eq. 2.44.

If we assume a viscosity constant γ for the enzyme, we have

$$\dot{z} = \frac{F}{\gamma} \Rightarrow z \propto \frac{1}{\omega} e^{i(\omega t+\phi)} \tag{2.41}$$

So at high enough voltages, the enzyme goes from having a dissipative behavior at low frequencies to being an elastic material at high frequencies. This changing behavior can be modeled as an elastic component in series with a viscous component (WZ10; WZ11a; WZ11b). This model, called the Maxwell model, was first proposed by James Clerk Maxwell in 1867. Fig. 2.19 shows the configuration.

For this model we can write

$$z = z_s + z_d, \quad z_s = \frac{F}{k}, \quad \dot{z}_d = \frac{F}{\gamma} \tag{2.42}$$

where is z_s is the displacement of the spring (elastic component) and z_d is the displacement of dashpot (viscous component).

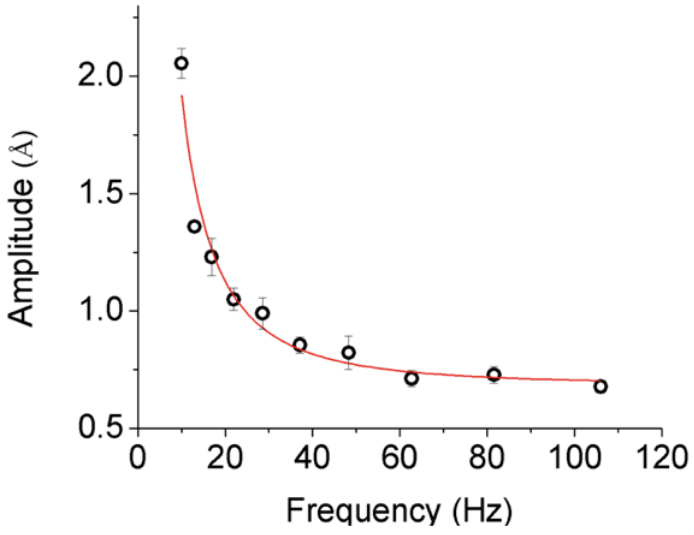

Figure 2.20: The same results shown in Fig. 2.18 is fitted with Eq. 2.44, resulting in a corner frequency of $\sim$ 20 Hz.

Therefore the equation of motion becomes

$$\dot{z} = \frac{\dot{F}}{k} + \frac{F}{\gamma} \tag{2.43}$$

Putting $F = F_0\ e^{i\omega t}$ and $z(\omega) = z_0(\omega)e^{i(\omega t+\phi)}$ in Eq. 2.43 we obtain

$$\begin{aligned} |z_0| &= \frac{A}{\omega}\sqrt{1+\left(\frac{\omega}{\omega_c}\right)^2} \\ \phi &= tan^{-1}\ \frac{\omega_c}{\omega} \end{aligned} \tag{2.44}$$

where $A = \frac{F_0}{k}$ and $\omega_c = \frac{k}{\gamma}$. In this equation

$$\lim_{\omega\to 0} z_0(\omega) \simeq \frac{1}{\omega} \quad \text{and} \lim_{\omega\to\infty} z_0(\omega) \simeq \frac{F_0}{k}\ \text{(constant)} \tag{2.45}$$

which is valid for the results shown in Fig. 2.18. Fitting the experimental results with Eq. 2.44, as seen in Fig. 2.20, the cut-off frequency ω_c was found to be $\sim$ 20 Hz. This is the frequency beyond which the enzyme starts to become elastic.

Elastic constant k thas previously been determined by previous experiments using the DNA spring (TWZ09). Taking k = 5 pN/nm and $\omega_c = 20\times 2\pi$ rad/sec, we can estimate the

internal friction coefficient, γ, to be $\simeq 4 \times 10^{-5}$ kg/sec.

Notice that in Eq. 2.42 and 2.43 there was no $m\ddot{z}$ term. This is because, as discussed earlier in section 2.2.4, the Reynolds number of the system is very small and thus the inertial effect is negligible. Also the viscosity of GNP against the solvent is negligible compared to that of the protein, meaning $\gamma \gg \gamma_0$ ($\sim 10^5$ times) (RFC94; KBB06). If we were to consider the friction of GNPs against the solvent, we would have a second cut-off frequency at kHz range, beyond which the dissipation of GNPs would have to be taken into account.

Maxwell model represents a linear system in which the amplitude of response depends on the magnitude of the applied force, but phase does not, as seen in Eq. 2.44. However our system shows nonlinearity. Fig.2.21 shows the frequency scan of the mechanical respond amplitude measured at different voltages (QLZ12). The lines are fits with Eq. 2.44. The value of A and ω_c is obtained for each voltage, using this fit. As seen in this figure, ω_c increases monotonically with V_0, amplitude of the applied voltage. The inset is a plot of $ln(\xi)$ versus $ln(1/\omega)$, where $\xi = |z|/(A\sqrt{1 + \left(\omega/\omega_c\right)^2})$, where A and ω_c are obtained by Eq. 2.44 for each voltage.

Keeping a constant frequency and measuring the response at different voltages, was seen that the viscoelastic transition is not linear, but sharp. Fig.2.22 (adapted from (QLZ12)) shows the applied voltage (which is proportional to the applied force F_0) versus the measured amplitude of the resulting deformation, at fixed frequency. A break at $\sim 1\mathring{A}$ is seen. This figure shows that the linear elasticity regime (where $|V_0| \propto |z_0|$) is extended at the higher frequency. This is consistent with the shift seen in $|z_0| - \omega$ plane where ω_c increases with V_0 (Fig. 2.21).

Fig.2.23 (adapted from (QLZ12)) is a plot of ω_c versus the applied voltage V_0. The relation $\omega_c = \omega_c(V_0)$ defines a viscoelastic phase transition in this diagram. In summary Maxwell model is not enough to describe the nonlinearity seen in our system. The frequency dependence can be described by Eq. 2.44, but the force dependence ($\omega_c = \omega_c(V_0)$) cannot.

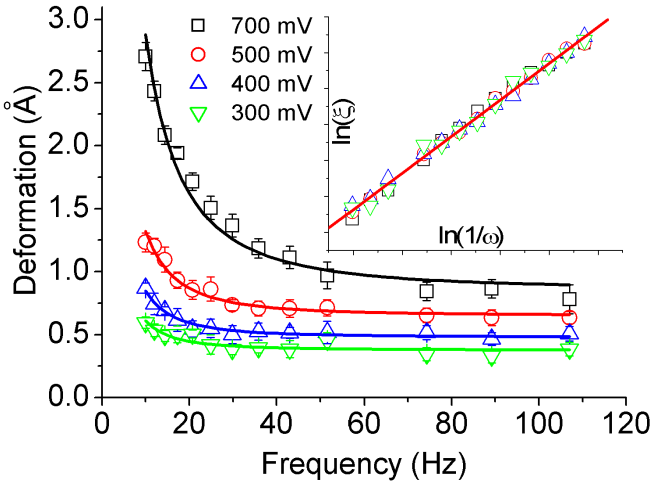

Figure 2.21: Mechanical response function measured for Guanylate Kinase using nano-rheology setup. The amplitude of response is plotted versus frequency of the applied force, at a constant voltage, for different values of V_0. The lines are fits with Eq. 2.44 to obtain ω_c for each voltage. ω_c increases monotonically with V_0. The inset is a plot of $ln(\xi)$ versus $ln(1/\omega)$, where $\xi = |z|/(A\sqrt{1+\left(\omega/\omega_c\right)^2})$ where A and ω_c are obtained by Eq. 2.44 for each voltage.

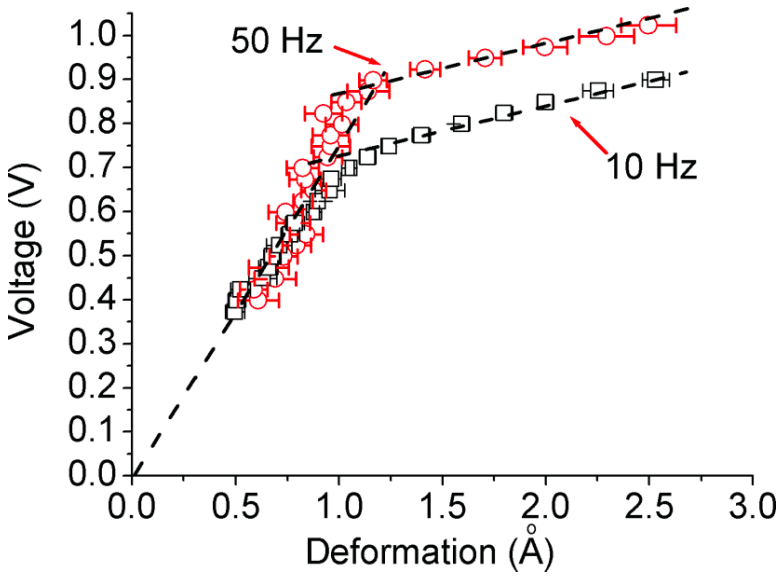

Figure 2.22: Mechanical response function measured for Guanylate Kinase using nano-rheology setup. Voltage of the applied force is plotted versus rms value of the amplitude of response, at fixed frequency. Different sets are for different frequencies. A sharp transition is observed as the enzyme goes from the elastic regime (towards smaller amplitudes) to the viscous regime (towards larger amplitudes). As frequency increases, the linear elasticity regime extends.

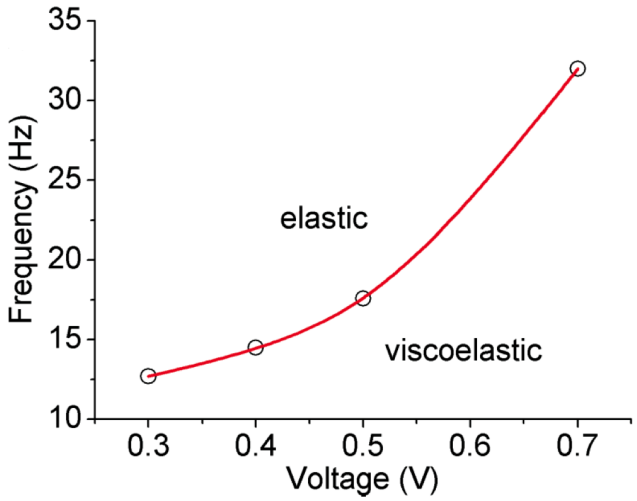

Figure 2.23: The phase diagram of the viscoelastic transition by plotting the cut-off frequency ω_c (obtained from Fig. 2.21) versus the magnitude of the applied force, V_0. The line separates the two regimes, i.e. the linear elastic dynamics from softer viscous dynamics.

CHAPTER 3

Probing the Surface: Hydration Layer Contribution

Monomeric enzymes are soft, heterogeneous nanoparticles with specific catalytic activity in aqueous environment. Functionally speaking, all the action is at the surface of the enzyme, which often deforms considerably upon binding of the reactants, into the catalytically competent conformation. These large deformations are driven primarily by surface forces, i.e. the interaction between the substrates and the surface of the enzyme: it is the enzyme's surface, not the interior, which is "complementary" to the reactants. Because of the enzyme's small size ($\sim 4\,nm$) the surface contribution to the dynamics is not overwhelmed by the bulk contribution. The surface of the enzyme is a complex dynamic network of hydrogen bonds between and amongst water molecules in the hydration shell of the protein and residues at the enzyme's surface. Fig. 3.1 shows the concept.

Here I show, through direct mechanical measurements, that this interface partially controls the mechanics of the enzyme, at least for the specific enzyme of this study. The hydration shell is chemically modified by addition of DMSO - a kosmotropic (order inducing) agent - in concentrations so small that the bulk properties of the solvent (water) are unaffected. Yet a dramatic effect on the mechanical susceptibility of the enzyme is observed, measured through a nano-rheology method (see Chapter 2). Interpreted through the viscoelastic model of enzyme conformational dynamics introduced in section 2.6.1, these measurements show that the enzyme's surface (the enzyme - water interface) partially controls the dissipative part of the dynamics.

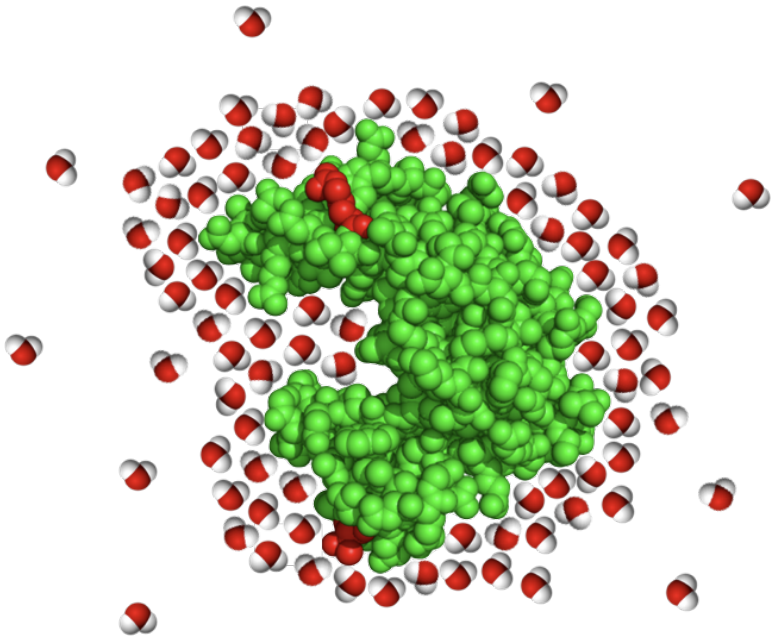

Figure 3.1: The surface of the enzyme is a complex dynamic network of hydrogen bonds between and amongst water molecules in the hydration shell of the protein and residues at the enzyme's surface. This hydration shell is an integral part of the enzyme which cannot be dissociated from it. Without the hydration layer there will be no functionality.

3.1 Perturbation of the Hydration Layer

The method is based on measuring the mechanical response function of the molecules in the frequency domain. The enzyme under study tethers gold nanoparticles (GNPs) to a microscope slide coated with a thin gold layer which allows optical measurements. The negatively charged GNPs are driven by an AC electric field perpendicular to the gold surface, and the amplitude of their motion in the same direction is measured by evanescent wave scattering, using a phase locked loop. With this method, the native conformation of the enzyme is preserved, as demonstrated by the ability of the enzyme in the apparatus to still bind specifically its substrates (WZ10). All details are explained in Chapter 2.

To study the contribution of the surface (i.e. the hydration layer) of the enzyme in the viscoelastic behavior seen in section 2.6.1, the surface was perturbed by adding small amounts of a chemical compound: dimethyl sulfoxide. DMSO (dimethyl sulfoxide: $(CH_3)_2SO$) is a polar organic solvent and cryoprotectant used when freezing cells; one notable property is that it readily penetrates the skin. In the biomolecular context, its interesting property is that it hydrogen bonds with water, the water - DMSO bond being somewhat stronger than the water - water bond (LC93). Furthermore, the presence of DMSO strengthens the water -water bond (LC93). It is a "kosmotropic" agent, believed to increase the ordering of water molecules in the first hydration shell of water dissolved substances (Rus08; VB92). Fig. 3.2 shows the molecular structure of DMSO.

An important property for the present study is that DMSO affects the dynamics of the hydration layer even at bulk concentrations ($0.1 \sim 1\,\%$, or $14 \sim 140\,mM$) which are too small to affect the properties of the bulk solvent. Presumably, DMSO accumulates into ("binds to") the hydration shell.

Also to show that DMSO at these concentrations does not affect the force on GNPs, a control experiment was conducted. In this experiment we studied the frequency response of a single stranded DNA with and without DMSO. The configuration for this experiment is shown in Fig. 3.3.

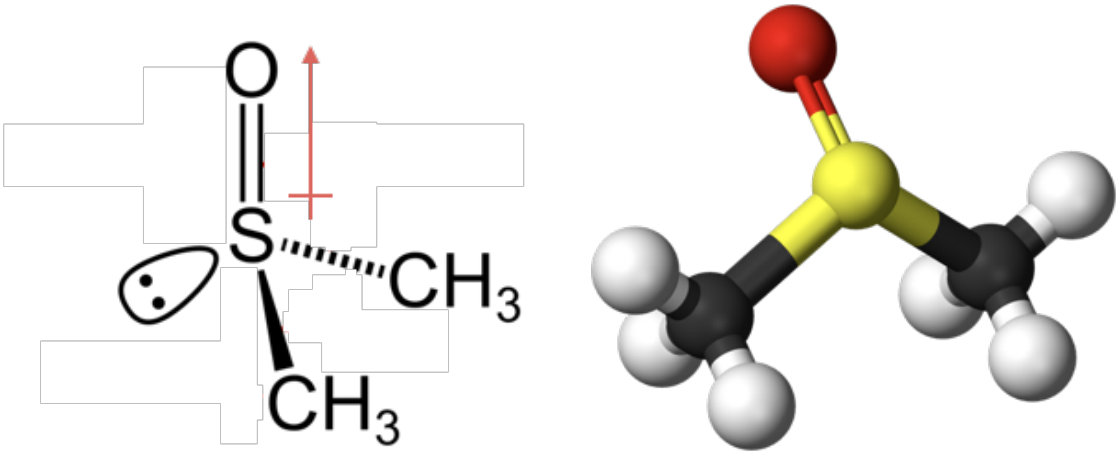

Figure 3.2: Molecular structure of dimethyl sulfoxide (DMSO) with the formula: $(CH_3)_2SO$. DMSO is a polar molecule with a molar mass of 78.13 g/mol. It is only an acceptor for hydrogen bonds and can bind to two water molecules.

DNA Arm B was initially tethered to the gold-coated slide employing using a similar method as the one used for tethering GK. DNA Then, Arm A was separately hybridized to the gold nano particles using the method described in (TMH02). DNA Arm A has a 12 base pair region at the end that is complementary to the end of Arm B. Thus, adding GNPs modified with DNA Arm A onto the Arm B, which is tethered to the gold slide, results in the tethering of the GNPs on to the gold coated slide.
Single stranded DNA is a polymer coil that behaves as an entropic spring. Therefore its response to an oscillatory force should be flat and independent from the frequency of the applied force.

Applying 300mV voltage across the cell, the response of the tethered ss DNA was measured, first without and then with DMSO. Fig. 3.4 shows the result. The squares are the measurements obtained in standard condition and the circles are measurements obtained in the presence of 1% DMSO.

This graph shows that DMSO does not affect the mechanics of DNA when used at small

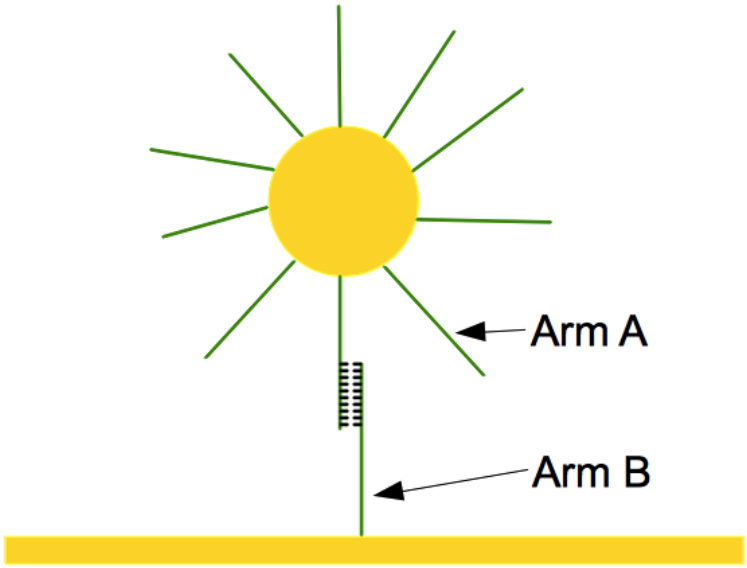

Figure 3.3: Gold nano particles tethered to the gold slide by ss DNA. First DNA Arm B is attached to the gold slide via thiol modification. GNPs are modified on the surface with DNA Arm A. DNA Arm A has a region at the end that is complimentary with the end region of DNA Arm B. Therefore when modified GNPs are introduced to the surface, they become tethered by these ss DNAs.

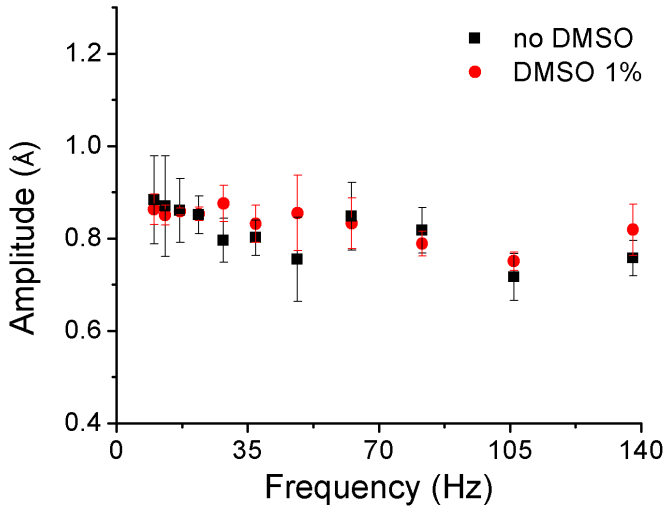

Figure 3.4: Frequency response of ss DNA obtained at 300mV. The response does not depend on the frequency as the ss DNA is similar to a spring. The squares are measurements done in the standard condition and the circles are measurements done in the presence of 1% DMSO. As seen in this graph, DMSO does not alter the response which means that it does not disrupt the force on the GNPs, since the two measurements are done on the same sample at the same voltage.

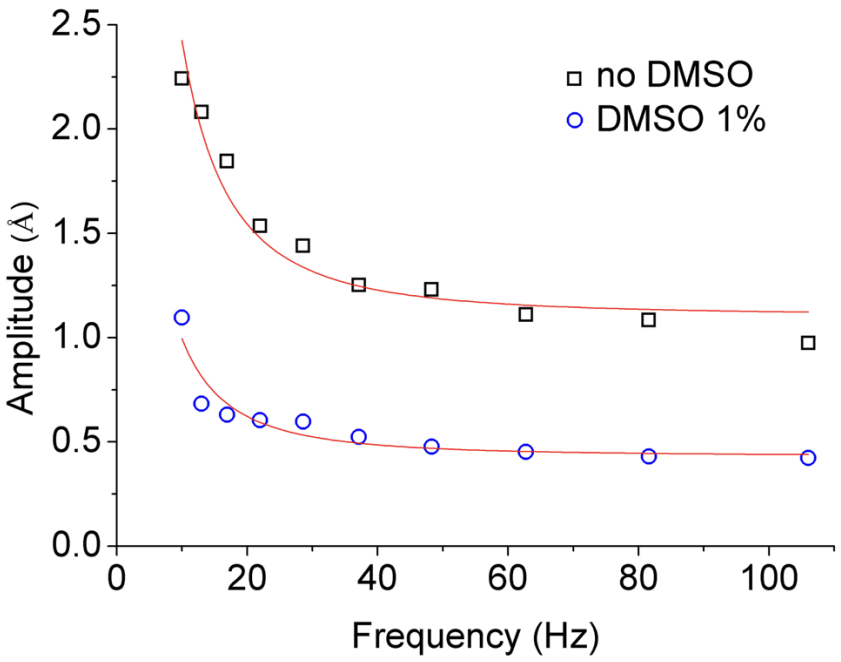

Figure 3.5: Response amplitude vs forcing frequency in the absence (squares) and presence (circles) of 1 % DMSO, for the same sample. Lines are fits with the viscoelastic response i.e. Eq. 3.1.

concentrations. Since the two responses in Fig. 3.4 are similar, it is concluded that DMSO does not alter the relation between the applied voltage and the force exerted on GNPs.

Now that we have shown adding DMSO does not alter the relation between the applied voltage and the force on the GNPs, we look at the effect of DMSO on GK.

The experiments are performed by first recording the frequency response of the system in the working buffer (which is SSC/3), in the range $10 \sim 200\,Hz$, using a fixed amplitude of the applied voltage such that the maximum amplitude of the response does not exceed $2 \sim 3\,\mathring{A}$ (in order not to damage the sample). Then the buffer in the cell is exchanged with the same buffer containing a given concentration of DMSO, and a new frequency response is recorded, all other conditions being exactly the same. Fig. 3.5a shows the dramatic effect of 1 % DMSO in solution on the measured mechanical response of the enzyme.

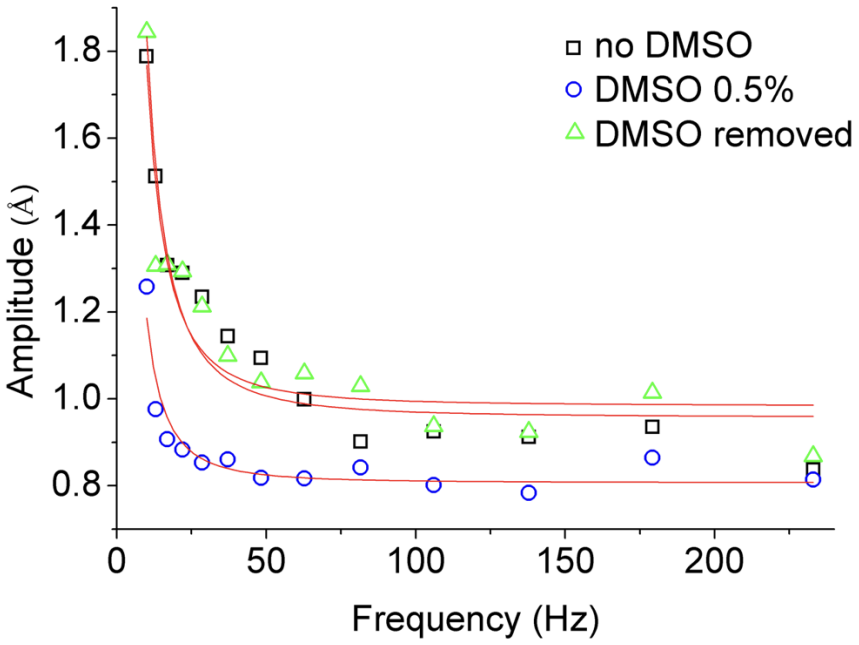

Figure 3.6: Reversibility of the DMSO induced change in mechanical properties. The figure shows, for the same sample, the response amplitude vs frequency before adding DMSO (squares), after adding 0.5 % DMSO (circles), and after removing DMSO (triangles). For both graphs each point is an average of 4-5 measurements. Typical standard deviation is $\sim 0.1\,\mathring{A}$.

Without DMSO, we observe the viscoelastic response (elastic at high frequency, viscous at low frequency) which we have described before for this enzyme (WZ11a; QLZ12; QZ13). Namely, there is a high frequency plateau in the amplitude curves (the response of a spring), and a $1/\omega$ divergence at low frequency (the response of a viscous flow). Adding DMSO makes the enzyme a factor ~ 2 "stiffer". The enzyme is still in its native, functional state (as I demonstrate later) and these mechanical susceptibility curves are reversible. The reversibility is shown in Fig. 3.6, where the frequency response in the absence of DMSO (squares) was recorded, then DMSO 0.5 % was added and the response was measured again (circles), then the DMSO is washed away and measurements are repeated once more (triangles).

At fixed amplitude of the forcing, our frequency response curves are very well described by the Maxwell model of viscoelasticity introduced in section 2.6.1, where the (one - dimen-

sional) mechanics is summarized by an elastic parameter κ (dimensions of $force/length$) and a dissipation parameter γ (dimensions of $mass/time$). In the context of this experiment, the corresponding deformation amplitude ($|z|$) vs frequency (ω) curve takes the form:

$$|z| = \frac{F_0}{\gamma\omega}\sqrt{1+(\omega/\omega_c)^2} \tag{3.1}$$

where $\omega_c = \kappa/\gamma$ is the corner frequency below which the response changes from elastic to viscous; F_0 is the amplitude of the applied force. The lines in Fig. 3.5 and 3.6 are two - parameter fits using Eq. 3.1, or more precisely using the form $|z| = (A/\omega)\sqrt{1+(\omega/B)^2}$. For each sample, I determine the parameters A and B and because F_0 is the same for the same sample we find the relative change in the parameters κ, γ of the viscoelastic description induced by the presence of DMSO. Namely, $\gamma \propto 1/A$, $\kappa \propto B/A$. The result for the change in the viscous dissipation γ is plotted vs log of bulk DMSO concentration in Fig. 3.7. For increasing DMSO concentration in the window $0.05 \sim 5\,\%$ the internal dissipation parameter γ increases up to a factor 2. It is remarkable that even a DMSO concentration as small as $0.1\,\%$ ($\sim 14\,mM$) leads to a detectable effect in the mechanical response of the enzyme.

The determination of the change in elastic parameter κ from the fits of Fig. 3.5 is in contrast noisier and shown in Fig. 3.8. The reason is the poor determination of the corner frequency ω_c (the parameter B) for the high DMSO concentration data. From Fig. 3.8 we conclude that κ is either unaffected or increases slightly ($\sim 20\,\%$) in the presence of DMSO. The main effect is on the dissipation parameter γ.

In this interpretation, the dramatic mechanical effect shown in Fig. 3.5 reflects an enzyme which becomes not so much "stiffer" as "more viscous" in the presence of DMSO.

The measurements of Fig. 3.7 are actually aligned on a binding isotherm (line in Fig. 3.7), i.e. they reflect the average occupation number for a two - states system:

$$\frac{\gamma-\gamma_0}{\gamma_0} = \frac{\alpha}{1+K_D/[DMSO]} \tag{3.2}$$

The LHS is the relative change in γ (γ_0 is the value in the absence of DMSO), $[DMSO]$ the DMSO concentration, K_D a "dissociation constant", and α a normalization factor. The

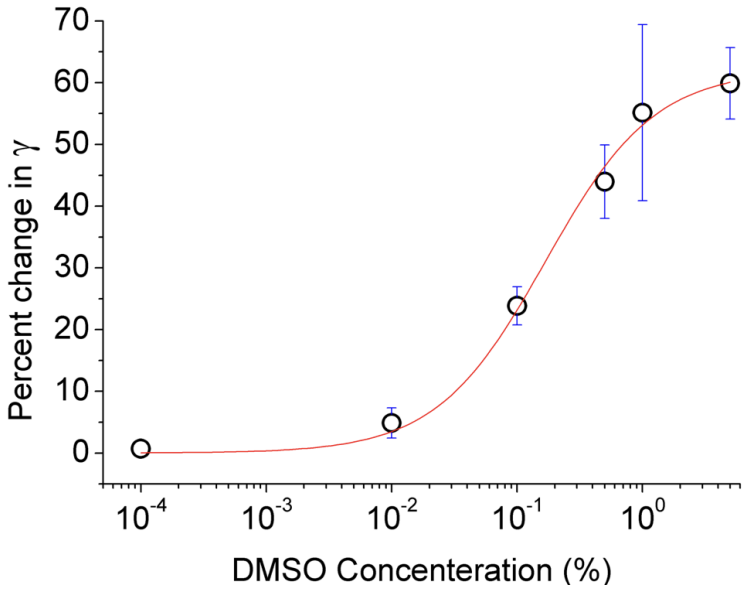

Figure 3.7: Percent change in the viscoelastic dissipation parameter γ (measured from fits as in Fig. 2) vs DMSO concentration. The line is a fit with Eq. 3.2 giving the values $K_D = 0.17$ % and $\alpha = 62$. Each point is an average of 5 measurements. The error bars indicate uncertainty($\sigma/\sqrt{N}$). Overall, the dissipation γ increases by $\sim 60\,\%$ in the presence of DMSO.

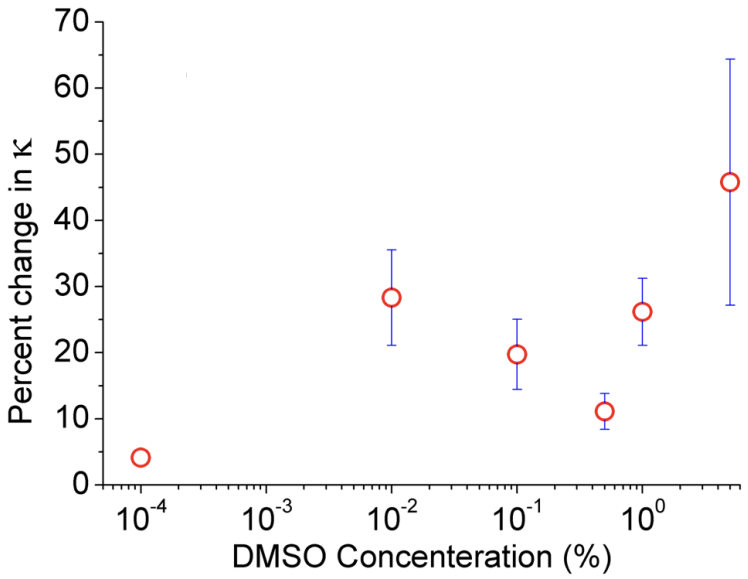

Figure 3.8: Percent change in the elasticity parameter κ. Given the large error bars, it is not clear whether κ is unaffected or increases slightly with DMSO.

value obtained from Fig. 3.7 is $K_D = 0.17\,\% = 24\,mM$.

The behavior displayed in Fig. 3.7 is instructive: it means DMSO accumulates at the surface of the enzyme by occupying a finite number of "binding sites", as shown schematically in Fig. 3.9.

This situation can be mapped to the problem of atoms of a dilute gas adsorbing on a surface, with N possible sites for adsorption. At equilibrium the fraction of occupied sites on the surface is:

$$\frac{< n >}{N} = \frac{1}{1 + K_D/C} \tag{3.3}$$

where $< n >$ is the average number of occupied sites, C the concentration (number of particles per unit volume); $K_D = \lambda^{-3} e^{\epsilon/T}$ with $\lambda = (h^2/(2\pi m T))^{1/2}$ the thermal wavelength and ϵ the binding energy to the surface. This is Eq. 3.2. On the other hand, the opposite scenario where DMSO binds to, but moves freely on, the 2D surface leads to a linear dependence on C, obtained by using, for the chemical potential of the molecules on the surface,

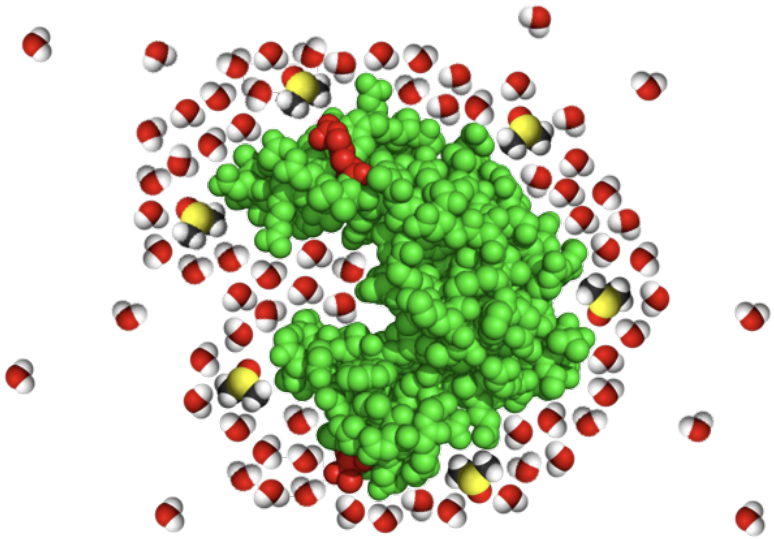

Figure 3.9: DMSO accumulates at the surface of the enzyme by replacing water molecules and occupying a finite number of binding sites.

the expression for the 2D ideal gas:

$$\mu_s = \epsilon + Tln(\lambda^2 n_s) \tag{3.4}$$

where n_s is the number of adsorbed atoms per unit area; this leads to the relation:

$$n_s = \lambda e^{-\epsilon/T} C \tag{3.5}$$

The measurements show that the first scenario (Eq. 3.3) is correct. Evidently more complicated explanations for the behavior of Fig. 3.7 are possible. For instance, the saturation may be due to a nonlinear relation between the parameter which is actually measured (γ) and n_s. Or it may be that the surface density n_s is large enough that interactions must be included in Eq. 3.4. However, Eq. 3.2 is the simplest representation for the measurements.

Overall, these measurements show that small ($< 1\,\%$) bulk concentrations of DMSO, which have negligible effect on the physico-chemical properties of bulk water, including the viscosity and dielectric constant, have nonetheless dramatic effects on the dynamics of the hydration layer of the enzyme, and ultimately on the enzyme's mechanics. DMSO

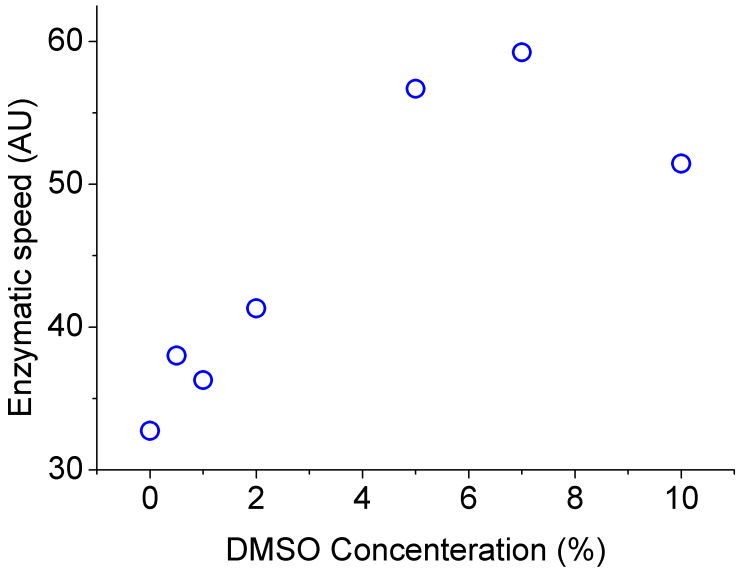

Figure 3.10: GK activity (speed of the reaction) for the free enzyme in solution vs DMSO concentration.

accumulates in the hydration layer ("binds to the surface of the enzyme"). Apparently the order - inducing ("kosmotropic") quality of DMSO leads to a hardening of the enzyme - water interface (SB12), detected in the measurements of Fig. 3.5.

I was of course curious to know what effect DMSO at these concentrations would have on the activity of the free enzyme in solution. In Fig. 3.10 the speed of the enzymatic reaction vs DMSO concentration is plotted, measured with a coupled enzymes biochemical assay (see section 5.4). The reaction catalyzed by GK is: $GMP + ATP \rightarrow GDP + ADP$ and we chose substrate concentrations ($2\,mM\,ATP$, $1\,mM\,GMP$) which maximize the speed, in an attempt to find a regime where enzyme conformational motion (rather than the chemical step) may be rate limiting. The result is surprising. The speed of the enzyme actually increases with DMSO present, though modestly (up to a factor 2). The speed increases linearly with DMSO concentration in the range $0 < [DMSO] < 5\,\%$, then saturates or perhaps decreases. However, for concentrations $[DMSO] < 1\,\%$ the reaction speed changes by at most $10\,\%$ (Fig. 3.10), whereas the dissipation γ increases by $\sim 70\,\%$ (Fig. 3.7). One possible conclusion is that the mechanics of conformational motion is not rate limiting for

this enzyme. Further, conformational motion and the chemical step seem to be essentially decoupled (changing γ, which affects the speed of conformational motion, does not change the overall enzymatic speed). This is a point of some contention as a general statement (AW09; MW06). However, in view of the fact that DMSO does eventually (at higher concentrations) increase the overall enzymatic speed (Fig. 3.10), it is also possible that the mechanics and the chemical step seem decoupled because of two compensating effects. This question provides motivation for further studies to detail the effects of DMSO on the specific steps of the enzymatic cycle (substrate binding, chemical conversion, product release). Having the possibility of both influencing and directly measuring the mechanical properties of enzymes, future experiments may clarify the question of whether large-scale conformational motion is in fact coupled to the chemical step or not.

The main result here is that influencing the hydration layer (while preserving enzyme structure and function) has a dramatic effect on the mechanical response of the enzyme. This fact may be surprising to some and obvious to others - one school of thought maintains that protein dynamics is "slaved" to the hydration layer (al05). Whether we are probing a global or local property of the enzyme - water interface is not clear: exquisitely detailed measurements of hydration dynamics by Overhauser dynamic nuclear polarization (ODNP) have shown that the hydration layer is significantly inhomogeneous, reflecting the inhomogeneous surface of the protein (al11). Water dynamics is slowed down in the hydration layer compared to the bulk, to an extent which is controlled by the protein's surface rather than the bulk solvent properties (FSH13). In light of results presented here, it is not surprising that DMSO displays a plethora of biological effects on the living cell: for example, the rheology of the hydration layer is likely to generally affect rates of macromolecular association and dissociation where large surfaces of molecular contact are involved. The dynamics of ion channels, motor proteins, and generally enzymes which display large conformational motion may be similarly affected.

3.2 Phase Measurements: Looking at Angstrom-scale Dissipation

In this section I introduce measurements of the phase of the mechanical response function within the nano-rheology paradigm. These measurements were possible because of the SPR enhancement introduced in section 2.5. I will show driven conformational motion of the enzyme is dissipative as characterized by the phase measurements. A viscoelastic transition seen in section 2.6 implies dissipative dynamics (AWT14; FRJ15); interpreting the corner frequency ω_c as a ratio of an elastic and a dissipative parameter: $\omega_c = \kappa/\gamma$ one finds indeed that the enzyme is effectively very viscous (WZ11a).

For the first time with this instrument, the measurement of the phase φ (between applied force and resulting deformation) were obtained, which is a direct measure of dissipation. Namely, for a linear system, an applied force $F(t) = F_0\, cos(\omega t)$ would result in a deformation $z(t) = z_0\, cos(\omega t + \varphi)$; the work done by the force over one cycle, which is the dissipation, is

$$\begin{aligned} W = \int_0^{2\pi/\omega} F\dot{z}\, dt \;&=\; -\int_0^{2\pi/\omega} dt\, F_0 z_0 \omega cos(\omega t) sin(\omega t + \varphi) \\ &=\; \pi F_0 z_0 sin(-\varphi) \end{aligned} \tag{3.6}$$

where φ is (see section 2.6.1):

$$\varphi = -atan(\omega_c/\omega) \tag{3.7}$$

For a nonlinear response, defining the dissipation is more delicate, but it is still true that $\varphi = 0$ corresponds to completely non-dissipative, and $\varphi = -\pi/2$ to completely dissipative, behavior, as explained for example in (FRJ15). In the general nonlinear case, the phase φ is defined by multiplying the signal by synchronous sines and cosines, averaging, and taking

the ratio:

$$z_r = \int_0^{2\pi/\omega} dt\, z(t) cos(\omega t) \quad , \quad z_i = \int_0^{2\pi/\omega} dt\, z(t) sin(\omega t)$$
$$tan(\varphi) = z_i / z_r \tag{3.8}$$

In our nano-rheology setup, the light intensity from the scattering setup is modulated at the forcing frequency, reflecting the synchronous oscillation of the GNPs; this signal, acquired with a photomultiplier, is combined with the reference forcing signal by a lock-in amplifier (Fig. 2.15), which performs the operations (Eq. 3.8), yielding the real and imaginary parts of the response, z_r and z_i, from which the amplitude $z = \sqrt{z_r^2 + z_i^2}$ and phase $\varphi = arctan(z_i/z_r)$ are calculated.

We will see that, similar to macroscopic rheology, for this molecular system also the measurement of the phase offers a consistent physical characterization, of the visco-elastic dynamics on the one hand, and also of perturbations applied to the system.

The work done by the force F over one cycle, which is the energy dissipated over one cycle, is

$$W = \int_0^{2\pi/\omega} F\dot{z}\, dt = \int_0^{2\pi/\omega} dt\, \frac{F_0^2}{\gamma} cos^2(\omega t) = \frac{\pi F_0^2}{\omega\gamma} \tag{3.9}$$

the same as for a pure flow, since this is a linear model. This work can be written in terms of different combinations of the thermodynamic variables $F_0, z_0, \varphi, \omega$; for example:

$$W = \pi F_0 z_0\, sin(-\varphi) \tag{3.10}$$

which is valid for any linear response function, not just the Maxwell model. But also,

$$W = \pi\gamma\, \frac{z_0^2\omega}{1 + (\omega/\omega_c)^2} = \frac{\pi}{2}\kappa z_0^2\, sin(-2\varphi) \tag{3.11}$$

These forms are specific to the Maxwell model; they show that, *at fixed* z_0, the dissipation is maximum for $\omega = \omega_c$ (and $\varphi = -\pi/4$).

We now examine the measurements. Fig. 3.11 shows a representative example of frequency scan for the GK with and without DMSO.

Let us first concentrate on the circles. In (a) we have the amplitude of the deformation, z_0. It shows the visco-elastic response documented before (WZ11a; QLZ12): $z_0 \sim const$ (independent of ω) above a corner frequency ω_c, and $z_0 \sim 1/\omega$ below ω_c. The line is a fit with the form for z_0 given in Eq. 3.1, returning the value $\omega_c = 163\, rad/s$ (note that the experimental data are plotted as a function of frequency $\nu = \omega/2\pi$ in $cycles/s$). In (b) we have the phase φ , for the same measurements. Qualitatively, it confirms that the dynamics is visco-elastic: non-dissipative for $\omega >> \omega_c$ (φ approaches zero), dissipative for $\omega << \omega_c$ (φ approaches $-\pi/2$). The line is a fit with the Maxwell model prediction in Eq. 3.7, returning the value $\omega_c = 213\, rad/sec$. The discrepancy between the values of ω_c obtained from (a) and (b), which is systematic, indicates that the Maxwell model describes the measurements only partially. Discrepancies are more evident in the phase plots, because the corresponding fits are one parameter fits. In (c) we replot the same data, but plotting the quantity $\pi z_0\, sin(-\varphi)$ vs ω. For any linear response system, including the Maxwell model, this quantity is equal to W/F_0 , see Eq. 3.10. In the Maxwell model, this same quantity is proportional to $1/\omega$, because from Eq. 3.9:

$$\pi z_0\, sin(-\varphi) = \frac{W}{F_0} = \frac{\pi F_0}{\gamma}\frac{1}{\omega} \tag{3.12}$$

The line in (c) is a fit using the form of the RHS of Eq. 3.12, returning the value $(\pi F_0/\gamma) = 67\, \mathring{A}\, rad/s$. We see that there is internal consistency between the measurements of the amplitude z_0 and the phase φ, and that both quantities roughly follow the frequency dependence of the Maxwell model of visco-elasticity. We therefore feel justified in interpreting the measured quantity $\pi z_0\, sin(-\varphi)$, for fixed F_0 , as a measure of the dissipation according to Eq. 3.10. Fig. 3.11c then shows that, at constant F_0 , the system is dissipative at low frequency and non dissipative at high frequency. This is, of course, completely different from a damped spring, which is non dissipative at low frequency.

Let us now discuss the data plotted as squares in Fig. 3.11. They represent the same

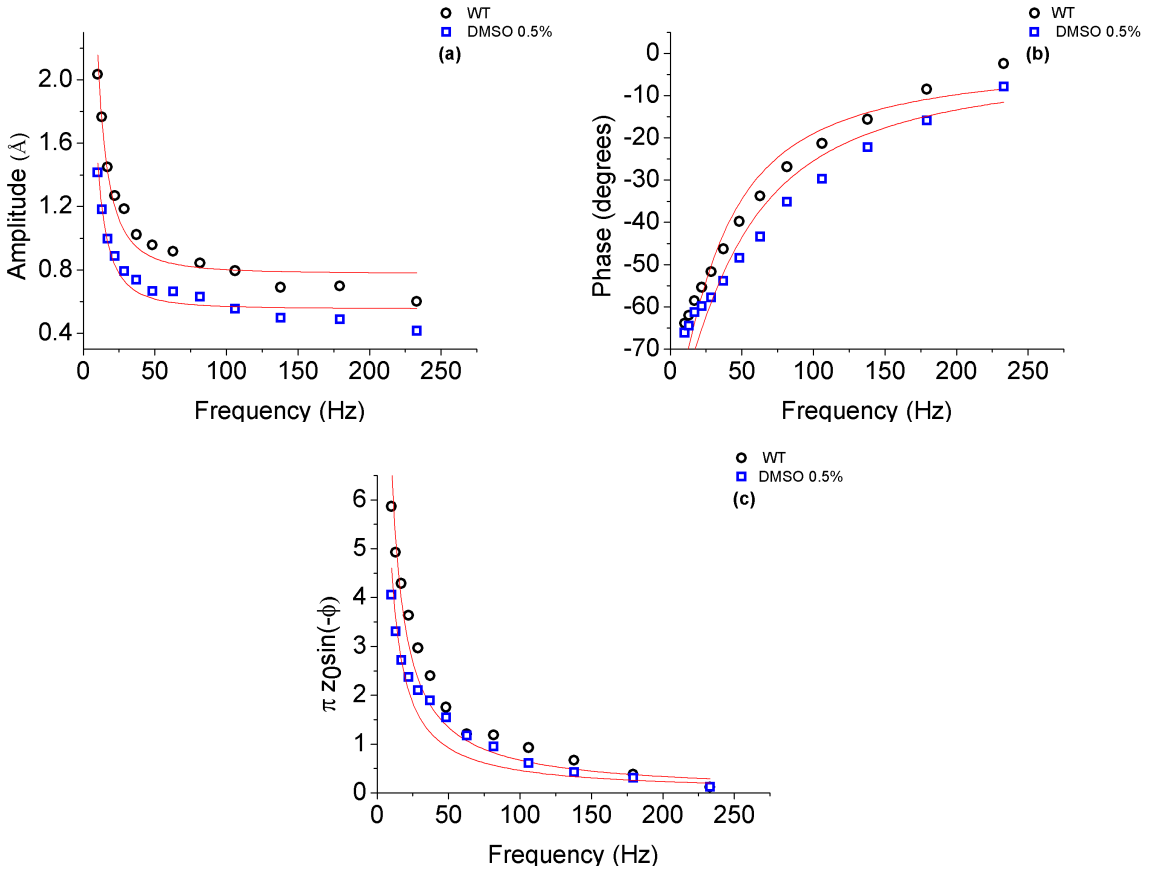

Figure 3.11: Frequency scan showing the mechanical response of the wild type (WT), under our standard conditions (in SSC/3, $50\,mM$ total ionic strength, $pH = 7.0$; circles) and with the addition of $0.5\,\%$ DMSO (a kosmotropic agent affecting the hydration layer; squares). The data are obtained from the same sample. (a) RMS amplitude z_0 of the response (in $\mathring{A}$) vs frequency $\nu = \omega/2\pi$ (in $cycles/s$). The lines are fits with Eq. 3.1, returning the values $F_0/\gamma = 20\,\mathring{A}/s$, $\omega_c = 163\,rad/s$ (circles) and $F_0/\gamma = 14\,\mathring{A}/s$, $\omega_c = 153\,rad/s$ (squares). (b) Phase φ of the response (defined operationally in Eq. 3.8) vs frequency. The lines are one-parameter fits with Eq. 3.7 , and show that the Maxwell model does not quite describe the system. (c) This plot is a measure of dissipation. For the same data (a) and (b), the quantity $\pi z_0 sin(-\varphi)$ is plotted (in $\mathring{A}$) vs frequency. For a linear system this quantity would be equal to W/F_0 (Eq. 3.10), where W is the energy dissipated per cycle and F_0 is the amplitude of the applied force. For the Maxwell model, this quantity is proportional to $1/\omega$ (Eq. 3.9); the lines are one-parameter fits with the form $const./\omega$.

sample as the circles, where DMSO (Dimethyl sulfoxide) 0.5 % (70 mM) has been added to the buffer. Earlier in this chapter it was shown that DMSO makes the enzyme more viscous by increasing the dissipation coefficient γ. The squares in Fig. 3.11a confirm that conclusion: for the same applied force, the presence of 0.5 % DMSO causes the deformation amplitude to drop by a factor 0.7 . The new measurements of the phase (Fig. 3.11b) show that the effect can be thought of as making the system more viscous: the phase decreases as DMSO is added at constant force. Fig. 3.11c shows that, in terms of the dissipation parameter γ of the Maxwell model, the dissipation measurements roughly agree with the amplitude measurements in finding an increase in γ by a factor 1.46 with DMSO present. Namely, interpreting the prefactor in the $1/\omega$ fits according to Eq. 3.12, we find $\pi F_0/\gamma = 67\,\mathring{A}\,rad/s$ for the circles, and $\pi F_0/\gamma_{DMSO} = 46\,\mathring{A}\,rad/s$ for the squares, giving $\gamma_{DMSO}/\gamma = 1.46$. In conclusion, by extending the measurements of the amplitude, which was reported previously, to measuring also the phase of the response function, we have shown that nano-rheology enjoys the same features as a macroscopic rheology experiment, where one measures amplitude and phase, or equivalently, real and imaginary part of the response function. The phase measurements were facilitated by the increase in sensitivity of the method obtained by making use of the plasmon resonance of the gold strip and gold nanoparticles in the detection optics (MHT12; AZ15).

3.3 Kosmotropic or Chaotropic?

Solvents in water can alter the hydrogen-bonding network between water molecules. Some solvents bring disorder and some make the water more ordered. The first group is called Chaotropic agents and the second is called Kosmotropic agents. These agents influence the stability of proteins in aqueous solutions (Rus08).

A chaotropic agent exerts chaotropic activity, i.e. causes entropic disordering. These agents weaken the hydrophobic effects in a macromolecule and disrupt the native states stability. In proteins, chaotropic agents reduce the amount of order in water molecules both in bulk

and the hydration shell and therefore disrupt the structure of the molecule, which can result in denaturing.

Kosmotropic agents, on the other hand, are order makers. They make water-water interactions more stable and contribute in to the stability.

Determining if an agent is kosmotropic or chaotropic is not straightforward. As seen earlier in this chapter, the effect of DMSO which is a kosmotropic agent, was detected with nano-rheology technique. In this section it will be shown that nano-rheology can be used to determine if an agents is order-maker or disorder-maker, by detecting its effect on the measure amplitude of response.

For this purpose, in addition to DMSO, two kosmotropic (Glucose and Trifluoroethanol) and two chaotropic agents (Urea and Guanidinium Chloride) were chosen to be studied.

Let us start with Urea. Urea is an organic compound with the formula $CO(NH_2)_2$. In concentrations up to 10 M, Urea can denature proteins by disrupting the non-covalent bonds and directly binding to amide units via hydrogen binds (QSK98). In this experiment the frequency response of the system in the working buffer (which is SSC/3), in the range $10 \sim 200\,Hz$, using a fixed amplitude of the applied voltage is first recorded. Then the buffer in the cell is exchanged with the same buffer containing a given 1M Urea (a low enough concentration in order to avoid denaturing. The enzyme is active in the presence of this amount of Urea as checked by NADH assay explained in section 5.4.), and a new frequency response is recorded, all other conditions being exactly the same. Fig.3.12 shows the result, as well as the molecular structure of Urea. In contrast to DMSO, the enzyme is softer (amplitude of oscillation shifts towards larger numbers) in the presence of Urea. This result confirms that Urea can be considered a chaotropic agent.

The next chaotropic agent is Guanidinium Chloride. Guanidinium Chloride is the hydrochloride salt of guanidine, with the chemical formula CH_6ClN_3. At concentrations above 6M, Guanidinium Chloride is one of the strongest denaturants. In this experiment, the effect of 0.5M Guanidinium Chloride is studied. This concentration is safe for the proteins struc-

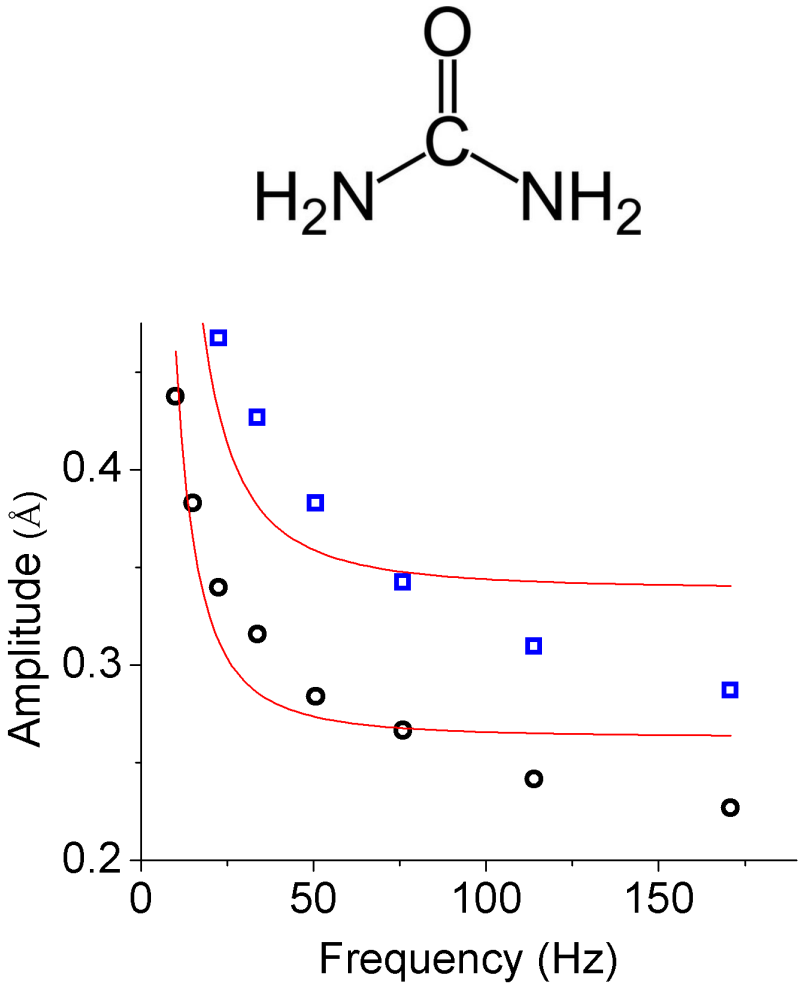

Figure 3.12: Moleculat structure of Urea and the effect of 1M Urea on the mechanical response of GK. The circles are measurements done in standard condition, and the squares are measurements done after 1M Urea was added to the buffer in the chamber. In contrast to DMSO, here the curve shifts upward. Fitting with Eq. 3.1, it is seen that γ (the dissipation coefficient) decreases by $\sim 50\%$.

ture, as the enzymatic activity was not changed much in the presence of 0.5M Guanidinium Chloride (checked with NADH assay explained in section 5.4. Fig. 3.13 shows the structure of this molecule and the result of the experiment.

The result confirms that Guanidinium Chloride is in fact chaotropic in a sense that it makes the enzyme more elastic, probably by making the water-water interactions less ordered, as it does not change the dissipation coefficient γ but does decrease κ , the elasticity coefficient. This result shows that Guanidinium Chloride might not disrupt the surface (which is associated with γ) and therefore it affects the protein in a different way than Urea (CRE08).

Now we look at a kosmotropic agent: Glucose with the chemical formula $C_6H_12O_6$. This simple sugar circulates in the blood as the blood sugar in animals. It has been shown in other studies that sugars enhance thermal stability of proteins(BOS79; HM13). Glucose is therefore known as a kosmotropic agent, which brings order to the structure. Similar to the procedures explained above, the effect of 0.5M Glucose was studied. Fig. 3.14 shows the structure of this molecule and the result of our measurements.

This result confirms the kosmotropic nature of Glucose. Similar to DMSO, Glucose makes the enzyme more viscous. As suggested in (HM13), being hydrophilic, Glucose bring structure to the protein-solvent interactions.

Finally we look at the effect of Trifluoroethanol (TFE) with the chemical formula $C_2H_3F_3O$. The effect of Trifluoroethanol on peptides has previously been studied and shown to make the peptide more structured (SEH92). TFE is often used to help the formation of peptides secondary structure (JCS07). This effect, however, depends on the concentration of TFE. Although low TFE concentrations can bring order, at higher concentrations TFE can act as a denaturant (RMF09; JCS07). At concentrations above a threshold of 16%v/v TFE disrupt the tertiary structure of BSA (Bovine Serum Albumin)(RMF09). Here we look at the effect of 10%v/v on the mechanical properties of GK, by following the same procedure as explained above for other agent..

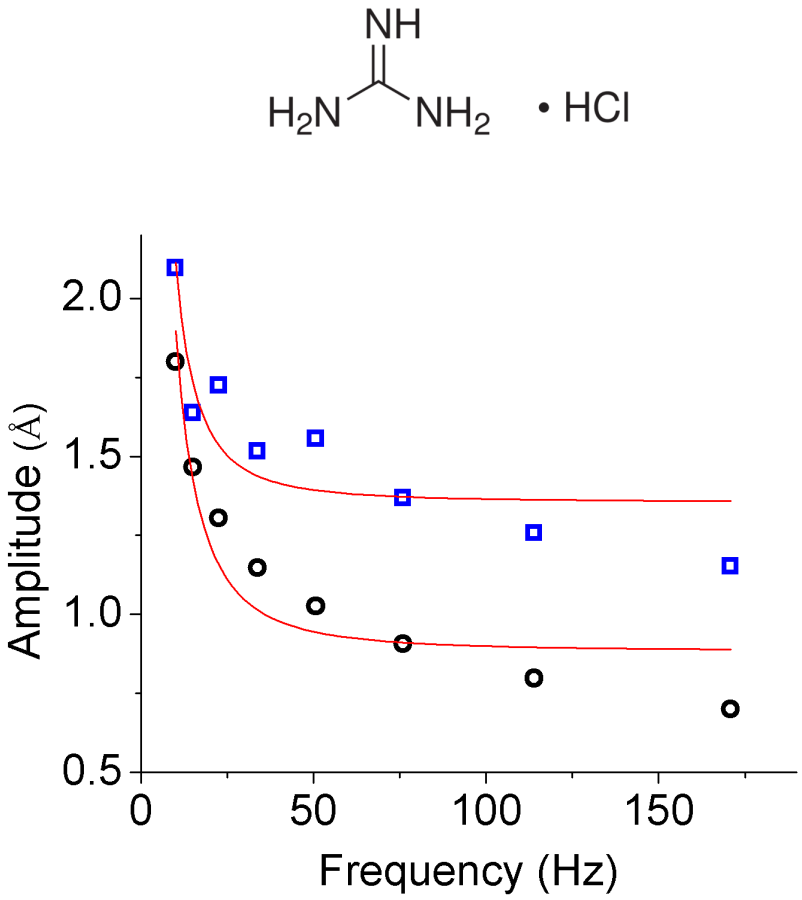

Figure 3.13: Guanidinium Chloride molecular structure and the effect of 0.5M Guanidinium Chloride on the mechanical response of GK. The circles are measurements done in standard condition, and the squares are measurements done after the buffer was changed with the same buffer but containing 0.5M Guanidinium Chloride. Like Urea, unlike DMSO, here the curve shifts upward. Fitting with Eq. 3.1, it is seen that γ (the dissipation coefficient) is not changed much, but it is the elasticity component that changes. These fits reveal that in this experiment κ is decreased by 40%. A decrease in elasticity coefficient means that the enzyme has became softer.

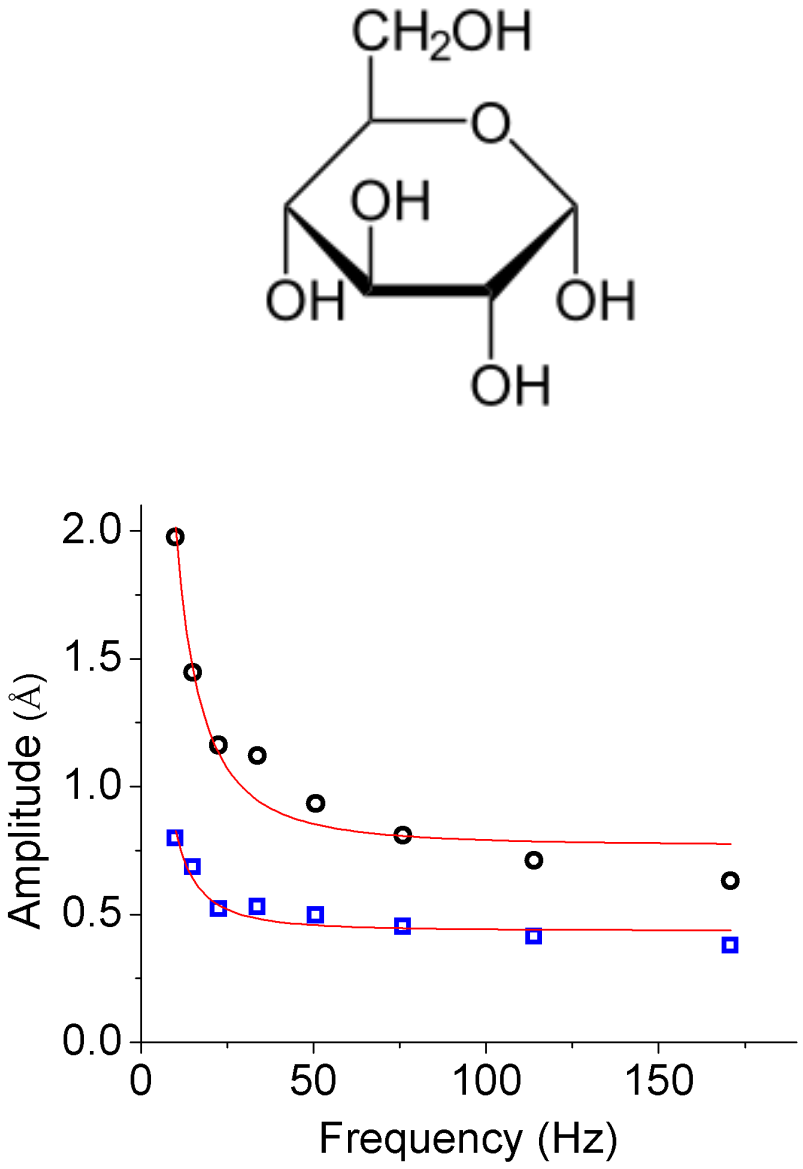

Figure 3.14: Glucose molecular structure and the effect of 0.5M Glucose on the frequency response of GK. The circles are the measurements done in standard condition and the squares are measurements in the presence of 0.5M Glucose. The lines are fits with Eq. 3.1, showing that 0.5M Glucose results in 60% increase in dissipation coefficient γ.

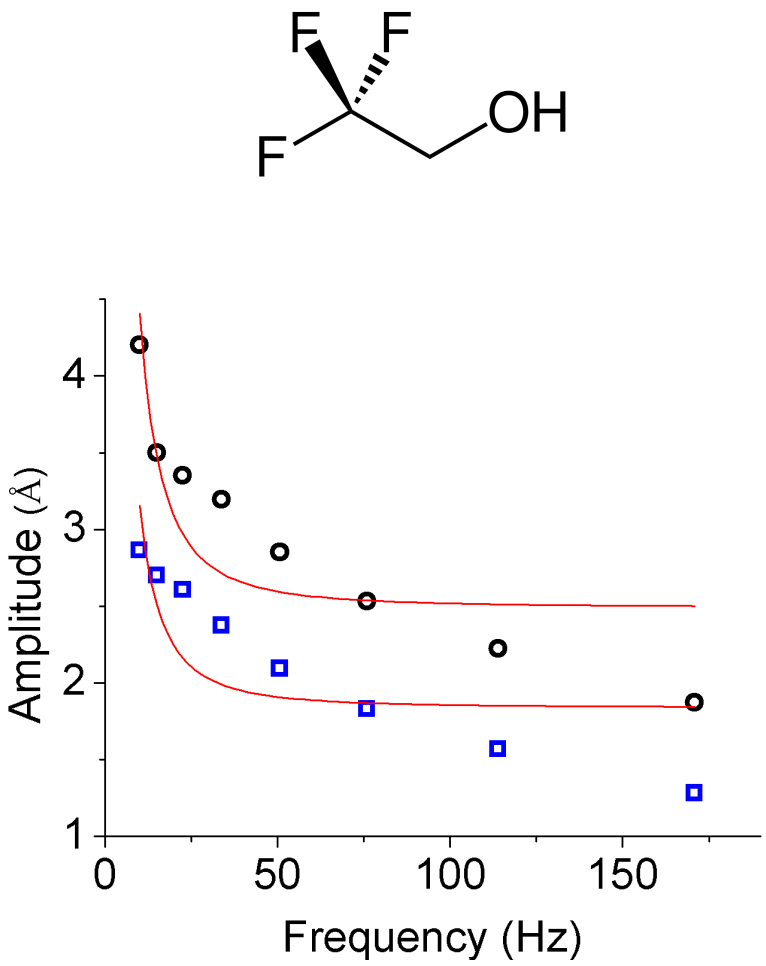

Figure 3.15: The molecular structure of TFE and the effect of 10%v/v TFE on the mechanical response of GK. The circles are measurements at standard condition and the squares are measurements in the presence of 10%v/v TFE. The lines are fits with Eq. 3.1, returning an increase in dissipation coefficient γ by 30%.

Fig. 3.15 shows the chemical structure of TFE and the results of our measurements. Similar to DMSO and Glucose, TFE makes the protein more viscous by increasing the dissipation coefficient γ. It is concluded then that TFE is in fact a kosmotropic agent.

In summary, studying 5 different agents, we have shown that nano-rheology can be used to determine if an agent is kosmotropic or chaotropic, by mechanical means. These measurements were done in collaboration with Dr. Nathalie Casanova.

CHAPTER 4

Probing the Interior: Polymer Chain Contribution

In previous chapters it was shown that driven conformational motion of the enzyme is dissipative and the hydration layer (i.e. the surface of the enzyme) is at least partially responsible for dissipation: chemically perturbing the hydration layer has a big effect on the measured dissipation. In this chapter I am going to look at the contribution of the interior of the molecule in the viscoelastic behavior, by studying the effect of point mutations in the interior of the molecule. Does the dissipation measured by nano-rheology originate from the surface or the interior of the enzyme? This chapter will answer this question.

Global deformations of enzymes are shown to be dependent on both hydration layer and polypeptide chain dynamics. I will show that dissipation originates both from the surface hydration layer and the interior of the molecule, probed by examining the effect of point mutations on the mechanics.

As stated previously, one interesting feature of nano-rheology is that it probes deformation dynamics of the hydration layer and the folded polypeptide structure at time scales from $100\,ms$ to $100\,\mu s$, which are also the time scales of large conformational motion induced by ligand binding, i.e. the time scales of the mechano-chemical cycle of enzymes. In fact, the nano-rheology "cycle" is not so very different from a binding - unbinding cycle. Using nano-rheology we can look at the conformational changes upon ligand binding. There are two hydration layers: one at the enzyme's surface and one at the gold's. When gold and enzyme are pressed together, the hydration layers are compressed and possibly partially expelled from a small surface of contact, and the polypeptide structure also deforms; when gold and enzyme are pulled apart, the hydration layers and molecule shape go back to their

previous state. Ligand binding similarly perturbs the hydration layers at the surface of contact between interacting molecules. Changes in the mechanics of the enzyme examined, Guanylate Kinase, upon binding its 4 substrates is documented in this chapter. We will see in this chapter that GMP binding stiffens the molecule, ATP and ADP binding softens it, while there is no clear mechanical signature of GDP binding.

This chapter also includes a discussion about a hyperactive two-Gly mutant which is found to possibly trade specificity for speed (ST07; YT10).

To look at the contribution of the polymer chain in the viscoelastic behavior, I studied the effect of point mutation. Specifically, I looked at two mutant proteins: a one-Gly substitution (mutant B1) and a two-Gly substitution (mutant C1). The location of the mutations was chosen in a region, which undergoes high strain during the enzymatic cycle, based on the structures of the open (apo) and closed (GMP bound) conformations of the enzyme (ML16). There is a readily observable effect on the enzymatic activity, the B1 mutant being roughly 10 times slower than the wild type (WT), while C1 is roughly 10 times *faster*, is itself a surprising result. However, summarizing the results of many experiments detailed below, it is shown that the effect of the point mutations on the mechanics measured by nano-rheology is relatively small. There is also no dramatic effect on the binding constants of substrates and products, which is perhaps not surprising since the mutations are far from the active site.

In this chapter the same nano-rheology technique (as introduced in Chapter 2) is used. The enzyme under study is also the same GK protein as was used in previous chapters. I present two kinds of measurements: frequency scans, where the frequency of the applied sinusoidal force is varied (at fixed amplitude of the force), and "concentration scans", or binding curves, where the concentration of a ligand (e.g. GMP) is varied, while the response is measured at a fixed frequency (and fixed force amplitude). For both cases, we measure amplitude and phase of the response. The light intensity from the scattering setup is modulated at the forcing frequency, reflecting the synchronous oscillation of the GNPs; this signal, acquired with a photomultiplier, is combined with the reference forcing signal

by a lock-in amplifier (Fig. 2.2), which performs the operations discussed in Chapter 3 to obtain the amplitude and phase of the response. The optical readout is by evanescent wave scattering (JZ97; WZ10) combined with the plasmon resonance of the gold strip and gold nanoparticles (MHT12; AZ15). Using a He-Ne laser (wavelength 633 nm) for illumination, the evanescent wave scatters directly off the GNPs, but it also excites the plasmon resonance in the 30 nm thick gold strip, which excites the plasmon resonance in the GNPs in a distance dependent manner. The result is a much ($\sim$ 500 times) larger scattered intensity and ~ 6 fold larger distance sensitivity compared to scattering off resonance using an Ar (wavelength 488 nm) laser (AZ15). More details are discussed in section 2.4 On the other hand, the force is not calibrated in the experiments, though it has been showed that it is proportional to the applied voltage (WZ11a). I choose the latter so as to operate in the regime of large but reversible deformations, which for this molecule and setup means rms deformation amplitudes $x < 3\,\mathring{A}$ or so. Under these circumstances the enzymes in the apparatus are in their native, functional state; for instance, binding constants for the substrates obtained by nano-rheology are essentially the same as for the enzyme in solution (AZ15).
In the following I use, in discussing the data, the simplest model of visco-elasticity, which is the Maxwell model, discussed in section 2.6.1 and I use Eq. 2.44 to interpret the data.

4.1 Effect of Point Mutations in the Interior of the Enzyme on Mechanics

Having established that the surface of the molecule, which includes the hydration layer, is very important for the mechanics measured in the experiments, I now turn to the question of how important is the interior of the molecule. I prepared two different mutants of GK, substituting Ala 176 with a Gly (Ala176Gly: mutant B1) and substituting Ala 176 and Ala 175 with Gly (mutant C1).

Glycine is the smallest aminoacid, and it was thought that Gly substitutions in the

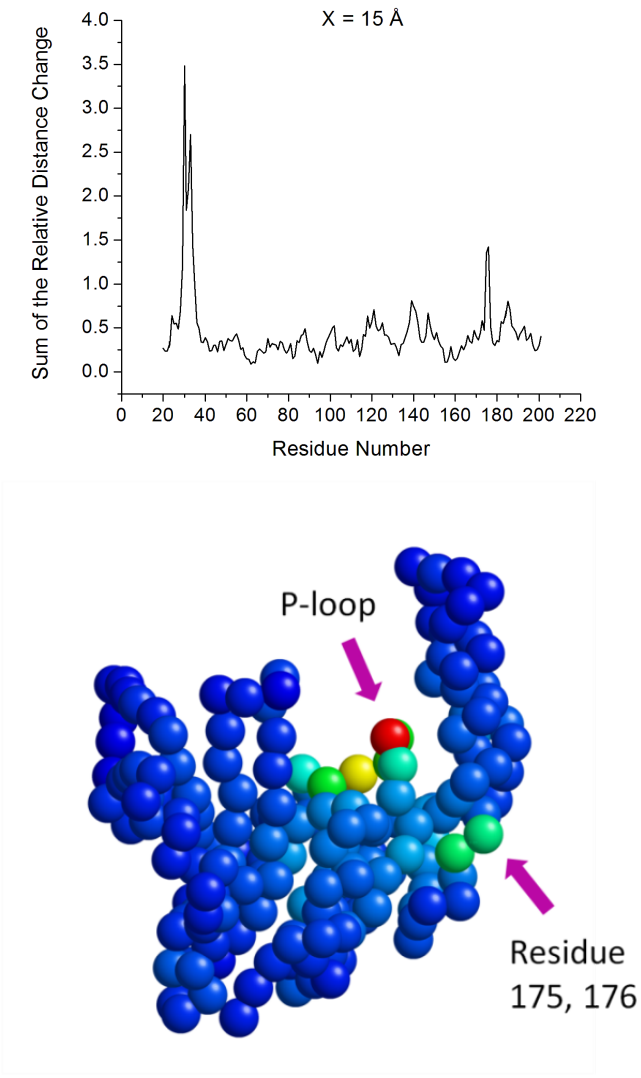

Figure 4.1: (a) Map of the relative distance change of Cα atoms of GK from the open to the closed states; the distance change is averaged over Cα atoms along the chain within a cutoff X ($X = 15\,\mathring{A}$ for this graph). Two major peaks appear in this strain map: one for residues 29-35, which is the p-loop, and another for residues 175-176, the region often called "hinge". The same features appear when varying the cutoff X from $8\,\mathring{A}$ to $18\,\mathring{A}$. (b) Color map of the graph in (a) painted on the GK structure (only Cα atoms are shown), with increasing "strain" from blue to red. The structures used for this map were PDB 1ZNX (closed state) and 1ZNW (open state).

interior would be the least disruptive of the overall structure. Indeed, both mutants are enzymatically active, as seen below. The location of the mutations was chosen in a region that undergoes large strains during the open to closed transition of the enzymatic cycle driven by GMP binding. Namely, we produced a strain map by comparing the open (apo) and closed (GMP bound) x-ray structures of the enzyme (ML16; Hib06) (the corresponding PDB structures are 1ZNX for the closed state and 1ZNW for the open state). A simple measure of "strain" is defined according to:

$$S(n) = \sum_m |\Delta_{nm}^{(o)} - \Delta_{nm}^{(c)}|/\Delta_{nm}^{(o)} \tag{4.1}$$

where $\Delta_{nm}^{(o)}$ is the distance between the Cα carbons of residues n, m in the open structure, $\Delta_{nm}^{(c)}$ is the same for the closed structure, and the sum is over neighbors within a cutoff distance $\Delta_{nm}^{(o)} \leq X$. The resulting S for $X = 15\,\mathring{A}$ is shown in Fig. 4.1, plotted vs residue number n.

This measure does pick out interesting regions of high strain, namely the so-called p-loop around residue 30 (a conserved sequence essential for catalysis in kinases which experiences a large conformational change from the open to the closed state (DS86)) and one more spot around residue 175. The latter is the location chosen for the mutations, as it is distant from the active site. Fig.4.2 shows the result of gel electrophoresis for the three enzymes which was done to check their sizes (see section 5.3).

Fig. 4.3 shows the aminoacid sequence of the two mutants, to be compared with Fig. 2.6. The purple residues are the introduced Cysteines, the yellow Cysteine is the one that appeared unexpectedly and the residues in green are the point mutations introduced for the purpose of this chapter.

Fig. 4.4 shows measurements of the enzymatic activity of the two mutants B1 (Ala176Gly) and C1 (Ala176Gly , Ala175Gly) compared to the WT, using NADH assay (see section 5.4).

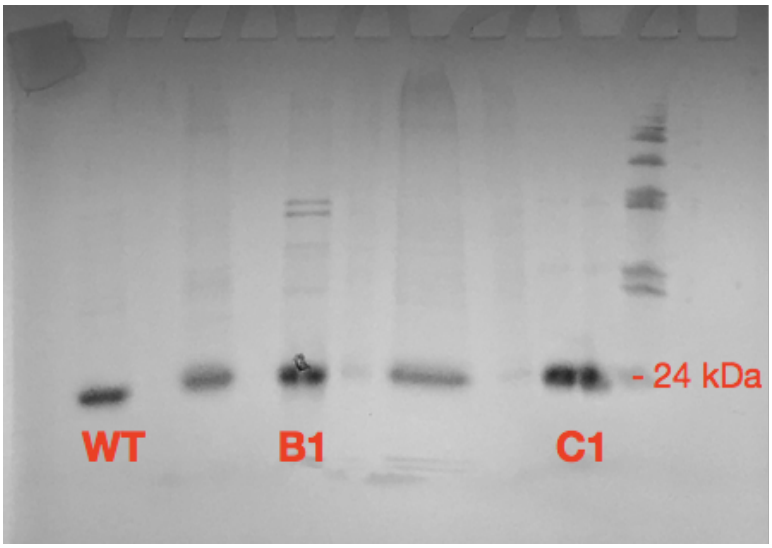

Figure 4.2: Gel electrophoresis done on the three enzymes: The wild type (WT), 1-Gly mutant (B1) and 2-Gly mutant (C1). All are $\sim$ 24 kDa

B1 (slow mutant) Protein sequence:

MAVSXXXXXD TKPTARGQPA AVGRVVVLSG PSAVGKSTVV RSLCERIPNL HFSVSATTRA
PRPGEVDGVD YHFIDPCRFQ QLIDQGELLE WAEIHGGLHR SGTLAQPVRA AAATGVPVLI
EVDLAGARAI KKTMPEAVTV FLAPPSWQDL QARLIGRGTE TADVIQRRLD TACIELAGQG
DFDKVVVNRR LESASAELVS LLVGTAPGSP GVPRGKLAAA LEHHHHHH

C1 (fast mutant) Protein sequence:

MAVSXXXXXD TKPTARGQPA AVGRVVVLSG PSAVGKSTVV RSLCERIPNL HFSVSATTRA
PRPGEVDGVD YHFIDPCRFQ QLIDQGELLE WAEIHGGLHR SGTLAQPVRA AAATGVPVLI
EVDLAGARAI KKTMPEAVTV FLAPPSWQDL QARLIGRGTE TADVIQRRLD TACIELGGQG
DFDKVVVNRR LESASAELVS LLVGTAPGSP GVPRGKLAAA LEHHHHHH

Figure 4.3: The aminoacid sequence of the two mutants, to be compared with Fig. 2.6. The purple residues are the introduced Cysteines, the yellow Cysteine is the one that appeared unexpectedly and the residues in green are the point mutations introduced for the purpose of this chapter.

The bar graph shows the (initial) speed (on a log scale) of the enzymatic reaction under substrate conditions optimal for the WT (initial concentration of GMP 1 mM and ATP 2 mM).

For all measurements, enzyme concentration was the same, as measured by the Bradford assay (see section 5.2) on the stock solutions. We see that the two-Gly mutant C1 is ~ 10 times faster than the WT, while B1 is ~ 10 times slower. Comparing B1 and C1, a single Gly substitution in a "high strain" region away from the active site is found to modulate the reaction speed by a factor 100. Also noteworthy is the surreptitious discovery of the two-Gly mutant which is *faster* than the WT. Since we tend to view biological machinery as "optimized", it is natural to ask what trade-off the C1 mutant may represent. I come back to this question later.

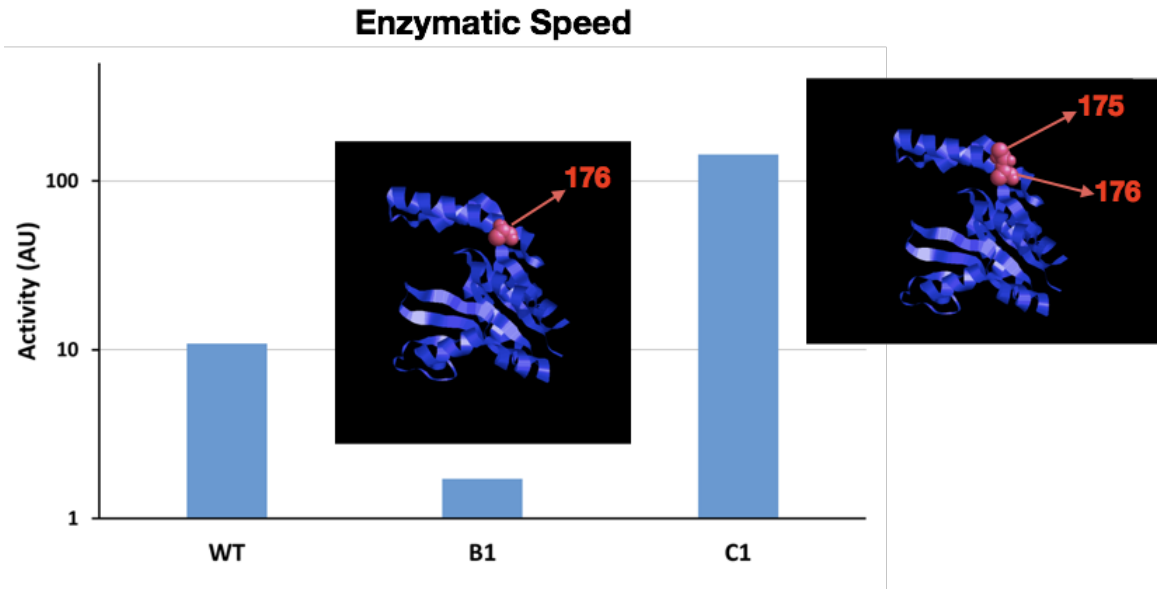

Figure 4.4: Comparison of the enzymatic activity (plotted on a log scale) of the WT and the two mutants. The quantity plotted is the initial speed of the enzymatic reaction, measured with a pyruvate - NADH coupled enzymatic assay (see section 5.4). Conditions were the same for all measurements (optimal conditions for the WT, [GMP] = 1 mM , [ATP] = 2 mM), the nominal enzyme concentration being determined with the Bradford assay (see section 5.2).

I have also obtained (rough) GMP and ATP titration curves of the enzymatic speed for the mutants, which show that any difference in Michaelis-Menten constants (see section 5.4.0.1) between the mutants and the WT, if present, is small. Fig.4.5 shows the ATP titration curves for the two mutants. The factors of 10 in speed are due, within the Michaelis-Menten description, to the rate of the chemical reaction k_{cat}, and not to differences in substrates binding affinities. This conclusion is consistent with the measurements of dissociation constants K_d by nano-rheology which is discussed later for substrates and products. These measurements show that the speed differences are also not due to differences in binding affinity of the products.

Looking for mechanical signatures distinguishing the mutants from the WT, Fig. 4.7 and Fig. 4.8 show representative frequency scans for B1 and C1, to be compared with Fig. 4.6 . Each figure contains the measurements of amplitude (a) and phase (b) of the response, as well as the dissipation (c) introduced in Chapter 3. For the phase and amplitude measurements the fits are with Eq. 2.44 and for the dissipation measurements the fits are with Eq.3.12. The value of F_0/γ obtained from plotting amplitude of response in (a) for all figures is $\simeq 20\mathring{A}/s$, which agrees with the corresponding dissipation plots in (c). All figures give similar values for ω_c extracted from the amplitude plots, namely $\omega_c = 170\, rad/s$ for Fig. 4.7 (mutant C1) and $\omega_c = 200\, rad/s$ for Fig. 4.8 (mutant B1) and $\omega_c = 163\, rad/s$ for Fig. 4.6 (WT). The values of A and ω_c obtained from these measurements are summarized in Table 4.1.
Comparing these figures, no evident differences in the mechanics is seen between the three molecules, by looking at individual samples. If there is any mechanical difference among the three enzymes it is relatively small.

Comparing different mutants, which must be done by comparing different samples, is more difficult than comparing different solvent (AAZ15) or temperature (AWT14) conditions, which can be done on the same sample. The reason is the sample to sample variability in the effective proportionality constant between the applied voltage and the actual force on

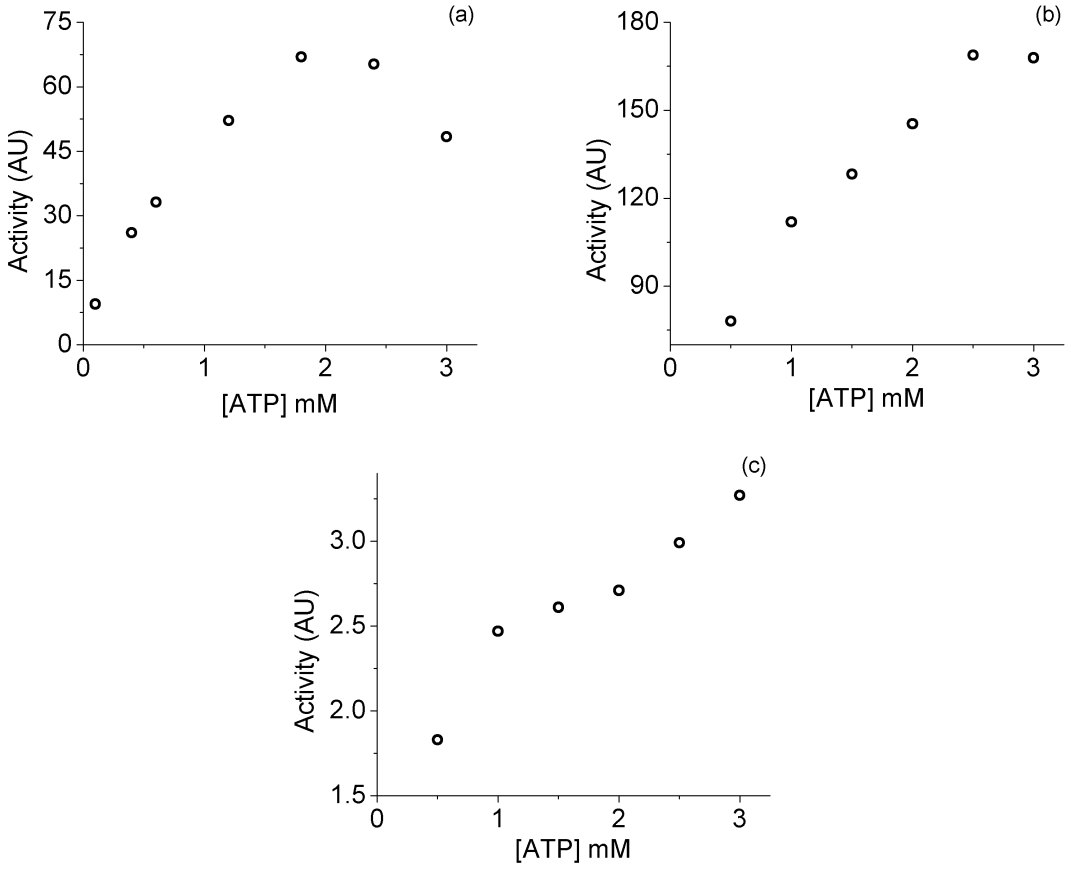

Figure 4.5: ATP titration curves for (a) WT, (b) C1 and (c) B1, using NADH assay explained in section 5.4. The measurements in Fig. 4.4 are done at [ATP] = 2 mM, which is optimal for the WT as seen in this figure. But C1 can be even faster at higher concentrations of ATP. B1 also can be faster, but it is unlikely that higher ATP concentration can increase B1 activity 10 times. The message here is that the result in Fig. 4.4 is definite.

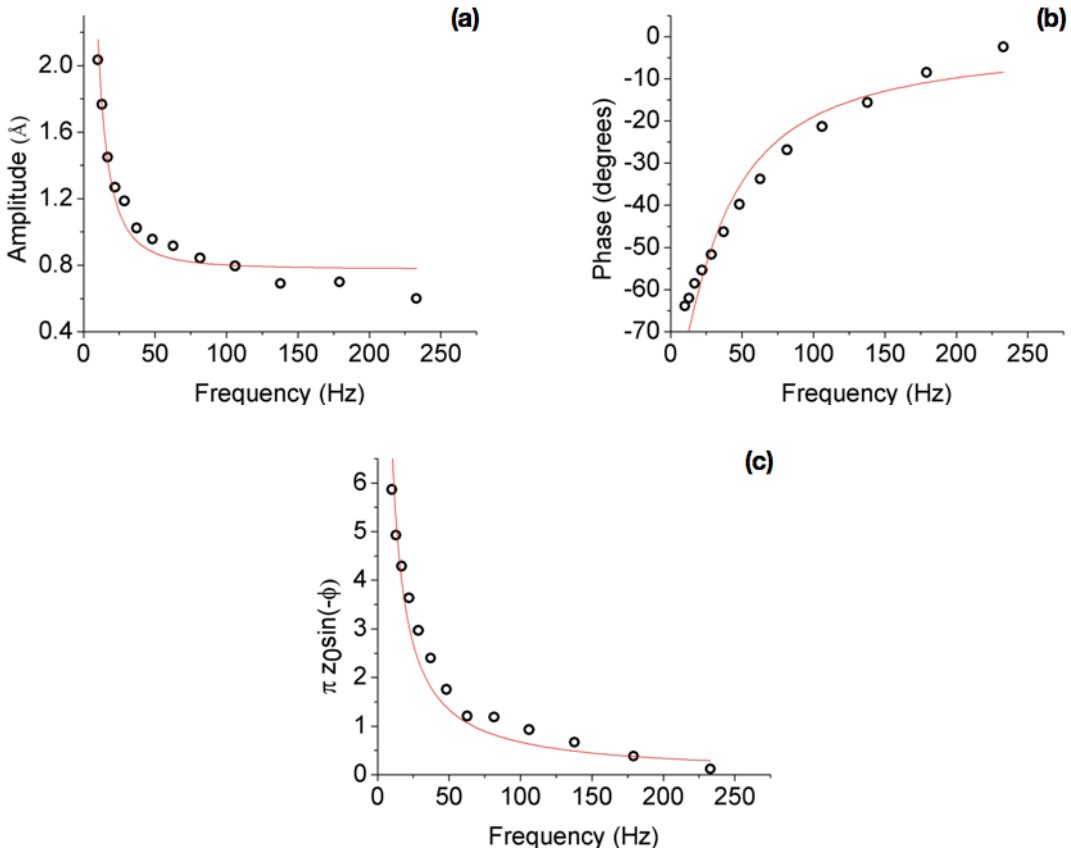

Figure 4.6: Frequency scan showing the mechanical response of the wild type (WT), under our standard conditions (in SSC/3, $50\,mM$ total ionic strength, $pH = 7.0$) (a) RMS amplitude x_0 of the response (in $\mathring{A}$) vs frequency $\nu = \omega/2\pi$ (in $cycles/s$). The line is a fit with Eq. 2.44, returning the values $F_0/\gamma = 20\,\mathring{A}/s$, $\omega_c = 163\,rad/s$, (b) Phase φ of the response vs frequency. The line is a one-parameter fit with Eq. 2.44 , returning $\omega_c = 213\,rad/s$ (c) This plot is a measure of dissipation. For the same data (a) and (b), the quantity $\pi x_0 sin(-\varphi)$ is plotted (in $\mathring{A}$) vs frequency. For the Maxwell model, this quantity is proportional to $1/\omega$ (Eq. 3.12); the line is a one-parameter fit returning the value $F_0/\gamma = 21\,\mathring{A}/s$.

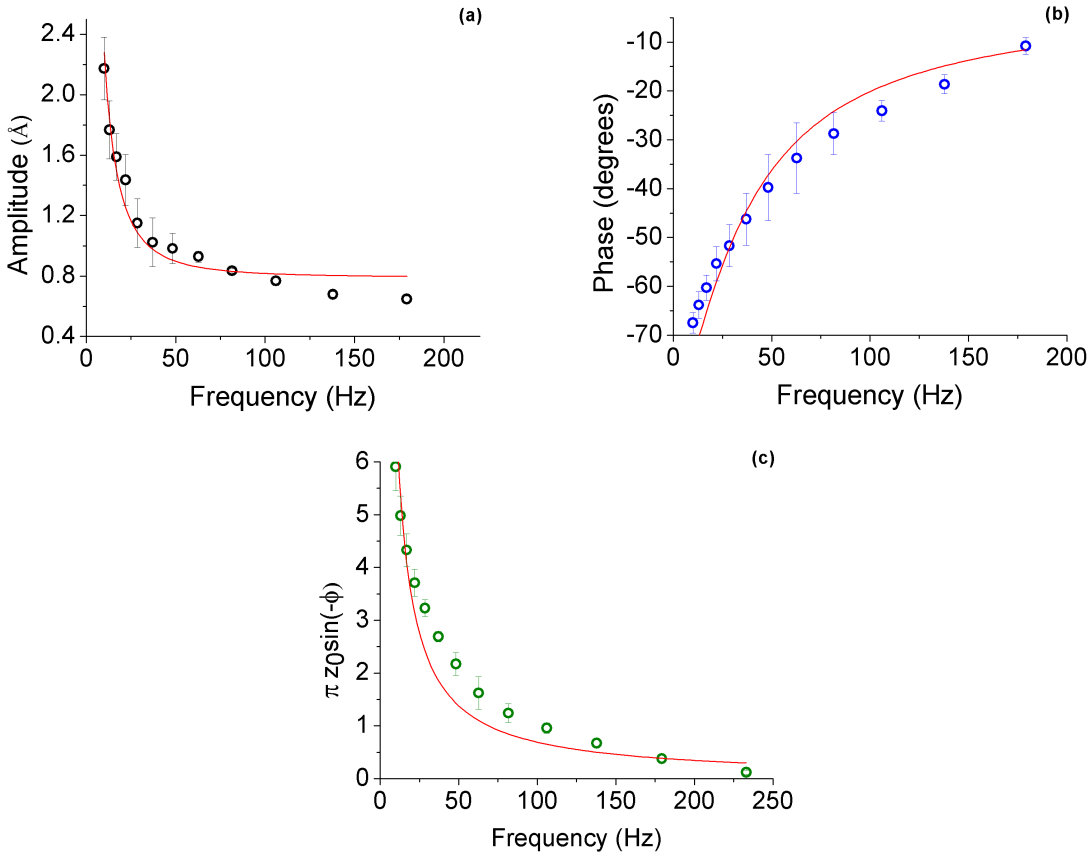

Figure 4.7: Representative nano-rheology frequency scans for the mutant C1. (a), (b), and (c) show, respectively, the rms amplitude of the mechanical response, the phase, and the dissipation (the quantity $\pi x_0 sin(-\varphi)$). The lines in (a) and (b) fits with Eq. 2.44, returning the values $F_0/\gamma = 21\,\mathring{A}/s$, $\omega_c = 170\,rad/s$ in (a) and $\omega_c = 226\,rad/s$ from (b). The line in (c) is a fit with Eq. 3.12; returning the value $F_0/\gamma = 22\,\mathring{A}/s$.

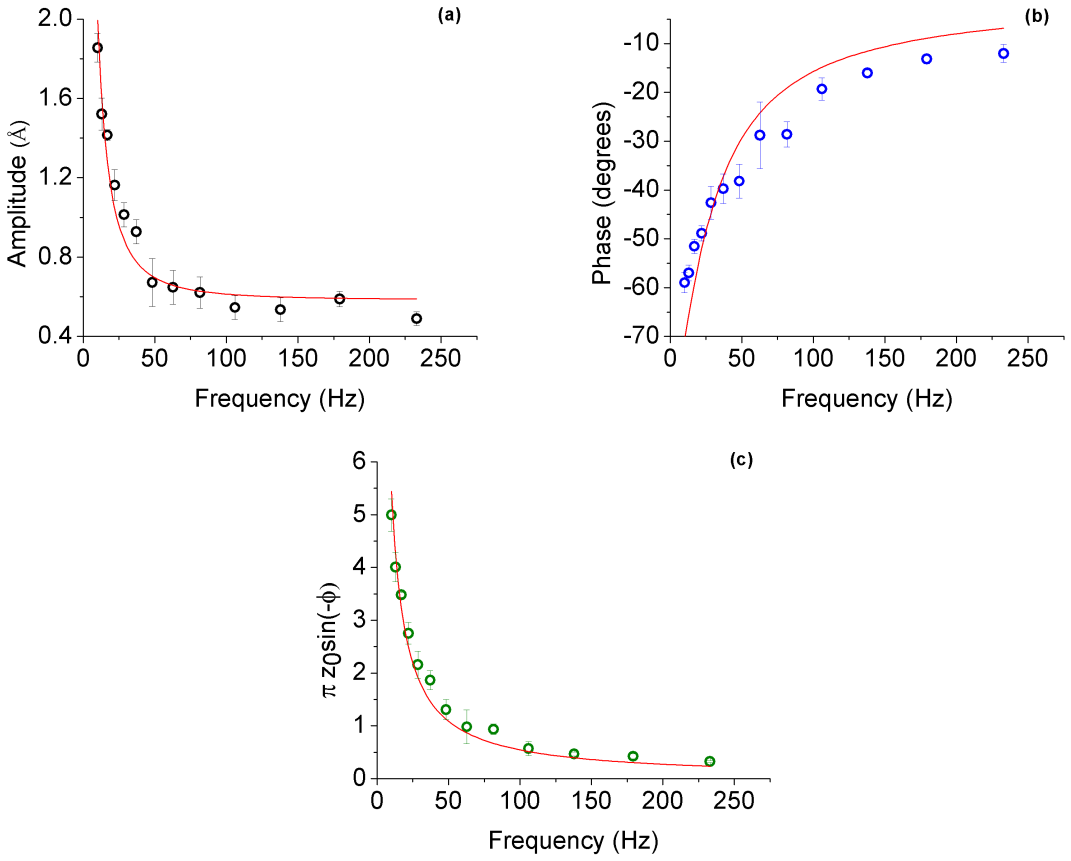

Figure 4.8: Representative nano-rheology frequency scans for the mutant B1. (a), (b), and (c) show, respectively, the rms amplitude of the mechanical response, the phase, and the dissipation (the quantity $\pi x_0 sin(-\varphi)$). The lines in (a) and (b) fits with Eq. 2.44, returning the values $F_0/\gamma = 19\,\mathring{A}/s$, $\omega_c = 200\,rad/s$ in (a) and $\omega_c = 182\,rad/s$ from (b). The line in (c) is a fit with Eq. 3.12; returning the value $F_0/\gamma = 17\,\mathring{A}/s$.

	Amplitude Measurements (a)		Phase Measurements (b)	Dissipation Measurements (c)
Enzyme	A($\mathring{A}/s$)	$\omega_c(Hz)$	$\omega_c(Hz)$	A($\mathring{A}/s$)
WT	20	26	34	21
C1	21	27	36	22
B1	19	32	29	17

Table 4.1: Parameters obtained from fitting Figs. 4.6, 4.7 and 4.8 with Maxwell model ($A = F_0/\gamma$ and ω_c) from amplitude and phase of the response and dissipation measurements.

the enzymes, which is not calibrated in the experiments. Nonetheless, some trends emerge, especially after averaging over several samples, as seen below.

To better compare the mechanics of the three mutants I normalized all the data from all the mutants by dividing the amplitude of the response by the magnitude of the applied voltage for the corresponding sample. Then the average of all the data for each mutant was taken and the average amplitude/voltage was plotted versus frequency. The result is shown in Fig. 4.9.

With this normalization and averaging, some trend becomes observable, especially at higher frequencies.

We see a departure from the Maxwell model behavior at high frequencies ($\omega >> \omega_c$), in that the amplitude keeps decreasing with frequency. This effect is more pronounced for C1, compared to the WT. It is natural to associate this behavior with an additional mechanism for dissipation, not included in the Maxwell model. In order to quantify the different behavior of the mutants, I modified the Maxwell model (which can be thought of as representing the dynamics of a spring (κ) and dashpot (γ_1) in series) by adding a second dashpot (γ_2) in parallel with the spring. Fig. 4.10 shows the configuration.

This addition can be thought of as heuristically accounting for the internal dissipation of

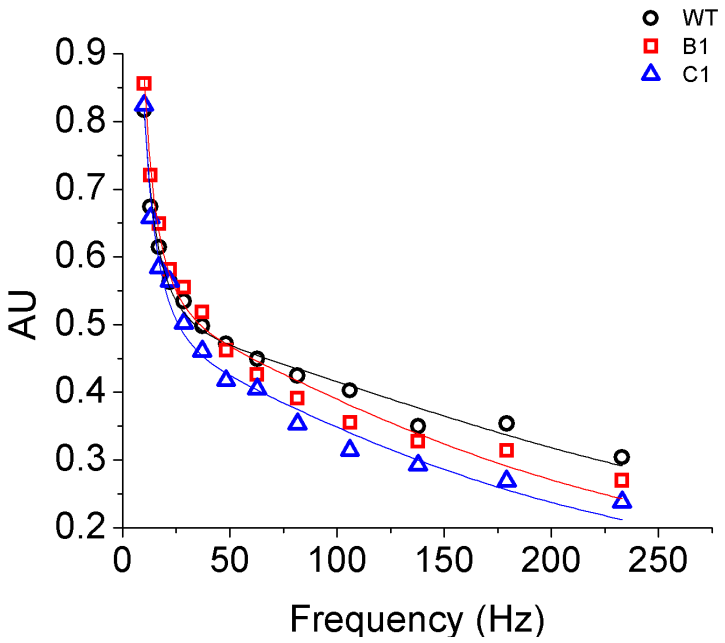

Figure 4.9: Amplitude of the response for the WT (circles), B1 mutant (squares) and C1 mutant (triangles), averaged over several samples. The WT is averaged over 5 different samples, B1 over 4, C1 over 3. Measurements are obtained by SPR enhanced nano-rheology. There are systematic differences in the mechanics, especially between the WT and C1. Namely, in the region $\omega > \omega_c$ the amplitude for C1 decreases faster with frequency compared to the WT. Because this region is not captured well by the Maxwell model, I use a different form to fit the data (see text). Overall, the figure indicates that internal friction (as opposed to surface friction) is increased for C1.

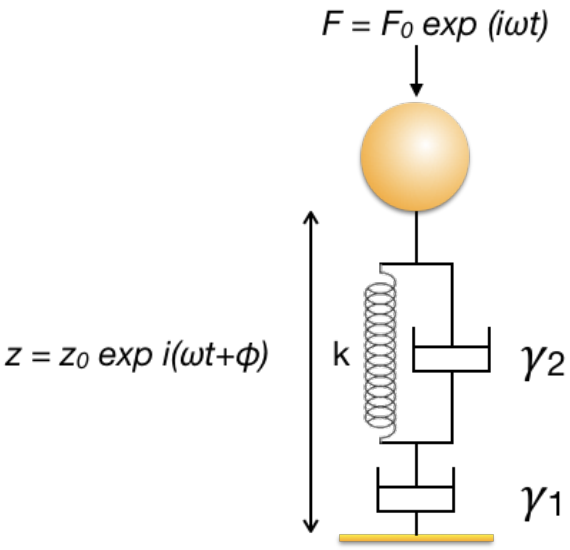

Figure 4.10: Modified Maxwell model (which can be thought of as representing the dynamics of a spring (κ) and dashpot (γ_1) in series) by adding a second dashpot (γ_2) in parallel with the spring.

the molecule, while dissipation at the surface is accounted for by the dashpot in series with the spring. The equation of motion is now:

$$\frac{\gamma_2}{\kappa}\ddot{x} + \dot{x} = \frac{F}{\gamma_1} + \frac{\dot{F}}{\kappa}\left(1 + \frac{\gamma_2}{\gamma_1}\right) \tag{4.2}$$

For an input $F(t) = F_0 e^{i\omega t}$ the amplitude of the response is:

$$x_0(\omega) = \frac{F_0}{\omega\gamma_1}\frac{1}{\frac{\omega_c}{\omega} + r^2\frac{\omega}{\omega_c}}\sqrt{1 + (\frac{\omega_c}{\omega} + (r^2 + r)\frac{\omega}{\omega_c})^2} \tag{4.3}$$

where $\omega_c = \kappa/\gamma_1$, $r = \gamma_2/\gamma_1$, and to reiterate, I associate the dissipation constant γ_1 with the hydration layer, and γ_2 with the interior of the molecule. The lines in Fig. 4.9 are fits with Eq. (4.3), for the WT and C1 (the fit for B1 is not drawn for clarity, and because it is a poor fit). The result is that the difference in behavior between WT and fast (C1) mutant shown in Fig. 4.9 can be attributed to the internal dissipation described by γ_2 , the fits returning the ratio $\gamma_2(C1)/\gamma_2(WT) = 1.4$. In summary, C1 has a higher "internal

viscosity" compared to the WT.

Being able to observe the dissipation at high frequencies was a result of improved detection technique as explained in section 2.5. With these technical improvements it became clear that the amplitude vs frequency response (e.g. Fig. 4.9) is not quite a Maxwell model at high frequency ($\omega > \omega_c$): the amplitude keeps decreasing with frequency, signaling a dissipative contribution even in the "elastic" regime. We associate this contribution with the interior of the enzyme, because this is the feature in the response function which is different between the WT and the C1 mutant. On the other hand, we associate the parameter γ of the Maxwell model description (Eq. 2.44) mostly with the surface of the enzyme, which includes the hydration layer, because we saw in Chapter 3 that this parameter changes dramatically when we perturb the hydration layer with DMSO. The $1/\omega$ viscoelastic "divergence" of the response amplitude at low frequency is however associated with global deformations of the molecule, i.e. deformations of the surface and the interior: if we denature the protein, the response amplitude is feature-less (AWT14).
For driven $\mathring{A}$ size deformations, a large part of the dissipation comes from the hydration layer. This suggests to us that the same is probably true for large conformational motion driven by ligand binding (the induced fit mechanism (Kos94)): in this case also the two interacting molecular surfaces (say GMP and the nucleotide binding site on GK) squeeze out the hydration layers to come into contact. For hard surfaces, the time course of this process has been beautifully measured by electron microscopy (ALL16).

I also looked at the effect of modifying the hydration layer in the two mutants. As discussed in Chapter 3, the hydration layer was modified by a small concentration of DMSO. Fig. 4.11 shows the results. The same effect as seen for the WT is also seen for the mutants: DMSO makes the enzyme more dissipative.

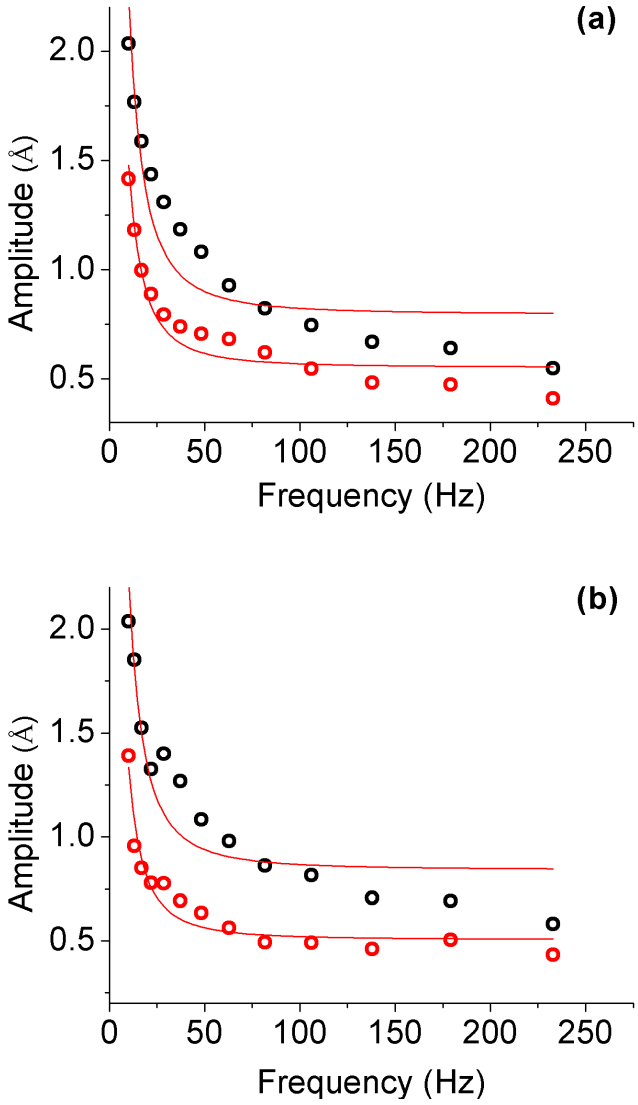

Figure 4.11: Measurements of amplitude of response versus frequency of the applied force for (a) C1 and (b) B1. The black circles are measurements under our standard conditions (in SSC/3, 50 mM total ionic strength, $pH = 7.0$). The red circles are measurements with the addition of 0.5 % DMSO (a kosmotropic agent affecting the hydration layer; see Chapter 3. Similar to what was shown for WT in Chapter 3, 0.5% DMSO ($\sim$ 70 mM) increases the dissipation coefficient γ by 40% for both mutants.

4.2 Ligand Binding Detection

It has been previously reported that ligand binding to the enzyme carries a mechanical signature which can be detected by nano-rheology (AZ15). Titrating in the ligand, one can obtain binding isotherms and measure the dissociation constant K_d; the value thus obtained is the same as that obtained by traditional spectroscopy with the molecule in solution, as shown in (AZ15). My next step was to probe whether this signature is different for the different mutants, potentially a "second order" mechanical effect. In the process of examining this question it was also discovered that the amplitude and phase of the rheological response are complementary measurements with respect to detecting ligand binding, in the sense that in some cases, only the phase, in other cases, only the amplitude, shows a clear signature of ligand binding, in addition to cases where both phase and amplitude are affected.
As stated earlier, GK is the enzyme to the reaction of phosphorylation of GMP:

$$GMP + ATP \overset{\text{GK}}{\rightleftharpoons} GDP + ADP \tag{4.4}$$

The 4 ligands are ATP, GMP (substrates) and ADP, GDP (products). Fig. 4.12 shows the structure of these 4 molecules.

The effect of ligand binding on the quantities directly measured by nano-rheology is relatively small for the present system: $\sim 10\,\%$ change in response amplitude, a few degrees change in the phase. Sub-$\mathring{A}$ resolution in the measurements is necessary to observe these changes. Keeping this in mind, the differences in the mechanical response observed between the WT and the two-Gly mutant (Fig. 4.9) appear the more significant. It is also noteworthy that ligand binding leads for some ligands to a stiffening of the structure, and for other ligands to a softening. For GK, binding of ATP and ADP makes the structure softer, while binding of GMP makes it stiffer. With GDP there is no clear signature. Below I will represent the measurements for ligand bindings for the three enzymes.

Fig. 4.13 shows, for the C1 mutant and the WT, experiments where the concentration

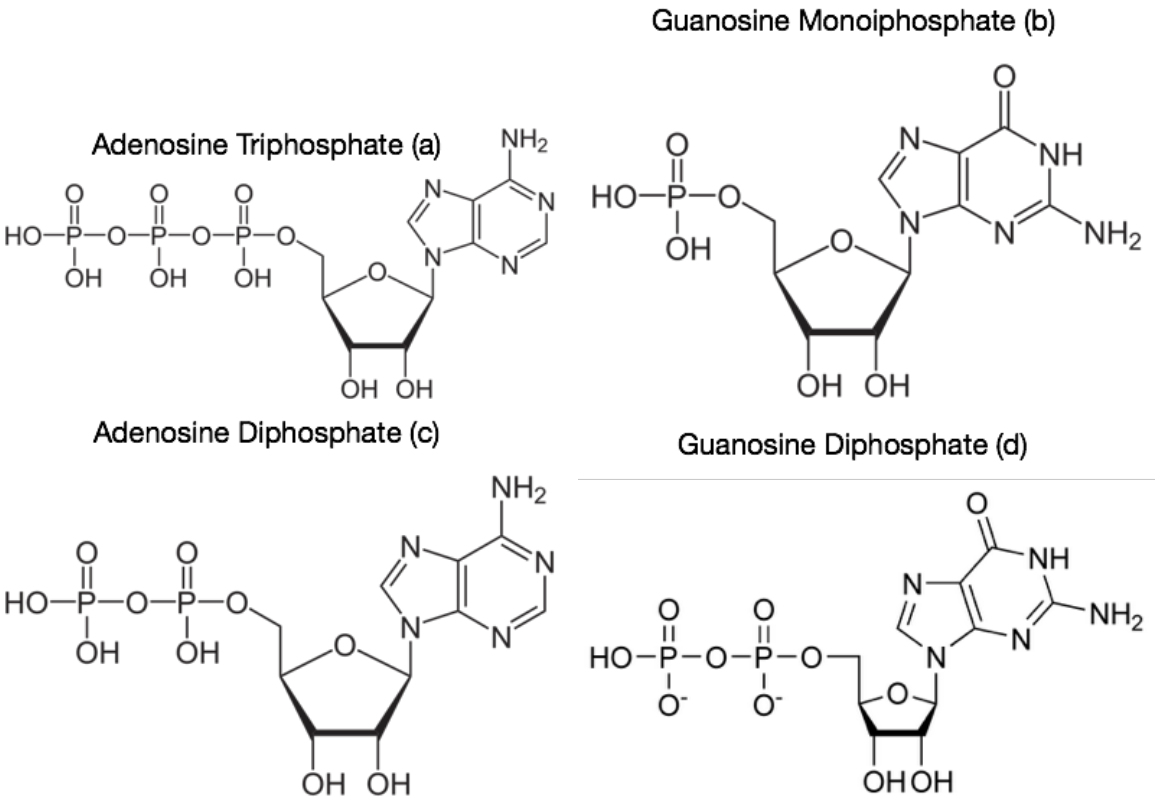

Figure 4.12: Skeletal formula of the four ligands: (a) ATP ,(b) GMP ,(c) ADP and (d) GDP.

of a ligand (ATP) is varied while the amplitude of the mechanical response is measured, at a fixed frequency $\nu = 12\,cycles/s$ (and fixed force amplitude). The line is a fit with the two-states binding isotherm:

$$f(C) = \alpha + \frac{\beta}{1 + K_d/C} \tag{4.5}$$

where C is ligand concentration,

For ATP, there is a clear signature in the amplitude, which increases upon binding (i.e. the enzyme becomes floppier). The fit with Eq. 4.5 returns the value $K_d^{ATP}(C1) = 1.2\,mM$, exactly the same as previous measurement on the WT (AZ15), where it was found that $K_d^{ATP}(WT) = 1.2\,mM$.

Fig. 4.14 shows for the C1 mutant, the amplitude and phase of the mechanical response measured at a fixed frequency $\nu = 12\,cycles/s$ (and fixed force amplitude), while the concentration of ADP is varied. The line is a fit with Eq. 4.5. For ADP, the amplitude (a) may show a small ($\sim 0.1\,\mathring{A}$!) increase upon binding, but the data are noisy. On the other hand, the phase (b) shows a clean binding isotherm, increasing by $\sim 2\,deg$ upon ADP binding. The line is a fit with Eq. 4.5

returning the value $K_d^{ADP}(C1) = 230\,\mu M$.

Fig. 4.15 shows the amplitude and phase of the rheological response measured at a fixed frequency $\nu = 12\,cycles/s$ (and fixed force amplitude), for different concentrations of ADP binding to the WT, measured by SPR enhanced nao-rheology. Here too ADP binding is not very visible in the amplitude (a) but there is a clear signature in the phase (b). The fit with (4.5) gives $K_d^{ATP}(WT) = 240\,\mu M$, essentially the same as the value for C1.

Fig. 4.16 and Fig. 4.17 show the results for GDP binding for C1 and WT, respectively. GDP binding does not carry a clear mechanical signature either in the amplitude (a) or phase (b) (supposing, of course, that GDP does bind at concentrations $< 10\,\mu M$, which is the range explored in Figs. 4.16 and 4.17).

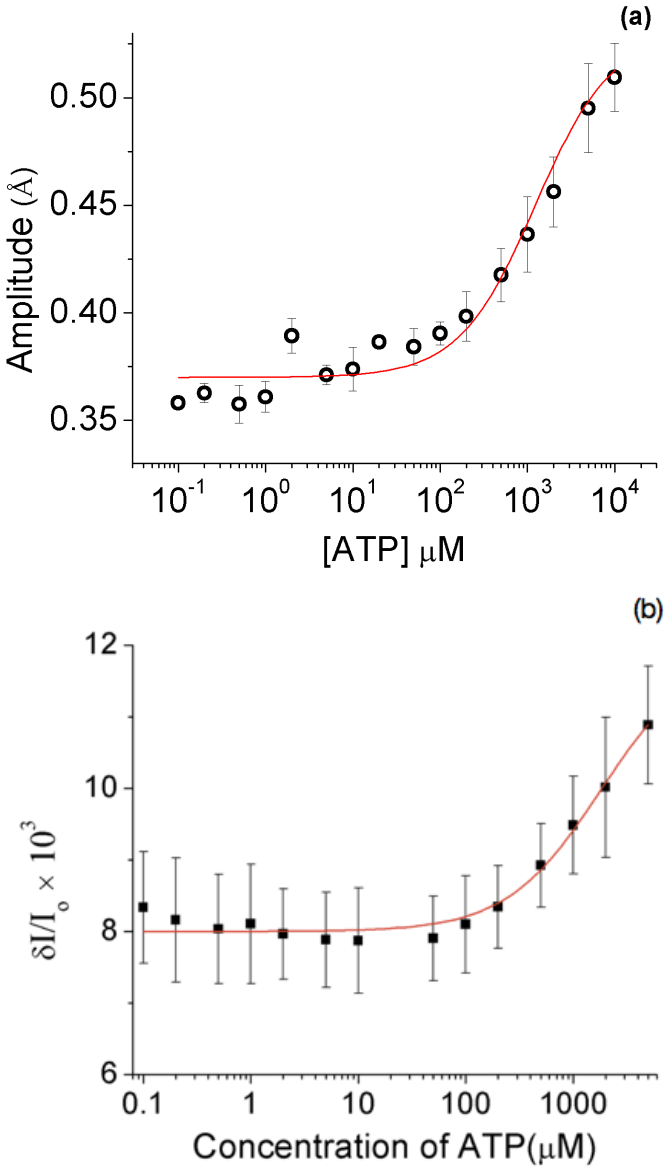

Figure 4.13: Binding isotherms for ATP, measured by SPR enhanced nano-rheology for (a) the "fast" mutant C1 and (b) the wild type (WT- adapted from (AZ15)). Displayed are the amplitude signals vs ligand concentration, measured at the fixed frequency $\nu = 12\,Hz$. The lines are fits with Eq. 4.5, yielding $K_d^{ATP}(C1) = 1.2\,mM$ and $K_d^{ATP}(WT) = 1.2\,mM$.

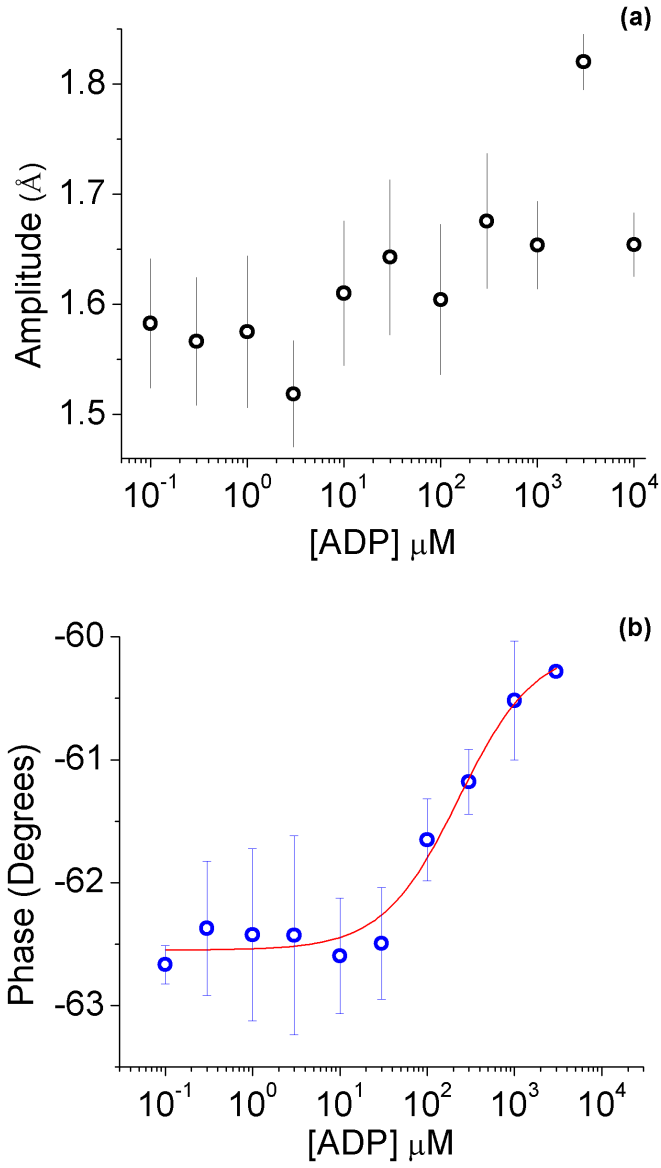

Figure 4.14: Binding isotherms for ADP measured by SPR enhanced nano-rheology for the "fast" mutant C1. Displayed are the amplitude (a) and phase (b) signals vs ligand concentration, measured at the the fixed frequency $\nu = 12\,Hz$. For ADP, the amplitude signal (a) is unclear, whereas the phase (b) shows a clear signature of binding. The line is a fit with the two-states binding isotherm Eq. 4.5, yielding the dissociation constant $K_d^{ADP}(C1) = 230\,\mu M$.

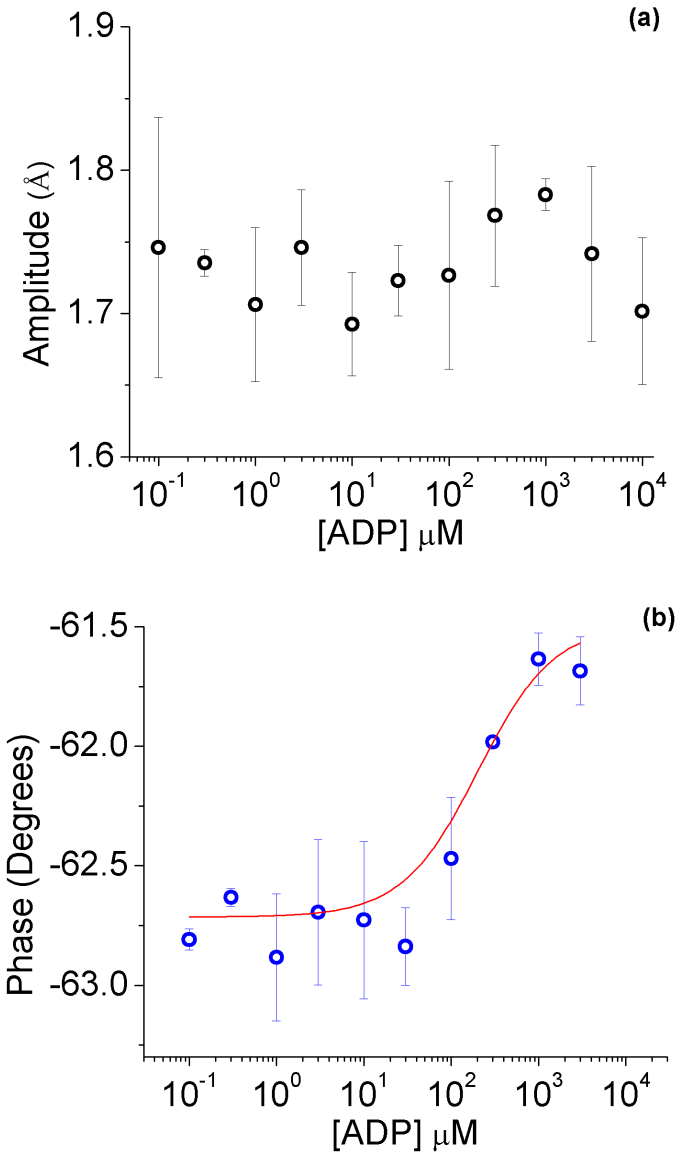

Figure 4.15: ADP binding isotherms obtained by SPR enhanced nano-rheology for the WT. Similar to C1, the signature of ADP binding is not clear in the amplitude (a), but is visible in the phase (b). The line is a fit with Eq. 4.5, giving $K_d^{ADP}(WT) = 240\,\mu M$.

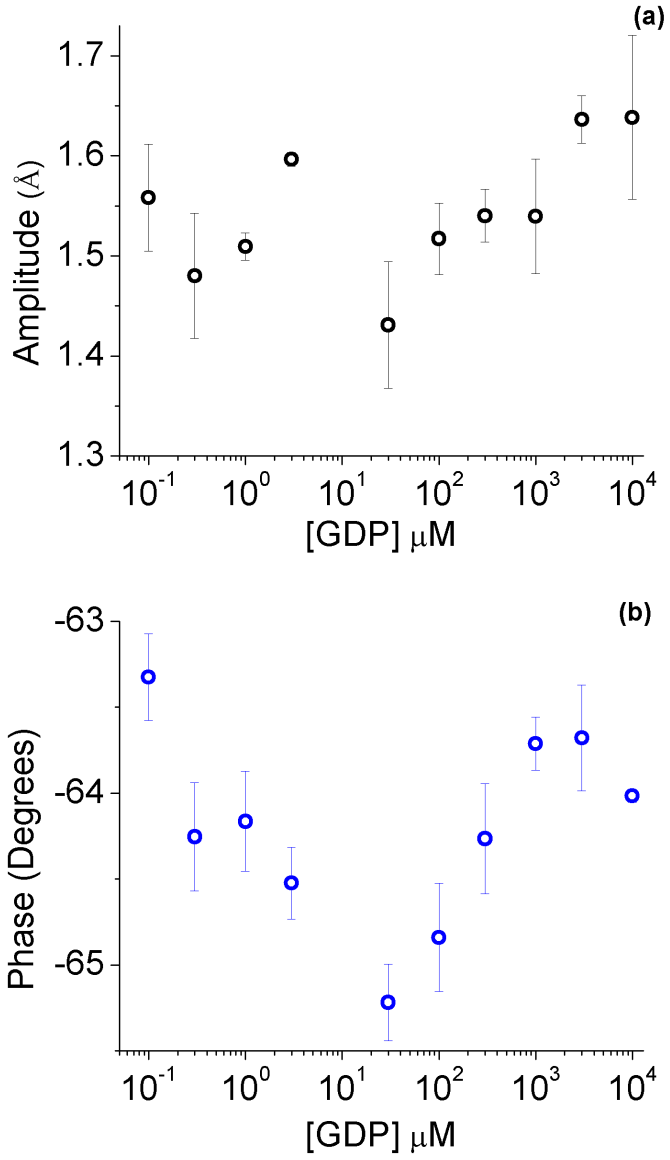

Figure 4.16: Binding isotherms for GDP, measured by SPR enhanced nano-rheology for the "fast" mutant C1. Displayed are the amplitude (a) and phase (b) signals vs ligand concentration, measured at the the fixed frequency $\nu = 12\,Hz$. For GDP, there is no signal above the scatter of the data, both for the amplitude (a) and the phase (b).

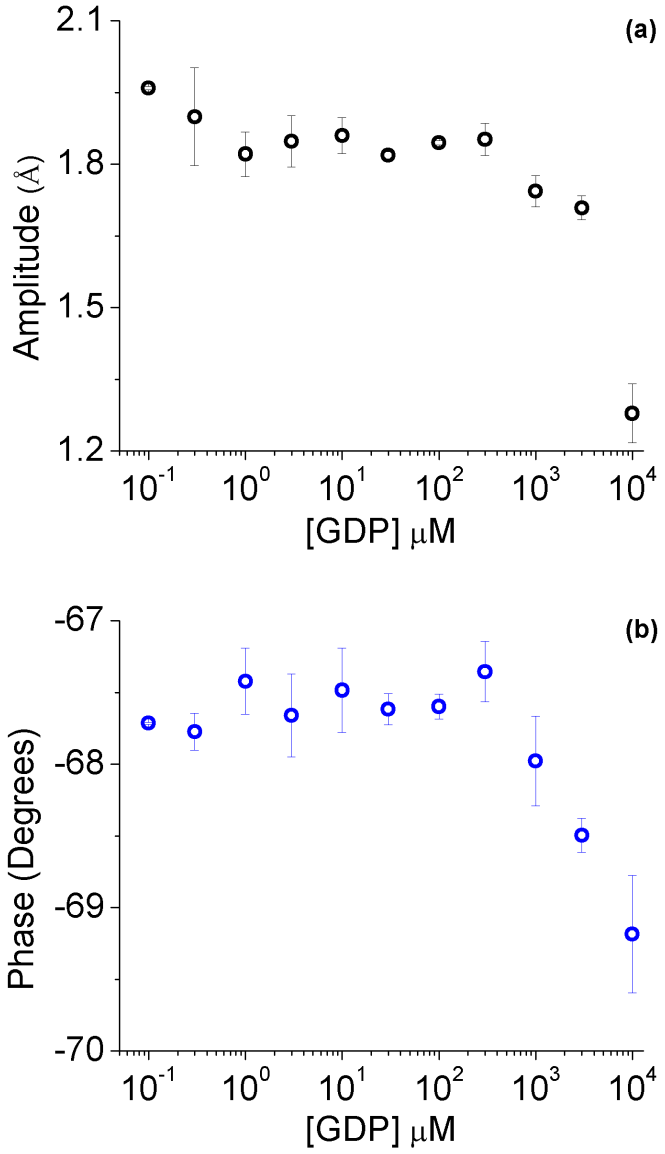

Figure 4.17: GDP binding isotherms obtained by SPR enhanced nano-rheology for the WT. Similar to C1, there is no clear signature of GDP binding either in the amplitude (a) or phase (b) for concentrations $[GDP] < 1\,mM$.

Finally I looked at the mechanical signature of GMP binding. Lets first look at B1, the slow mutant. Fig. 4.18 shows the measurements of the phase and amplitude of response at fixed frequency and amplitude of the applied force, for different concentrations of GMP. For B1, both amplitude (a) and phase (b) lead to well defined binding curves. The amplitude decreases by about 20 % (or $0.4\,\mathring{A}$ working with $\sim 2\,\mathring{A}$ size deformations), and the phase decreases by $\sim 3\,deg.$ The enzyme becomes stiffer upon binding GMP, as reported previously (WZ10; AZ15). The lines are fits with (4.5), returning the values $K_d^{GMP}(B1) = 5.7\,\mu M$ from the amplitude measurements (a) and essentially the same value $K_d^{GMP}(B1) = 4.6\,\mu M$ from the phase measurements (b). Fig. 4.19 adapted from (AZ15), shows the measurements of amplitude of response for GMP binding to WT, at fixed frequency and amplitude of the applied force. The dissociation constant for the WT, which was reported previously (AZ15), is the same: $K_d^{GMP}(WT) = 4.7\,\mu M$.

In Fig. 4.20 we show the rheological response to GMP for C1. In contrast to B1 and WT, the GMP binding curves for the fast mutant C1 show a new phenomenon. The amplitude (a) decreases in two steps, centered around $[GMP] \approx 5\,\mu M$ and $[GMP] \approx 600\,\mu M$. This binding curve has been repeated a second time with an independent sample, and the same feature appears.

This result is interpreted as evidence that at high concentrations a second GMP molecule binds the enzyme, presumably occupying the ATP binding site. In this spirit, the line in (a) is a fit with a three-states binding equation:

$$f(C) = \alpha + \frac{\beta_1}{1 + K_d^{low}/C} + \frac{\beta_2}{1 + K_d^{high}/C} \tag{4.6}$$

returning the values $K_d^{low-GMP}(C1) = 5.2\,\mu M$ and $K_d^{high-GMP}(C1) = 620\,\mu M$. The lower binding constant is the same as for the B1 mutant and the WT. On the other hand, the phase signal (b) is scattered, possibly due to the *collusion* of these two binding events.

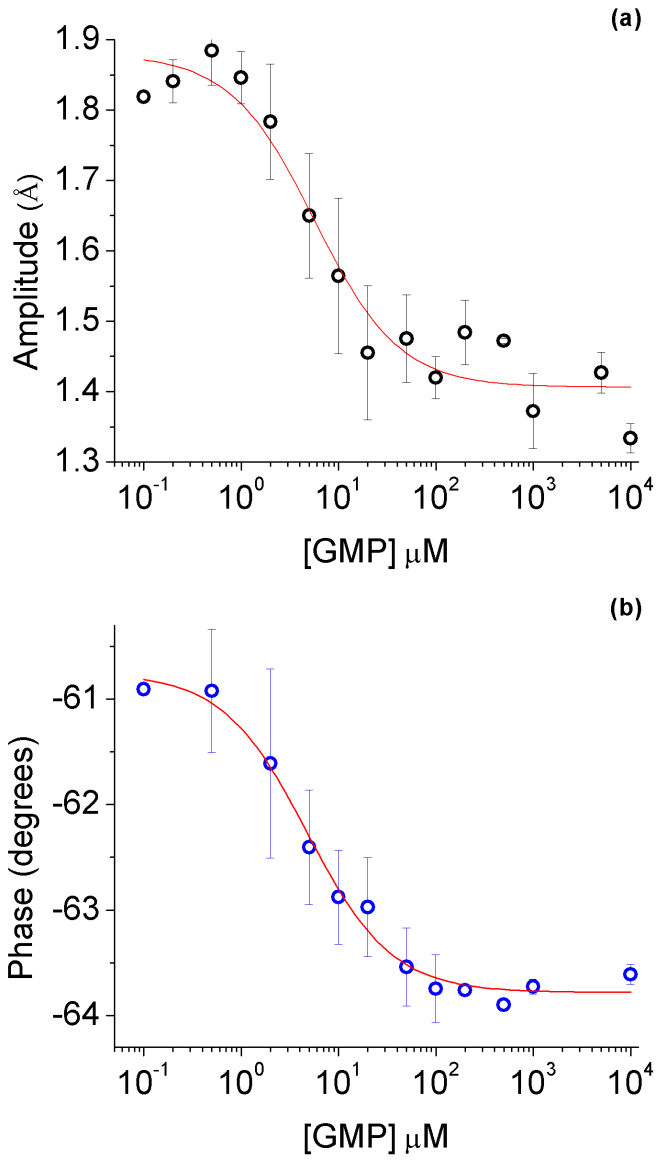

Figure 4.18: GMP binding curves for B1, the slow mutant, measured by SPR enhanced nano-rheology. This mutant becomes stiffer upon binding GMP, as does the WT (AZ15). For B1, both the amplitude (a) and phase (b) carry a signature of GMP binding; fitting with Eq. 4.5 returns the values $K_d^{GMP}(B1) = 5.7\,\mu M$ from (a) and $K_d^{GMP}(B1) = 4.6\,\mu M$ from (b).

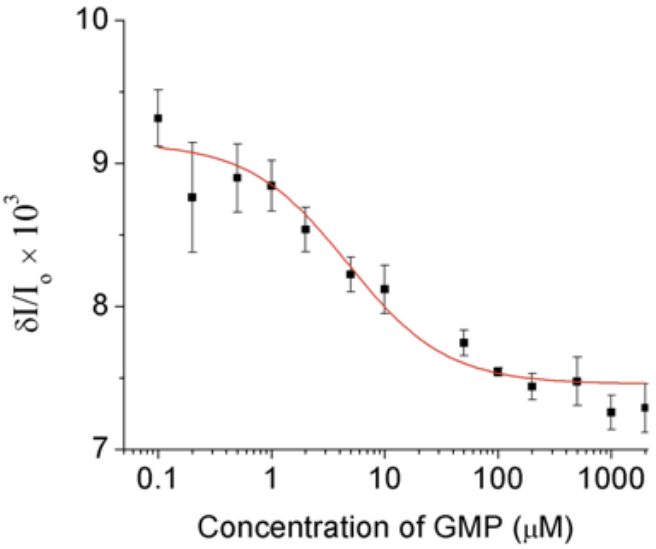

Figure 4.19: Adapted from (AZ15), this graph shows the binding isotherm for GMP for the wild type (WT), measured by SPR enhanced nano-rheology. GMP binding is detected through the stiffening of the enzyme. The line is a fit with Eq. 4.5, returning $K_d^{GMP}(WT) = 4.7\,\mu M$

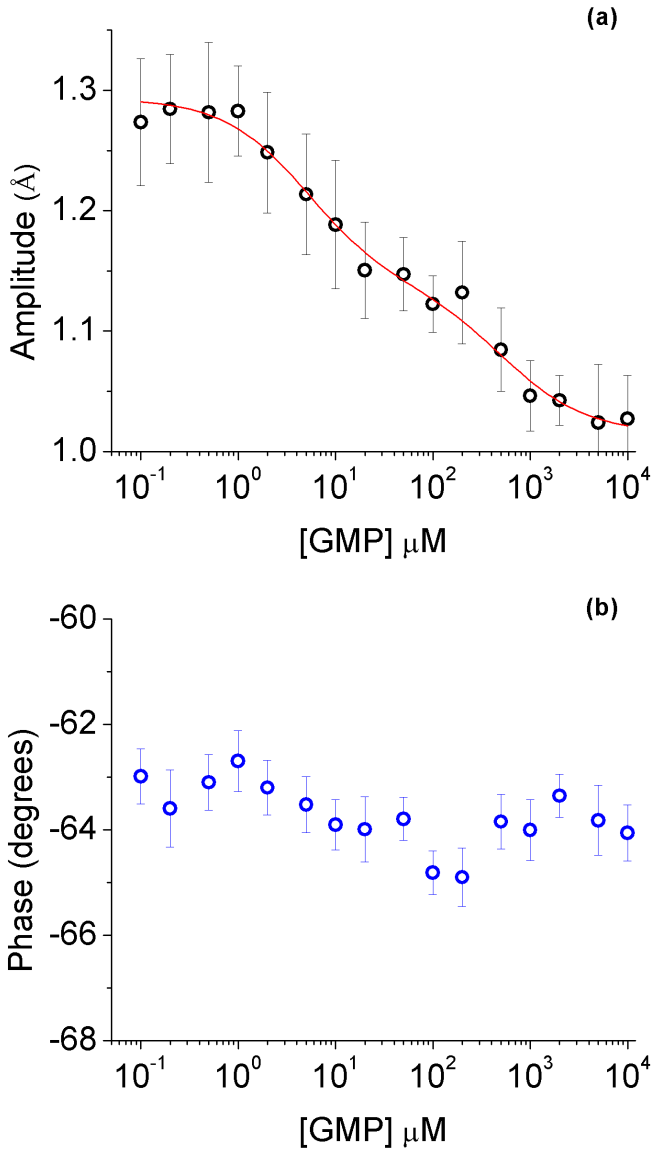

Figure 4.20: GMP binding curves C1 measure by SPR enhanced nano-rheology. The amplitude measurements are shown in (a) and the phase measurements are shown in (b). For C1, the GMP binding curve based on the amplitude (a) shows two binding events, the first with midpoint $[GMP] \approx 5\,\mu M$ and the second at $[GMP] \approx 600\,\mu M$. The line is a fit with Eq4.6. There is no clear signature in phase measurements (b).

The results of ligand binding for all the enzymes and all the ligands are summarized in Table. 4.2

Looking overall at Figs. 4.16-4.20 we find that when ligand binding leads to an increase in response amplitude, the phase also increases, while if the amplitude decreases, so does the phase. In terms of the viscoelastic description, it is easy to see from Eq. 2.44 that this means ligand binding affects primarily the elasticity parameter κ rather than the dissipation parameter γ. For example, from the data of Fig. 4.18b we get $\kappa_{GMP}/\kappa_{apo} = 1.14$ for B1. Of course, this specific value refers to the specific orientation of the molecule in the apparatus achieved in this experiment: the mechanical response of the enzyme is quantitatively different along different directions (TWZ10).

The C1 mutant is more resistive to driven deformations. This observation may support a recent evolutionary model of the emergence of allostery and global deformability as a percolation transition leading to an easily shearable plane in the interior of the enzyme (TLE17). In general it may support the notion of an easily shearable channel spanning the molecule (ML16), which could be disrupted by point mutations. However, our results in this respect are quite preliminary, as we examined only two different mutants. In order to advance the understanding of this question, a more comprehensive study is needed, which is forthcoming (Mos).

4.3 A Hypothesis for Hyperactive Mutant

What is the reason for the 10-fold differences in speed between B1, the WT, and C1 ? Fig. 4.21 shows the molecular structure of GK , in open (a) and closed (b) states [PDB: 1ZNW and 1LVG]. In this figure, the GMP binding domain is shown in red, ATP binding domain in

Enzyme	ATP	GMP	ADP	GDP
WT	$K_d^{GMP} = 4.7\,\mu M$ from amplitude measurements	$K_d^{ATP} = 1.2\,mM$ from amplitude measurements	$K_d^{ADP} = 240\,\mu M$ from phase measurements	no signature
C1	$K_d^{low-GMP} = 5.2\,\mu M$ and $K_d^{high-GMP} = 620\,\mu M$ from amplitude measurements	$K_d^{ATP} = 1.2\,mM$ from amplitude measurements	$K_d^{ADP} = 230\,\mu M$ from phase measurements	no signature
B1	$K_d^{GMP} = 5.7\,\mu M$ from amplitude measurements and $K_d^{GMP} = 4.6\,\mu M$ from phase measurements	no data	no data	no data

Table 4.2: The results of ligand binding for all the enzymes and all the ligands from Figs. 4.13-4.20

violet, residues 075 and 171 (our two Cys handles) in cyan, residue 176 in blue and residue 175 in green. The orange part is a water channel as defined in (OB11). In the closed state, this water channel can potentially enable bound water molecules to interact with the enzymatic site, an interaction possibly crucial to the enzymatic activity [refs]. These structures show that our two mutation points are delicately located near this water channel. Considering that before mutation (in the WT) we had Ala in these two points, a hydrophobic amino acid, and in the mutants we have Gly, which is neither clearly hydrophobic nor hydrophilic, it is plausible that these mutations have altered the characteristic of the water channel. In C1, the *faster* mutant, the extra mutation point (residue 175 in green in Fig. 4.21) is right next to the water channel. This proximity can potentially bring some level of structure in the water molecules, in the closed state. Keeping in mind the importance of structured water molecules at the active site [ref], having a more stable closed state might result in a potential increase in activity, as seen in Fig. 4.4.

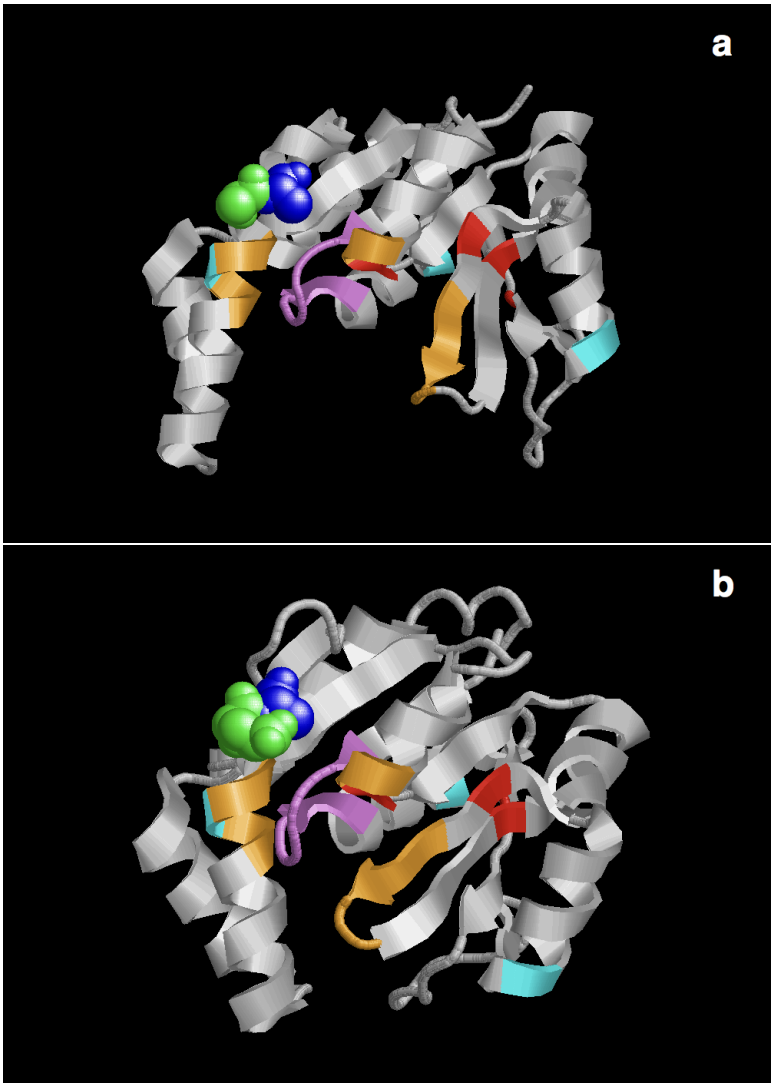

Figure 4.21: Crystal structure of GK. The GMP binding domain is shown in red, ATP binding domain in violet, residues 075 , 171 and 042 in cyan, residue 176 in blue and residue 175 in green. The orange part is a water channel as identified in (OB11). (a) Open state from PDB 1ZNW (b) Closed state from PDB 1LVG

CHAPTER 5

Experimental Techniques and Protocols

5.1 Guanylate Kinase Expression

In summary, to express protein, first we have to send the corresponding plasmid in a suitable cell (Day 1). Then we grow the colonies and transfer them into the culture medium to amplify the amount of cells containing the plasmid (Day 2). When we have enough cells we trick the cells to express the protein. The cells are then concentrated and stored in $-80°C$ to be purified later (Day 3). The whole process takes 3 days. Below is the detailed protocol for expressing Guanylate Kinase:

Day 1: Transformation: sending the plasmid into Rosetta cells and grow the cells on agar plates

Needed chemicals and equipments:

- S.O.C (Super Optimal broth with Catabolite repression, contains glucose) medium from BioLabs
- Rosetta DE 3 cells from Novagen
- AMP (100 mg/ml in water) and CAM (34 mg/ml in ethanol) antibiotics from Sigma
- Ice bucket
- Water bath
- Fire
- LB agar plates (to be made in advance)

- Ethanol (Ethyl Alcohol Denatured) from Fisher Scientific
- Glass Rod
- Incubators

Procedure:

1. Preheat the water bath to 42°C and place the S.O.C tube inside.
2. Thaw Rosetta DE 3 cells on ice (5 $\sim$ 10 minutes) and prepare a tube of 40 μL of it.
3. Add 1 μL of plasmid into the Rosetta DE 3 tube and swirl the tube or tap it gently on the bottom.
4. Incubate the tube on ice (0°C) for 25 $\sim$ 30 minutes.
5. Submerge the tube in the water bath (42°C) for 30 seconds and quickly put it back in ice for 2 minutes. This step is to give the cells a thermal shock to force the plasmids inside the cells. Temperature and timing is very crucial in this step.
6. Add 250 μl of warm S.O.C in to the tube.
7. Incubate the tube at 37°C for 1 hour with 225 rpm shaking. Affix the tube to the bottom of the incubator with a piece of thermal tape.
8. Prepare the antibiotics, take the tube out of the incubator, start the fire and have 3 agar plates ready. The following needs to be done around the fire.
9. Dip 20 μL AMP and 20 μL CAM in the middle of the plate.
10. Add 5-100 μL (different amount for each plate) of the cells in the middle of the plate.
11. Dip the glass rod in Ethanol, sterilize it with fire and let it cool down (by rubbing it with the dish cover if water drops present). Smear the dish with the glass rod and make sure the solution pool is evenly spread.

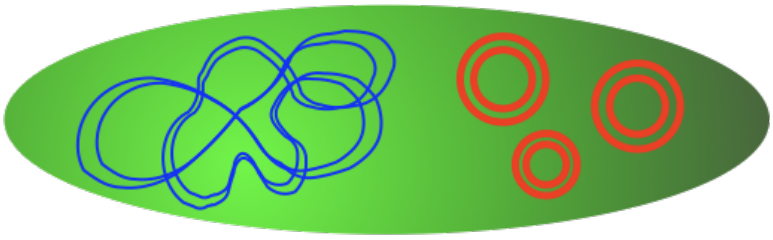

Figure 5.1: Illustration of a bacteria (cell) containg its own chromosal DNA (in blue) and the intoduced plasmid (in red).

12. Label each plate with the date, your name and the amount of cells contained.

13. Incubate the plates (in the small incubator with no shaking) in 37°C overnight (16 $\sim$ 20 hours). Put the dishes up-side-down to prevent the condensed vapor.

Fig. 5.1 illustrates the bacteria (cell) containg its own chromosal DNA (in blue) and the intoduced plasmid (in red). This is the configuration obtained by the end of Day 1.

Day 2: Small scale fermentation and preparing cell culture medium
Needed chemicals and equipments:

- Clean 1L and 2L flasks
- LB Broth from Fisher BioReagents
- Pressure Cooker
- 5mL glass tubes
- AMP and CAM antibiotics
- Fire
- Incubator

Procedure:

1. Start the fire and prepare 3 sterilized 5mL glass tubes. Do the next 3 steps around the fire.

2. Add 5mL of autoclaved LB broth solution (to be prepared in advance) to each tube.

3. Add 5 μL AMP and 5 μL CAM in each tube (1000:1)

4. Take the agar plates from the incubator. Pick 1 colony with a pipette tip (choose the size of the pipette according to the size of the selected colony) to dip into each tube. Try to select colonies that are isolated and far from the edges.

5. Incubate the tubes at 37°C for 5 $\sim$ 6 hour with 225 rpm shaking.

6. In the mean time dissolve 12.5 g LB broth powder in 500mL DI water in a 1L flask. Dissolve 25 g LB broth powder in 1L DI water in each 2L flasks (total of 2 flasks). Swirl the flasks heavily to dissolve the powder.

7. Seal the openings with aluminum foil and autoclave the flasks in the pressure cooker. After 1 $\sim$ 2 hours the pressure reaches 10 Psi. Autoclave at 10 Psi for 20 minutes. The 1L flask and one of the two 2L flasks can be put together. Later autoclave the remaining 2L flask separately. When each autoclave is done, first unplug the pressure cooker and wait until the pressure is back to zero before opening it. Put on heat-resistant gloves when working with the pressure cooker.

8. Label the 2L flasks with your name, date and a warning note (HOT) and set aside to use for tomorrow.

9. Start the fire and work in its vicinity. Add 500 μL AMP and 500 μL CAM in the autoclaved 1L flask (1000:1).

10. Take the glass tubes out of the incubator and choose the best one (opaque in color with no chunk) and pour the containing into the 1L flask.

11. Incubate the 1L flask at 37°C with 225 rpm shaking overnight (16 $\sim$ 20 hours).

Day 3: Fermentation, Induction and Concentration Needed chemicals and equipments:

- Spectrometer and cuvettes
- AMP and CAM antibiotics
- Incubator
- IPTG (2mL of 1M IPTG in water) from Gold Biotechnology
- Centrifuge

Procedure:

1. Take the 1L flask containing the cell culture out of the incubator. Dilute the culture 10× in a cuvette (900 μL LB Broth + 100 μL of cell culture).
2. Prepare a cuvette containing 1mL LB broth to be used as blank
3. Blank the spectrometer at 600nm (scan at fixed wavelength). Measure the O.D. (optical density) of the diluted cell culture at 600nm.
4. Calculate the amount of cell culture needed to be added to each 2L flask to have an O.D. of 0.1 (example: if the O.D. of the diluted culture is 0.3 then the actual culture has an O.D. of 3. Therefore $V_i = 0.1 \times 1000\text{mL} \,/\, 3 \simeq 33\text{mL}$)
5. Add 1mL AMP and 1mL CAM in each 2L flask (1000 : 1).
6. Add the calculated amount of cell culture into each 2L flask and incubate them at 37°C with 225 rpm shaking.
7. After about 2 hours start measuring the O.D. of the cell culture in the flasks every 20 minutes.
8. Prepare 2mL of 1M IPTG. IPTG structurally mimics Lactose and can bind to lac repressor to remove it so that RNA polymerase can bind. Therefore IPTG induce the

cell to start the transcription process and make the desired protein. In this process the cell does not use IPTG and therefore its concentration will remain constant.

9. When the O.D. of the cell culture reaches 0.8∼1 add 1mL of 1M IPTG in each flask to start induction.

10. Keep incubating the flasks at 37°C with 225 rpm shaking for another 4 $\sim$ 6 hours.

11. Prepare two clean 1L Nalgene bottles and pour the content of the flasks into the bottles. Balance the weight of the bottles carefully.

12. Centrifuge the bottles at 4000rpm for 20 minutes. In this process the cells will be separated from the medium.

13. When centrifuge is done, drain the supernatant and keep the cells (keep a little of supernatant and dissolve the cells in it)

14. Put the bottles in the -80°C fridge with a label showing your name, sample name and the date.

Now we have the cells that contain our protein of desire. Next we have to break the cell wall and collect the content of the cells. Then in the purification process we purify our desired protein from this content.

5.2 Bradford Assay

To measure the concentration of protein after purification, Bradford Assay is used. In this spectroscopic method, the solution is first dyed with Protein Assay Dye Reagent Concentrate from Bio-Rad, which contains phosphoric acid and thus is acidic. In this condition the red dye becomes bluer, binding to the protein being assayed. The dye forms a strong, non-covalent bond with the protein's carboxyl group through van der waals force and amino group through electrostatic interactions. The anionic form of the dye (bound to the protein) is blue and

has maximum absorption at 595 nm. By measuring the absorption at this wavelength, the amount of bound dye and therefore the amount of protein is determined. Calibrating this assay with a known concentration of protein one can obtain the concentration of proteins present in any solution.

5.3 Gel Electrophoresis

To check the size of the purified protein molecules, and to check the present proteins in different steps of purification, I used gel electrophoresis. In this method molecules travel thorough an ant convective medium, the gel, in an electric field and the distance they travel is proportional to their charge. Since proteins can have various charges and shapes, they are usually denatured before running the gel. To do so, I used 4x Laemmli Sample Buffer from Bio-Rad which contains SDS (sodium dodecyl sulfate). SDS coats the protein with a negative charge. The amount of SDS bound and thus the charge depends on the size of the protein. Therefore we can separate protein molecules by their size. A standard protein ladder is also loaded in the gel next to the protein under study (Precision Plus Protein Standard . The ladder has various proteins at different sizes and produces different bands at different heights, each corresponding to a specific protein size. I used TGX (Tris-Glycine eXtended) precast gels from Bio-rad, and Tris/Glycine buffer from Bio-Rad was used as the running buffer. Table 5.1 shows the mixture of different samples for checking all the purification steps. To check the polymerization of the eluted protein 355 mM βMe (2-Mercaptoethanol) is used to reduce it.

After preparing the samples, the gel is loaded and placed in the chamber containing the running buffer. The gel is run for 40 minutes at 200mV. When running is done, the gel has to be stained. Depending on the amount of protein present in the sample, I used either Coomassie Stain G-250 from Bio-Rad (for more than 1 ng of protein) or Sypro Ruby from Thermo Fisher (for less than 1 ng of protein) for staining. If using Coomassie the gel needs to be incubated in Coomassie for 1 hour followed by 10 minutes in water to remove the

Sample Name	Sample (μL)	SLB (μL)	Water (μL)	β Me 7M (μL)
Protein Ladder	10	5	5	0
Flow Through	1	9	10	0
Native Wash	10	5	5	0
Imidazole Wash	10	5	5	0
Eluted Protein	10	5	5	0
Reduced Protein	10	4.5	5	0.5

Table 5.1: Protein sample preperation for gel loading. In this example there are 6 samples each with a total volume of $20\mu L$. SLB stands for sample loading buffer

unbounded stain. Coomassie is detectable in visible light and visible light box can be used to see the gel. If using Sypro Ruby, the bands have to be fixed first. To do so, the gel is incubated in Fix buffer (50% methanol and 7% acetic acid) for an hour. Then the gel is put in Sypro Ruby overnight while the container is covered. After that the gel is washed with Wash buffer (10% methanol and 7% acetic acid) for 30 minutes. To see the gel UV light box should be used in this case. Fig. 5.2 shows the result of a GK purification. Comparing each band with the ladder gives an estimate of the size of the corresponding molecule.

In this figure, the first column from right is Imidazole Wash buffer (IW) followed by Eluted protein with β Me (E+), Eluted protein without β Me (E), protein standard ladder, Native Wash buffer (NW) and the last one is Flow Through (FT). Comparing E+ to E, we can see that protein is likely to form dimers and polymers. When reduce, i.e. E+, the size of the protein is determined by comparing the band position to the ladder. In this case, the band is at $\sim$ 25 kDa, which is the right size for GK protein.

5.4 NADH Assay

The reaction rate is measured with GK-NADH activity assay where the GK reaction is coupled to two other downstream reactions:

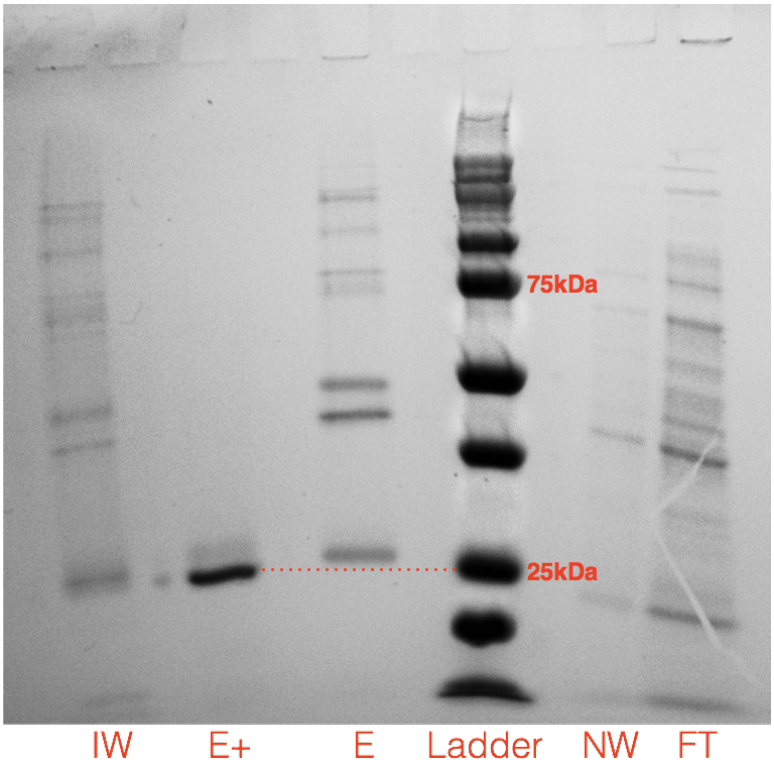

Figure 5.2: GK protein purification results in a TGX gel stained with Coomassie. From left to right, the first column is Imidazole Wash buffer (IW) followed by Eluted protein with β Me (E+), Eluted protein without β Me (E), protein standard ladder, Native Wash buffer (NW) and the last one is Flow Through (FT). Comparing the eluted protein without β Me to the reduced form suggests that the protein has some tendency to form dimers. Comparing Eluted protein with β Me to the ladder shows that if polymer bonds are broken, the reduced protein is at $\sim$ 25 kDa, which is the size of GK, and therefore this gel assures us that the product of the purification has the right size.

$$\begin{cases} GMP + ATP \overset{\text{GK}}{\rightleftharpoons} GDP + ADP \\ ADP(GDP) + PEP \overset{\text{PK}}{\rightleftharpoons} ATP(GTP) + pyruvate \\ 2\,pyruvate + 2\,NADH \overset{\text{LDH}}{\rightleftharpoons} 2\,lactate + 2\,NAD^{+} \end{cases}$$

- PK is Pyruvate Kinase and LDH is the lactate dehydrogenase. (Pyruvate Kinase/ Lactate Dehydrogenase enzymes from rabbit muscle from Sigma).
- PEP is Phosphoenolpyruvic acid from Chem-Impex.
- NADH (reduced Nicotinamide Adenine Dinucleotide), GMP (Guanosine Monophosphate) and ATP (Adenosine Triphosphate) are from Sigma.

The consumption of ATP and GMP are monitored by the decrease of NADH, whose concentration is derived from the fluorescent at 465 nm with calibrated standards (excitation at 365 nm). Measurements are done using BioTek Synergy HT Microplate Reader.
First a mixture with the total volume of 45 μL is made, containing:

- 100 mM Tris HCL
- 100 mM KCL
- $10 mM MgCl_2$
- $150 \mu M NADH$
- 0.5 mg/mL BSA (from BioLabs)
- 10 mM PEP
- 10 units/ml PK and 13.2 units/ml LDH
- 50 nM GK

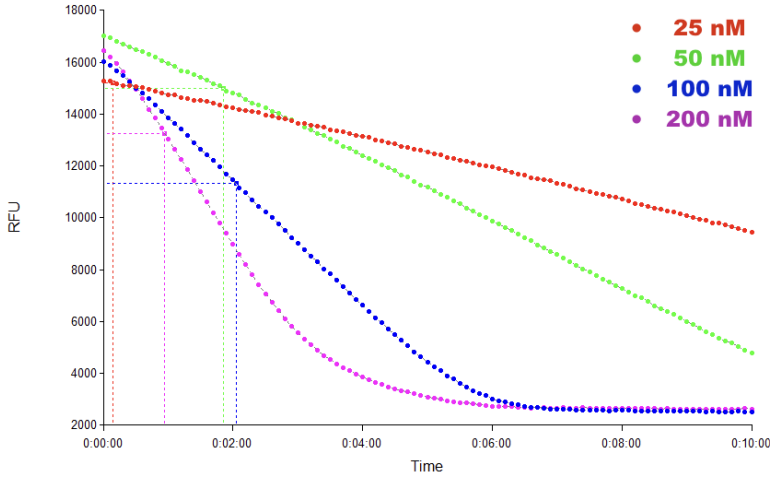

Figure 5.3: GK enzymatic activity detected by NADH assay for different concentrations of GK in the solution. The red line corresponds to the solution containing only 25nM of the enzyme, and it is the slowest. The green line shows the activity of 50nM enzyme. The blue line shows the activity of 100nM GK and finally the purple line shows the activity of 200nM GK and it is the fastest one.

- 2 mM ATP (or GMP) (1 substrate should be added at the end so that the reaction does not start in the preparation process)

Finally $5\mu L$ of 10 mM GMP (or ATP) is added in the last step to make a final volume of $50\mu L$ and to initiate the reaction. The concentration of ATP and GMP is to be optimized for different enzymes.

In order to use this assay, we have to make sure that the reaction under study is the rate-limiting step (slowest reaction). In this condition if the amount of enzyme is doubled the reaction speed will also be doubled. Fig. 5.3 shows the activity of GK protein, using NADH assay, at different concentrations of the enzyme.

Looking at Fig. 5.3 we conclude that as we increase the amount of the enzyme in the solution the speed of the whole reaction increases, which shows that the reaction under study (GK enzymatic activity) is the rate limiting step.

5.4.0.1 MichaelisMenten kinetics

Michaelis-Menten kinetics is a model of enzyme kinetics that describes the rate of enzymatic reaction, relating the reaction rate to the substrate concentration. Consider the reaction below:

$$\mathrm{E} + \mathrm{S} \underset{\mathrm{k_2}}{\overset{\mathrm{k_1}}{\rightleftharpoons}} \mathrm{ES} \xrightarrow{\mathrm{k_{cat}}} \mathrm{E} + \mathrm{P} \tag{5.1}$$

where E is the enzyme, S is the substrate, ES is the enzyme bound to the substrate and P is the product. ks are the rates of each reaction. From 5.1 we can write

$$\frac{d[S]}{dt} = -k_{cat}[ES] \tag{5.2}$$

where [S] is the substrate concentration and [ES] is the concentration of enzyme-substrate complex. Now from a physical approach, we can treat the enzyme-substrate complex as a two state system: the enzyme can be either occupied (bound to the substrate- a.k.a. [ES]) or un-occupied (no substrate attached). Then using Fermi distribution for this 2-state system we can write:

$$P_{occupied} \propto [ES] \simeq \frac{1}{1 + e^{(\epsilon-\mu)/kT}} \times [E_{total}] \tag{5.3}$$

where k is Boltzmann's constant, T is the absolute temperature, ϵ is the energy of the occupied state, and μ is the total chemical potential.

Putting $\mu = kTln[S]$ and $e^{\epsilon/kT} = k_S$ in Eq. 5.3 gives:

$$\frac{d[S]}{dt} = -k_{cat}\frac{[E_{total}]}{1 + k_s/[S]} \tag{5.4}$$

Having $[E_{total}]$ and k values this equation gives the reaction rate (the rate of substrate consumption). To obtain the same equation from a chemical approach, considering that at equilibrium the rate of the change in [ES] is zero we can write:

$$
\begin{aligned}
(\frac{d[ES]}{dt})_{equilibrium} = -k_{cat}[ES]_{equilibrium} - k_2[ES]_{equilibrium} + k_1[E_{free}][S] = 0 \\
\Rightarrow [ES]_{equilibrium} = \frac{k_1}{k_{cat}+k_2}[E_{free}][S]
\end{aligned}
\tag{5.5}
$$

Putting $[ES] + [E_{free}] = [E_{total}]$ in Eq. 5.5 gives:

$$
[ES]_{equilibrium} = \frac{E_{total}}{1 + 1/\alpha[S]} \tag{5.6}
$$

where $\alpha = \frac{k_1}{k_{cat}+k_2}$. Putting this result in Eq. 5.2 we finally get:

$$
\frac{d[S]}{dt} = -k_{cat}\frac{[E_{total}]}{1 + k_s/[S]} \tag{5.7}
$$

where $k_S = \frac{k_2+k_{cat}}{k_1}$.

In our case, the reaction has two substrates: GMP and ATP. Then 5.1 becomes:

$$
\mathrm{E} + \mathrm{S}_1 + \mathrm{S}_2 \longrightarrow \begin{pmatrix} ES_1 \\ ES_2 \\ ES_1S_2 \end{pmatrix} \longrightarrow \mathrm{E} + \mathrm{P} \tag{5.8}
$$

Therefore there are 4 states available: No substrate bound, S_1 bound, S_2 bound and both S_2 and S_1 bound. Writing the partition function for this 4 states system, assuming that S_1 and S_2 are independent, we have:

$$
\begin{aligned}
Z = \underbrace{1}_{\text{no substrate bound}} + \underbrace{e^{-f_1/kT}}_{ES_1} + \underbrace{e^{-f_2/kT}}_{ES_2} + \underbrace{e^{-(f_1+f_2)/kT}}_{ES_1S_2} \\
= (1 + e^{-f_1/kT})(1 + e^{-f_2/kT})
\end{aligned}
\tag{5.9}
$$

where f_1 is the energy of ES_1 state and f_1 is the energy of ES_2 state. Now the probability that S_1 and S_2 are both bound (the condition required for the reaction to start) is $P_{ES_1S_2}$. Like Eq. 5.2 here we have:

$$
\frac{d[S_i]}{dt} = -k_{cat}[ES_1S_2] \tag{5.10}
$$

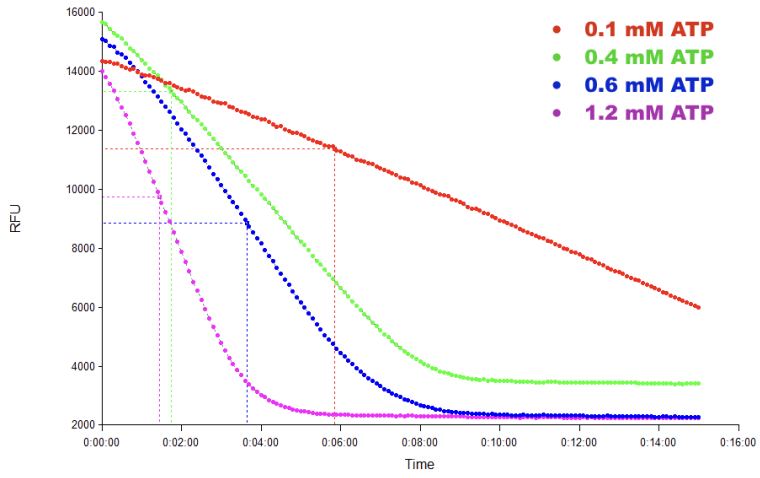

Figure 5.4: ATP titration measurements for GK. Concentration of GK was fixed at 50 nM and GMP concentration was fixed at 1 mM. Enzymatic activity was measured with NADH assay, for different concentrations of ATP.

that is, if both substrates are bound and therefore product is released.

Now like Eq. 5.3 here we have:

$$P_{ES_1S_2} \propto [ES_1S_2] \simeq \frac{e^{-(f_1+f_2)/kT}}{(1+e^{-f_1/kT})(1+e^{-f_2/kT})} \times [E_{total}] \tag{5.11}$$

Rearranging Eq. 5.11 and putting the result in Eq. 5.10 we obtain:

$$\frac{d[S_i]}{dt} = -k_{cat}\frac{[E_{total}]}{(1+k_{s_1}/[S_i])(1+k_{s_2}/[S_i])} \tag{5.12}$$

Fixing $[E_{total}]$ and $[S_1]$, we can find k_{s_2} by measuring the enzymatic activity using NADH assay with different values of $[S_2]$. Plotting $d[S_i]/dt$ (i.e. enzymatic activity) vs $[S_i]$ and fitting with Eq. 5.12 one can obtain k_{s_i}, given that the enzyme concentration and the concentration of the other substrate is fixed. We can find k_{cat} in the limits $[S_1] \gg k_{s_1}$ and $[S_2] \gg k_{s_2}$.

Fig.5.4 shows ATP titration measurements for GK.

In this experiment the concentration of GK was fixed at 50 nM and GMP concentration is fixed at 1 mM. Different solutions with different ATP concentrations were made and the

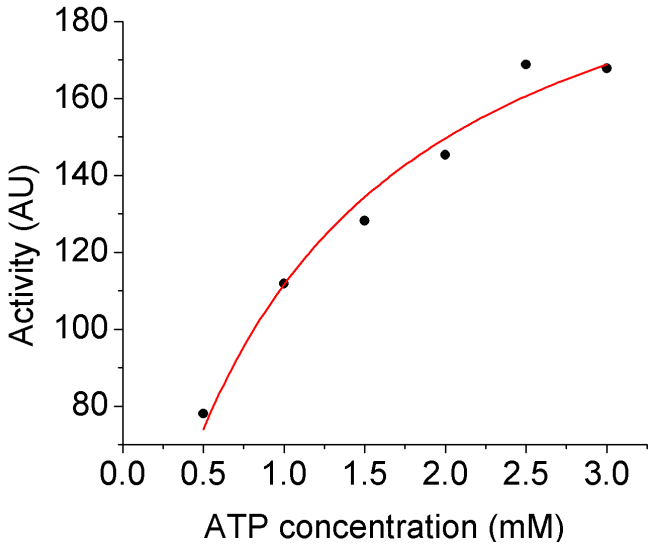

Figure 5.5: Plotting enzymatic activity versus ATP concentration. Enzymatic activity for each ATP concentration is the slope of the corresponding line in Fig. 5.4. Fitting this curve with Eq. 5.12 gives $k_{ATP} = 1.2$ mM.

enzymatic activity was measured with NADH assay for each of the solutions. The enzymatic speed for each solution is the slope of the corresponding line in Fig. 5.4. Fig. 5.5 shows the activity of the enzyme versus ATP concentration, i.e the slope of each line in Fig.5.4 versus the ATP concentration corresponding to that line. Fitting this curve with Eq. 5.12 gives $k_{ATP} = 1.2$ mM.

Bibliography

[AAZ15] Zahra Alavi, Amila Ariyaratne, and Giovanni Zocchi. "Nano-rheology measurements reveal that the hydration layer of enzymes partially controls conformational dynamics." *Appl. Phys. Lett.*, **106**:203702, 2015.

[al05] H. Frauenfelder et al. "A unified model of protein dynamics." *PNAS*, **106**:5129–34, 2005.

[al11] B. D. Armstrong et al. "Site-specific hydration dynamics in the nonpolar core of a molten globule by dynamic nuclear polarization of water." *JACS*, **133**:5987–95, 2011.

[ALL16] Utkarsh Anand, Jingyu Lu, Duane Loh, Zainul Aabdin, and Utkur Mirsaidov. "Hydration Layer-Mediated Pairwise Interaction of Nanoparticles." *Nano Lett.*, **16**:786790, 2016.

[AW09] Shina C. L. Kamerlina Andrei V. Pisliakova, Jie Caoa and Arieh Warshel. "Enzyme millisecond conformational dynamics do not catalyze the chemical step." *PNAS*, **106**:17359–64, 2009.

[AWT14] A. Ariyaratne, C. Wu, C-Y. Tseng, and G. Zocchi. "Dissipative Dynamics of Enzymes." *Phys. Rev. Lett.*, **113**:198101, 2014.

[AZ15] A. Ariyaratne and G. Zocchi. "Plasmon resonance enhanced mechanical detection of ligand binding." *Appl. Phys. Lett.*, **106**:013702, 2015.

[BH11] Carlos Lopez Darryl A. Wesener Wayne Hubbell Silvia Cavagnero Brandon D. Armstrong, Jennifer Choi and Songi Han. "Site-Specific Hydration Dynamics in the Nonpolar Core of a Molten Globule by Dynamic Nuclear Polarization of Water." *JACS*, **133**:5987–5995, 2011.

[BOS79] Joan F. Back, David Oakenfull, and Malcolm B. Smith. "Increased thermal stability of proteins in the presence of sugars and polyols." *ACS Biochemistry*, 1979.

[Bre61] H. Brenner. "The slow motion of a sphere through a viscous uid towards a plane surface." *Chem. Eng. Sci.*, **16**:242–251, 1961.

[Con06] Brian E. Conway. *Electrical Double-Layer and Ion Adsorption Behavior at Solid-Solution Interface*. Taylor Francis, 2006.

[CRE08] C. Camilloni, A. Guerini Rocco, I. Eberini, E. Gianazza, R. A. Broglia, and G. Tiana. "Urea and Guanidinium Chloride Denature Protein L in Different Ways in Molecular Dynamics Simulations." *Biophys. J.*, 2008.

[CZ07] B. Choi and G. Zocchi. "Guanylate kinase, induced t, and the allosteric spring probe." *Biophys. J.*, **92**:1651–1658, 2007.

[Deb88] Peter J.W. Debye. *The Collected Papers of Peter J.W. Debye.* Ox Bow Press, 1988.

[DS86] D. Dreusike and G. E. Schulz. "The glycine-rich loop of adenylate kinase forms a giant anion hole." *FEBS Lett.*, **208**:301–304, 1986.

[Fen02] McMahon BH Parak FG Fenimore PW, Frauenfelder H. "Slaving: Solvent fluctuations dominate protein dynamics and functions." *PNAS*, **99**:16047–16051, 2002.

[Fen04] McMahon BH Young RD Fenimore PW, Frauenfelder H. "Bulk-solvent and hydration-shell fluctuations, similar to alpha and beta fluctuations in glasses, control protein motions and functions." *PNAS*, **101**:14408–14413, 2004.

[FMA01] Hans Frauenfelder, Benjamin H. McMahon, Robert H. Austin, Kelvin Chu, and John T. Groves. "The role of structure, energy landscape, dynamics and allostery in the enzymatic function of myoglobin." *PNAS*, 2001.

[FPP07] D. Freedman, R. Pisani, and R. Purves. *Statistics*. W. W. Norton Company, 2007.

[Fra06] Chen G McMahon BH Frauenfelder H, Fenimore PW. "Protein folding is slaved to solvent motions." *PNAS*, **103**:15469–15472, 2006.

[FRJ15] Craig Fogle, Joseph Rudnick, and David Jasnow. "Protein viscoelastic dynamics: A model system." *Phys. Rev. E*, **92**:032719, 2015.

[FSH13] J.M. Franck, J.A. Scott, and S. Han. "Nonlinear scaling of surface water diffusion with bulk water viscosity of crowded solutions." *JACS*, **135**:4175–78, 2013.

[Gra47] David C. Grahame. "The electrical double layer and the theory of electrocapillarity." *Chemical Reviews*, **41**:441–501, 1947.

[Hib06] Christova P. Renault L. Seclaman E. Thompson A. Girard E. Munier-Lehmann H. Cherfils J. Hible, G. "Unique GMP-binding site in Mycobacterium tuberculosis guanosine monophosphate kinase." *Proteins*, **62**:489–500, 2006.

[HM13] Oshima H1 and Kinoshita M. "Effects of sugars on the thermal stability of a protein." *The Journal of Chemical Physics*, 2013.

[Jac98] John David Jackson. *Classical Electrodynamics, 3rd edition.* John Wiley and Sons, Inc., 1998.

[JCS07] Povey JF, Smales CM, Hassard SJ, and Howard MJ. "Comparison of the effects of 2,2,2-trifluoroethanol on peptide and protein structure and function. Comparison of the effects of 2,2,2-trifluoroethanol on peptide and protein structure and function." *Journal of Structural Biology*, 2007.

[JH13] John A. Scott John M. Franck and Songi Han. "Nonlinear Scaling of Surface Water Diffusion with Bulk Water Viscosity of Crowded Solutions." *JACS*, **135**:4175–4178, 2013.

[JZ97] H. Jensenius and G. Zocchi. "Measuring the spring constant of a single polymer chain." *Phys. Rev. Lett.*, **79**:5030, 1997.

[KBB06] M. Kawakami, K. Byrne, D. J. Brockwell, S. E. Radford, and D. A. Smith. "Viscoelastic study of the mechanical unfolding of a protein by AFM." *Biophys. J.*, **91**:L16–L18, 2006.

[KLT07] Kather, Ming Lei, Vu Thai, S Jordan Kerns, Martin Karplus, and Dorothee Kern. "A hierarchy of timescales in protein dynamics is linked to enzyme catalysis." *Nature*, 2007.

[Kos94] D. E. Koshland. "The key-lock theory and the induced fit theory." *Angew. Chem. Int. Ed. Engl.*, **33**:2375, 1994.

[KR68] E. Kretschmann and H Reather. "Radiative decay of nonradiative surface plasmon excited by light." *Z. Naturf.*, **23a**:2135–2136, 1968.

[KS03] Friedrich Kremer and Andreas Schonhals. *Broadband Dielectric Spectroscopy.* Springer, 2003.

[LC93] A. Luzar and D. Chandler. "Structure and hydrogen bond dynamics of water-dimethyl sulfoxide mixtures by computer simulations." *J. Chem. Phys.*, **98**:8160–73, 1993.

[Mau61] A. D. Maude. "End e ects in a falling-sphere viscometer." *Br. J. Appl. Phys.*, **12**(293), 1961.

[MHT12] J. J. Mock, R. T. Hill, Yu-Ju Tsai, A. Chilkoti, and D. R. Smith. "Probind Dynamically Tunable Localized Surface Plasmon Resonances of Film-Coupled Nanoparticles by Evanescent Wave Excitation." *Nano Letters*, **12**:1757–1764, 2012.

[MK05] Paul Maragakis and Martin Karplus. "Large Amplitude Conformational Change in Proteins Explored with a Plastic Network Model: Adenylate Kinase." *J. Mol. Biol.*, **352**(4):807 – 822, 2005.

[ML16] Tsvi Tlusty Michael R. Mitchell and Stanislas Leibler. "Strain analysis of protein structures and low dimensionality of mechanical allosteric couplings." *PNAS*, **113**:E5847–E5855, 2016.

[Mos] Elisha Moses. "private communication.".

[MW06] William W. Parson Mats H. M. Olsson and Arieh Warshel. "Dynamical Contributions to Enzyme Catalysis: Critical Tests of A Popular Hypothesis." *Chemical Reviews*, **106**:1737–56, 2006.

[OB83a] R. W. O'Brien. "The solution of the electrokinetic equations for colloidal particles with thin double layers." *Journal of Colloid and Interface Science*, **92**:204–216, 1983.

[OB83b] M. E. O'Neill and K. B. Banger. "The approach of a sphere to an interface." *Phys. Fluid*, **26**:2035–2042, 1983.

[OB11] S. Sacquin-Mora O. Delalande and M. Baaden. "Enzyme Closure and Nucleotide Binding Structurally Lock Guanylate Kinase." *Biophys. J.*, **101**:1440–1449, 2011.

[Ott71] A. Otto. "Exitation of nonradiative surface plasma waves in silver by the method of frustrated total re ection." *Z. Naturf.*, **241**:313–324, 1971.

[PH08] Erik Persson and Bertil Halle. "Cell water dynamics on multiple time scales." *PNAS*, **105**:6266–6271, 2008.

[QLZ12] Hao Qu, Jonathan Landy, and Giovanni Zocchi. "Cracking phase diagram for the dynamics of an enzyme." *Phys. Rev. E*, **86**:041915, 2012.

[QSK98] Zou Q, Habermann-Rottinghaus SM, and Murphy KP. "Urea effects on protein stability: hydrogen bonding and the hydrophobic effect." *Proteins*, 1998.

[QZ13] Hao Qu and Giovanni Zocchi. "How Enzymes Work: A Look through the Perspective of Molecular Viscoelastic Properties." *Phys. Rev. X*, **3**:011009, 2013.

[RFC94] M. Radmacher, M. Fritz, J. P. Cleveland, D. A. Walters, and P. K. Hansma. "Imaging adhesion forces and elasticity of lysozyme adsorbed on mica with the atomic force microscope." *Langmuir*, **10**:3809, 1994.

[RMF09] Carrotta R, Manno M, Giordano FM, Longo A, Portale G, Martorana V, and Biagio PL. "Protein stability modulated by a conformational effector: effects of trifluoroethanol on bovine serum albumin." *Physical Chemistry*, 2009.

[Rus08] Daniela Russo. "The impact of kosmotropes and chaotropes on bulk and hydration shell water dynamics in a model peptide solution." *J. Chem. Phys.*, **345**:200–211, 2008.

[SB12] Biman Jana Susmita Roy and Biman Bagchi. "Dimethyl sulfoxide induced structural transformations and non-monotonic concentration dependence of conformational fluctuation around active site of lysozyme." *J. Chem. Phys.*, **136**:115103(1–10), 2012.

[SEH92] F. D. Sonnichsen, J. E. Van Eyk, R. S. Hodges, and B. D. Sykes. "Effect of trifluoroethanol on protein secondary structure: an NMR and CD study using a synthetic actin peptide." *ACS Biochemistry*, 1992.

[SSS02] N. Sekulic, L. Shuvalova, O. Spangenberg, M. Konrad, and A. Lavie. "Structural characterization of the closed conformation of mouse guanylate kinase." *J. Biol. Chem.*, **277**:30236–30243, 2002.

[ST07] Y. Savir and T. Tlusty. "Conformational proofreading: The impact of conformational changes on the specificity of molecular recognition." *PLoS ONE*, **2**:e468, 2007.

[TLE17] Tsvi Tlusty, Albert Libchaber, and Jean-Pierre Eckmann. "Physical Model of the Genotype-to-Phenotype Map of Proteins." *Phys. Rev. X*, **7**:021037, 2017.

[TMH02] T. A. Taton, edited by M. Egli, P. Herdewijn, A. Matsuda, and Y. S. Sangvhi. "Preparation of Gold Nanoparticle-DNA Conjugates." *ohn Wiley and sons, Inc.,Malden, MA*, pp. 12.2.1–12.2.12., 2002.

[TWZ09] Chiao-Yu Tseng, Andrew Wang, Giovanni Zocchi, Biljana Rolih, and Alex J. Levine. "Elastic energy of protein-DNA chimeras." *Phys. Rev. E*, **80:061912**, 2009.

[TWZ10] C.-Y. Tseng, A. Wang, and G. Zocchi. "Mechano-chemistry of the enyzme Guanylate Kinase." *Europhys. Lett.*, **91**:18005, 2010.

[TZ13] C-Y. Tseng and G. Zocchi. "Mechanical control of Renilla Luciferase." *J. Am. Chem. Soc.*, **135**:11879, 2013.

[VB92] Iosif I. Vaismant and Max L. Berkowitz. "Local Structural Order and Molecular Associations in Water-DMSO Mixtures. Molecular Dynamics Study." *Journal of American Chemical Society*, **114**:7889–96, 1992.

[WTH04] Magnus Wolf-Watz, Vu Thai, Katherine Henzler-Wildman, Georgia Hadjipavlou, Elan Z Eisenmesser, and Dorothee Kern. "Linkage between dynamics and catalysis in a thermophilic-mesophilic enzyme pair." *Nature*, 2004.

[WZ10] Yong Wang and Giovanni Zocchi. "Elasticity of globular proteins measured from the AC susceptibility." *Phys. Rev. Lett.*, **105**:238104, 2010.

[WZ11a] Yong Wang and Giovanni Zocchi. "The folded protein as a viscoelastic solid." *Europhys. Lett.*, **96**:18003, 2011.

[WZ11b] Yong Wang and Giovanni Zocchi. "Viscoelastic transition and yield strain of the folded protein." *PLoS ONE*, **6(12)**:e28097, 2011.

[YLK03] Haw Yang, Guobin Luo, Pallop Karnchanaphanurach, Tai-Man Louie, Ivan Rech, Sergio Cova, Luying Xun, and X. Sun. "Protein Conformational Dynamics Probed by Single-Molecule Electron Transfer." *Science*, 2003.

[YT10] Ron Milo Yonatan Savir, Elad Noor and Tsvi Tlusty. "Cross-species analysis traces adaptation of Rubisco toward optimality in a low-dimensional landscape." *PNAS*, **107**:3475–3480, 2010.

[YZ16a] Lijuan Wanga Yangzhong Qina and Dongping Zhong. "Dynamics and mechanism of ultrafast water-protein interactions." *PNAS*, **113**:8424–8429, 2016.

[YZ16b] Lijuan Wanga Yangzhong Qina and Dongping Zhong. "Mapping Hydration Dynamics around a -Barrel Protein." *JACS*, **139**:4399–4408, 2016.

[ZMZ13] Xinming Zhang, Lu Ma, and Yongli Zhang. "High-Resolution Optical Tweezers for Single-Molecule Manipulation." *Yale Journal of Biology and Medicine*, 2013.

[Zoc09] G. Zocchi. "Controlling proteins through molecular springs." *Ann. Rev. Biophys.*, **38**:75–88, 2009.